Colloids and Surfaces A: Physicochem. Eng. Aspects 436 (2013) 1092–1102

Contents lists available at ScienceDirect

Colloids and Surfaces A: Physicochemical and Engineering Aspects

journal homepage: www.elsevier.com/locate/colsurfa

Physicochemical aspects behind the size of biodegradable polymeric nanoparticles: A step forward

Anderson M. de Oliveira[a], Eliézer Jäger[b], Alessandro Jäger[b], Petr Stepánek[b], Fernando C. Giacomelli[a,*]

[a] Centro de Ciências Naturais e Humanas, Universidade Federal do ABC, 09210-170 Santo André, Brazil
[b] Institute of Macromolecular Chemistry, Heyrovsky Sq. 2, 162 06 Prague 6, Czech Republic

HIGHLIGHTS

- PLGA sub-100 nm polymeric nanoparticles were produced.
- The size of the nanoparticles can be linearly tuned by using mixtures of solvents.
- A size-dependent effect on the organic solvent has been observed.
- Polymer–solvent interaction does not play a substantial role in the final dimension.

GRAPHICAL ABSTRACT

The size of biodegradable polymeric nanoparticles prepared by nanoprecipitation can be tuned by using appropriate organic solvents or mixtures of organic solvents.

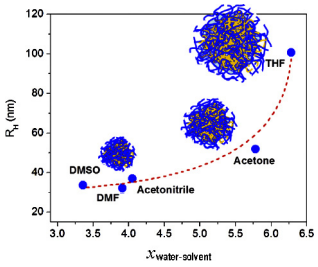

ARTICLE INFO

Article history:
Received 10 July 2013
Received in revised form 18 August 2013
Accepted 27 August 2013
Available online xxx

Keywords:
Sub-100 nm polymeric nanoparticles
Light scattering
Nanoprecipitation

ABSTRACT

Surfactant-free PLGA polymeric nanoparticles (PNPs) with hydrodynamic radius (R_H) ranging from 25.8 nm to 128.5 nm were successfully obtained through nanoprecipitation by controlling a variety of physicochemical parameters. The size of the generated PLGA PNPs could be controlled by adjusting the polymer concentration, the choice of organic solvent, mixing different organic solvents or by changing temperature and ionic strength. By optimizing such parameters sub-100 nm uniform PNPs can be produced through this methodology including the advantage and ability to scale-up production. The PNPs have shown a size-dependent effect on the organic solvent and polymer concentration. On the other hand, the polymer–solvent interactions seem not to play a substantial role in the final dimension of the polymer colloids. It has been also evidenced that the size of PNPs can be precisely and linearly tuned by using solvent mixtures as organic phase.

1. Introduction

Polymeric nanoparticles (PNPs) have proven to be a very useful component in advanced materials science with a myriad of applications in biotechnology, environmental technology, pollution control and especially biomedical applications including usage in diagnostic [1], vaccine [2], gene delivery [3] as well as anticancer therapies [4,5]. The potential use of PNPs is therefore diverse and it relies certainly on their physicochemical properties which can be frequently tuned towards the desirable application. The development of nanoscale materials is generally motivated by their unique properties conferred by the high surface to volume ratio. The benefits of PNPs include protection of encapsulated substances against degradation, reduced side-effects, higher therapeutic efficacy, sustained drug release, specific accumulation, high cellular internalization and long blood circulation half-life [6–8].

There are indeed a large number of polymers and block copolymers available for the preparation of PNPs. The commonly used in drug delivery belong to the family of biodegradable polyesters

* Corresponding author. Tel.: +55 11 4996 8361; fax: +55 11 4996 0090.
E-mail addresses: fernando.giacomelli@ufabc.edu.br, fernandogiacomelli@gmail.com (F.C. Giacomelli).

0927-7757/$ – see front matter © 2013 Elsevier B.V. All rights reserved.
http://dx.doi.org/10.1016/j.colsurfa.2013.08.056

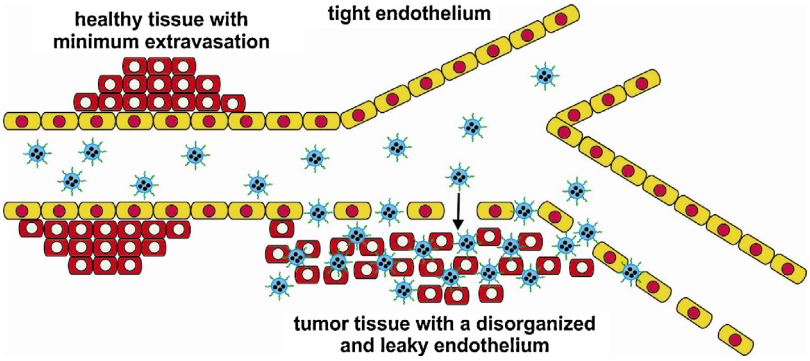

Fig. 1. Schematic representation of the passive tumor accumulation of polymeric nanoparticles due to the EPR effect (the leaky tumor vasculature allows the preferential PNPs extravasation).

including poly(lactic-*co*-glycolic acid) (PLGA) [9–12]. The PLGA is reported to exhibit excellent biocompatibility [13] and adequate biodegradation under physiological conditions [14,15]. Moreover, PLGA-based nanoparticles have been widely used for drug encapsulation and delivery investigations [10,16,17], although they might show relatively low drug loading capacity and often an initial burst release depending on drug nature [18,19].

Particularly in the field of nanomedicine, the ability to control the dimension of PNPs is essential. The biodegradable polymeric nanocontainers are frequently investigated as potential tumor targeting vehicles since they are able to be accumulated into solid tumors due to combination of the generally leaky microvasculature and missing or tight lymphatic capillary system. This is known as the enhanced permeability and retention (EPR) effect as it is schematically depicted in Fig. 1 [20].

Since the leaky vasculature is distinct from tumor to tumor, the size of the nanocarriers influences the vascular permeability. Generally, nanoparticles smaller than 100 nm are preferentially accumulated at tumor sites by the EPR effect [21,22], although only smaller particles (~30 nm) might be able to penetrate poorly permeable tumors [23]. Furthermore, it has been evidenced that PEGylated PNPs under 70 nm have the potential of bypassing the reticuloendothelial system (RES), which leads to persistent circulation half-life [24]. On the other hand, the PNPs have also to be sufficiently large (D_H > 10 nm) otherwise they might experience fast renal clearance [25,26]. Additionally, the rate of PNPs uptake by tumor cells once they reach the specific tumor site is also influenced by the particle size. It has been demonstrated that rapid cellular uptake of PNPs can be achieved when the size falls below 50 nm [27]. The mean particle size also impacts in the biodistribution of nanoparticles [12,28]. Indeed, the effect of mean particle size on biodistribution has been shown to be non-linear varying from organ to organ [29]. Lastly, the polydisperity of the particle population is also a significant factor in performance. Preparation of particles that are highly uniform will exhibit more consistent biodistribution, cellular uptake and drug release [12]. Therefore, all the aforementioned informations highlight the importance of to be able to tune the size and size-distribution of PNPs for each distinct biomedical application.

There are several established methods to prepare polymeric nanoparticles including the emulsification–solvent diffusion, salting out and nanoprecipitation (solvent shifting) [30]. Recently, more elaborated nanoprecipitation protocols have been suggested [31,32]. The nanoprecipitation refers to a quite simple process relying on the fast diffusion of an organic polymer solution into an aqueous phase resulting in the reduction of the interfacial tension between the two phases and the formation of small droplets of organic solvent [33]. This finally leads to the precipitation of the polymer into small colloidal particles. Actually, the accurate mechanism of PNPs formation through nanoprecipitation still remains an open debate. The fast formation of PNPs is probably governed by the Gibbs–Marangoni effect at high polymer concentration and high organic:aqueous phase ratio whereas nanoparticle formation comprises a nucleation-and-growth process at low organic:aqueous phase ratio and low polymer concentration [34]. The nucleation-and-growth process comprises three stages [35]: nucleation, growth and aggregation. The rate of each step determines the particle size and the driving force of these phenomena are influenced by polymer concentration and its solubility in the solvent mixture. The separation between the nucleation, growth and aggregation is the key factor for uniform particle formation.

Although the nanoprecipitation method has outstanding advantages compared to the others such as the fast processing time and the low energy consumption, it has also serious shortcomings, for instance the production of generally large PNPs (D_H > 100 nm), low mass fraction of nanoparticles in the prepared samples and generally broad size-distribution [36]. Currently, the physical causes of this limitation are not understood. Indeed, the fundamental knowledge about the process of preparation of PNPs is still limited. The effect of the homogenization conditions and the control of droplet size distribution which determines the particle size and morphology are not fully understood [30]. Therefore, future research is needed focusing on the development of simple protocols that provide precise and reproducible control over the particle size and morphology, which are the key determinants of the properties and applications of these wondrous particles. Indeed, a deeper understanding of the physicochemical phenomena involved during PNPs formation is still necessary. Specifically, the relationship between physicochemical parameters and their quantitative effects on PNPs features could be an invaluable tool in the controlled engineering of particles. A simple and reproducible process for the preparation of PNPs would enable manufacturing of PNPs with distinct properties and allow an easy achievement of optimal properties for a given application. These efforts might speed up the commercial utilization of PNPs.

The motivation of the current investigation was therefore to evaluate in details the influence of the physicochemical properties of the aqueous and organic phase during the preparation of biodegradable PNPs as well as their effect on the final characteristics of the PNPs produced by the nanoprecipitation approach. The physicochemical aspects behind the size and size-distribution of PNPs have been focused. The well-known PLGA (poly(lactic-*co*-glycolic acid)) copolymer was selected as the central polymer due to its biocompatibility, biodegradability and proven record in polymer-based nanotechnologies. There is a forthcoming paper underway where the mechanical aspects on the final properties

of PLGA PNPs (mixing rate, stirring rate of non-solvent) is also being discussed. Although we were aware that naked PLGA PNPs are susceptible to protein adsorption and phagocytosis when administered intravenously, therefore they are not stable in the bloodstream since they are easily recognized by the body immune system [37], it has been decided to manipulate the pure copolyester in order to explore the influence of physicochemical parameters in the final features of the PNPs with minimum interfering. It is demonstrated that the size of PLGA PNPs can be easily and precisely tuned from 25.8 nm to 128.5 nm by altering the physicochemical parameters during the nanoprecipitation protocol. The driven force of the process is asserted to be the solvent–water interaction whereas polymer–solvent interactions seem to be of less importance in the final dimension of the colloids.

2. Experimental

2.1. Materials and reagents

The poly(lactic-*co*-glycolic acid) PLGA01 (lactide:glycolide 50:50, $M_w = 60{,}000\ g\ mol^{-1}$, $M_w/M_n = 2.0$), PLGA02 (lactide:glycolide 65:35, $M_w = 75{,}000\ g\ mol^{-1}$, $M_w/M_n = 1.9$), PLGA03 (lactide:glycolide 85:15, $M_w = 75{,}000\ g\ mol^{-1}$, $M_w/M_n = 1.5$) and the poly(ε-caprolactone) PCL ($M_w = 65{,}000\ g\ mol^{-1}$, $M_w/M_n = 1.5$) were purchased from Sigma Aldrich and used as received. The poly(butylene succinate-*co*-butylene dilinoleate) herein referred to as PBS:PBDL was synthesized following a procedure previously described [38]. All the solvents employed in the preparation of the PNPs were of analytical grade and they were used as received. The water was pretreated with the Milli-*Q*® Plus System (Millipore Corporation).

2.2. Preparation of the nanoparticles

The PNPs were prepared by the nanoprecipitation approach from stock polymer solutions of different concentrations prepared in different solvents (acetone, acetonitrile, *N*,*N*-dimethylformamide (DMF), tetrahydrofuran (THF) and dimethyl sulfoxide (DMSO)). Typically, the nanoparticles were produced by pouring 2.0 mL of the organic polymer solutions (solvent) into 5.0 mL of pure Milli-*Q*® water or brine solution (antisolvent) by using a syringe at flow rate of $2\ mL\ min^{-1}$. The stirring speed of the aqueous phase was kept fixed in all the experiments (350 rpm) whereas solvent, polymer nature, polymer concentration, solvent:water ratio, temperature and ionic strength were variables of study. The high boiling point organic solvents were removed by membrane dialysis (MWCO 10 kDa) whereas acetone was removed by evaporation at environmental temperature. To ensure the reproducibility of the preparation procedure, the nanoparticles were formulated three times under the same conditions. The final aqueous volume after the nanoprecipitation procedure and organic solvent elimination was set to 5.0 mL and the given polymer concentrations throughout the manuscript correspond to the concentrations after the aforementioned procedure.

2.3. Scattering characterization of the nanoparticles

Dynamic (DLS) and electrophoretic (ELS) light scattering measurements were performed by using the Zetasizer NanoZS apparatus (Malvern Instruments, UK). The intensity correlation functions were measured at 173°. The correlation functions were further analyzed using the cumulant approach as [39,40]:

$$\ln g_1(t) = \ln A - \Gamma t + \frac{\mu_2}{2}t^2 \cdots \quad (1)$$

wherein A is the amplitude of the correlation functions, Γ is the decay rate and in a sufficiently diluted system it is related to the diffusion coefficient of the nanoparticles. The parameter μ_2 is the second-order cumulant. The hydrodynamic radius (R_H) of the scattering objects was calculated from the resulting relaxation time τ ($1/\Gamma$) by using the Stokes–Einstein relation:

$$R_H = \frac{k_B T q^2}{6\pi\eta}\tau \quad (2)$$

where k_B is the Boltzmann constant, T is the absolute temperature, η is the viscosity of the solvent and q is the scattering vector:

$$q = \frac{4\pi n}{\lambda}\sin\left(\frac{\theta}{2}\right) \quad (3)$$

n being the refractive index of the solvent and θ the scattering angle. The second-order cumulant (μ_2) was used to compute the polydispersity index ($PDI = \mu_2/\Gamma^2$) which is a measure of the width of the monomodal decay rate distribution.

To ensure the monomodal distribution of nanoparticles, the correlation functions were also analyzed using the algorithm REPES (incorporated in the GENDIST program) which employs the inverse Laplace transformation according to Eq. (4).

$$g_2(t) - 1 = \beta\left[\int A(\tau)\exp(-t/\tau)d\tau\right]^2 \quad (4)$$

where t is the delay time of the correlation function and β is an instrumental parameter [41]. The resulting function is a distribution of relaxation times consisting generally of several peaks representing individual dynamic processes. Herein, the distributions of relaxation times were converted into distributions of R_H by using the Stokes–Einstein equation.

The average zeta potential (ζ) of the nanoparticles was determined by measuring their electrophoretic mobility (U_E) and the values were converted to ζ-potential (mV) through the Henry's equation:

$$\zeta = \frac{3\eta U_E}{2\varepsilon f(ka)} \quad (5)$$

wherein ε is the dielectric constant of the medium. The parameter $f(ka)$ is the Henry's function which has been calculated through the Smoluchowski approximation $f(ka) = 1.5$.

The small angle X-ray scattering (SAXS) measurements were performed at the SAXS1 beamline of the Brazilian Synchrotron Light Laboratory (LNLS—Campinas, SP, Brazil) operating at wavelength $\lambda = 1.55$ Å and consisting of a temperature-controlled vacuum flow-through cell and a Pilatus 300 K 2D detector (Dectris). The 2D-images were found to be isotropic and they were normalized by the sample transmission undertaken using the FIT2D software. The $I(q)$ *vs.* q scattering curves were corrected by the subtraction of the scattering of the pure solvent.

The Transmission electron microscopy (TEM) measurements were performed on a JEM 200CX microscope (Jeol, Japan). The microphotographs were taken at acceleration voltage 100 kV (JEM 200CX) and recorded on a digital camera. The nanoparticles were diluted 100 times and a 5-μL droplet was deposited onto a copper TEM grid (300 mesh) coated with carbon film.

3. Results and discussion

The effect of a variety of physicochemical parameters such as the polymer concentration, organic solvent nature as well as solvent:water ratio on the final size, size-distribution and zeta potential of biodegradable PNPs have been investigated. The DLS data provide informations about the hydrodynamic radius and size

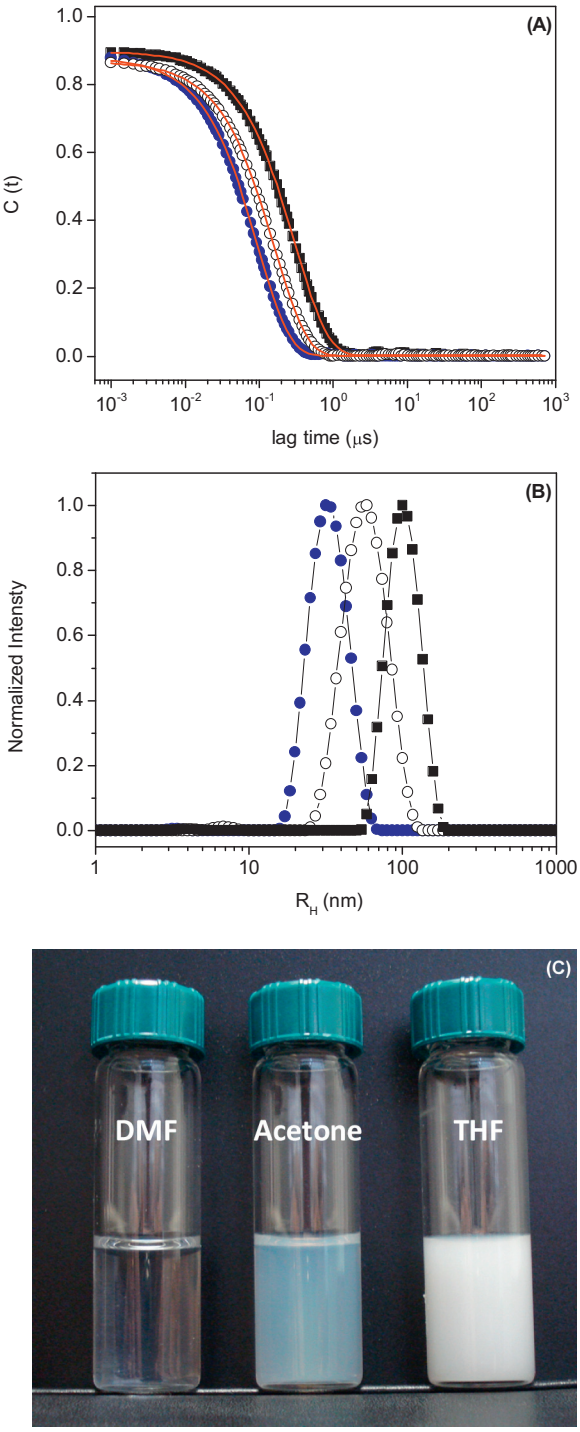

Fig. 2. Autocorrelation functions measured at 173 °C and 25.0 °C (A), respective distributions of R_H revealed by the REPES algorithm (B) and the visual appearance of PLGA01 PNPs produced from different organic solvents (C): DMF (●), acetone (○) and THF (■). The polymer concentration and the solvent:water ratio were preset to 1.4 mg mL^{-1} and 0.4 mg mL^{-1}. The solid lines in (A) correspond to the cumulant fittings. (For interpretation of the references to color in this figure legend, the reader is referred to the web version of this article.)

dispersity. Fig. 2 portrays representative examples of the autocorrelation functions along to the cumulant fits (A), the respective distributions of R_H (B) and the visual appearance of PLGA01 PNPs produced at preset polymer concentration (1.4 mg mL^{-1}) and solvent:water ratio (0.4) in DMF, acetone and THF according to the legend.

The nanoprecipitation process yields single particle populations in all the cases. The cumulant expansion fitted the curves reasonably well suggesting a monomodal distribution of nanoparticles ($\mu_2/\Gamma^2 < 0.15$). This is also supported by the distributions of R_H given in Fig. 2B. The visual appearance of the suspensions is size-dependent regardless the physicochemical parameter investigated. The suspensions are fully transparent for smaller particles (~40 nm) and a weakly opalescent suspension is obtained for slightly bigger PNPs (~50–60 nm). The opalescence becomes more pronounced as the size becomes even bigger. This trend can be qualitatively seen in Fig. 2C for PNPs produced by using DMF (R_H ~25 nm), acetone (R_H ~51 nm) and THF (R_H ~100 nm) as starting organic solvents. Essentially, a similar trend was observed as a function of polymer concentration. The ζ-potential of the whole set of prepared PNPs was determined to be always negative and ranging from −30 mV to −50 mV depending on the experimental conditions. The negative ζ-potential is attributed to the delocalization of the negative charges of the ester bonds and to the negative charges of the partially ionized carboxylic groups of the polymer backbone [42].

The formation of the PLGA PNPs has been also investigated by transmission electron microscopy (TEM) and small-angle X-ray scattering (SAXS). The TEM images of the suspensions portrayed in Fig. 2C are given in Fig. 3A–C where the spherical shape and size trend of the PNPs can be confirmed. The SAXS data in Fig. 3D (PLGA01 PNPs prepared in DMF) has been modeled geometrically as homogenous spheres and the fitting approach described the experimental result reasonably well leading to $R = 31.0$ nm and the polydisperisty considering the log-normal distribution $\sigma = 0.15$, therefore also supporting their spherical shape. SAXS data for larger PNPs could be not appropriately obtained due to the minimum-q accessible in the SAXS1 beamline of the LNLS.

The following sections are devoted to the whole set of experimental data along to the discussion of the influence of a number of physicochemical parameters in the final characteristics of the PNPs.

3.1. The influence of the solvent:water ratio

Taking into account that acetone is one of the widely used solvents employed in the manufacturing of PNPs by nanoprecipitation, mainly due to safety considerations and easy evaporation, the influence of the solvent:water ratio on the final characteristics of the PNPs has been primarily performed by using such a solvent. The solvent:water ratio was varied from 0.2 to 1.0 at preset final polymer concentration (1.4 mg mL^{-1}) and the experimental results for PLGA01 are given in Fig. 4.

The solvent:water ratio had a small effect on the size of the produced particles in the range from 0.4 to 1.0, although for 0.2 the manufactured PNPs are substantially bigger. In the low solvent:water ratio region (0.2 to 0.8), the mean particle size decreases as the solvent:water ratio increases. The mean particle size was reduced from 67.8 nm to 44.0 nm as the solvent:water ratio increased from 0.2 to 0.8. This can be understood by considering that a higher amount of organic solvent is injected in the aqueous phase (therefore the final volume increases). Accordingly, it is reasonable to assume the size reduction as a consequence of the formation of a higher number of nucleation sites which must lead to the formation of smaller particles once the final polymer concentration is kept fixed [43]. The maximum number of nucleation sites is supposed to be close to the solvent:water ratio ~0.6–0.8. As the solvent:water ratio increases beyond 0.6–0.8, the nucleation process might become more difficult leading to the formation of less nucleation sites and consequently bigger particles. Nevertheless, modifications in the mechanism of formation of the PNPs cannot be ruled out. Since the Gibbs–Marangoni effect is enhanced at high organic:aqueous ratio [34], the unexpected upward profile at the

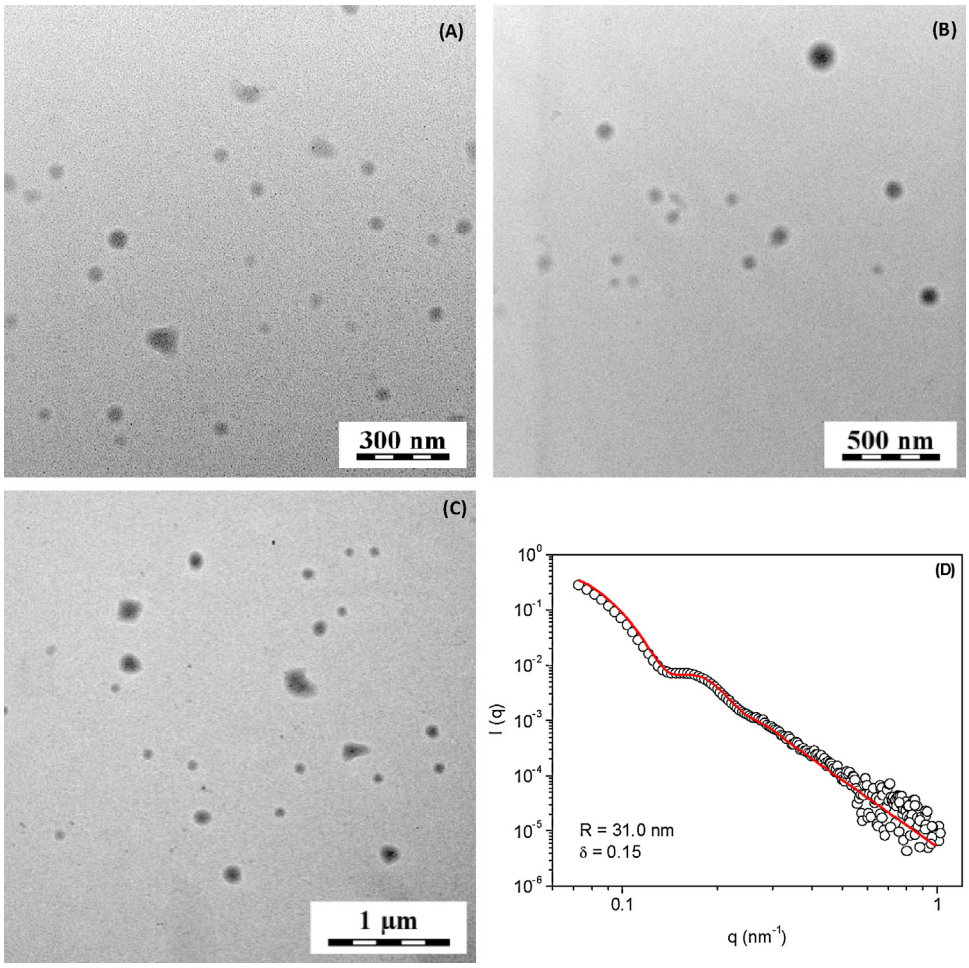

Fig. 3. TEM image of PLGA01 PNPs produced from DMF (A), acetone (B) and THF (C). SAXS data and corresponding curve fitting (solid line) for PLGA01 PNPs prepared from DMF (D).

right-hand side of Fig. 4A might also be related to mechanistic aspects although such discussion is so far beyond the scope of the current investigation.

The polydispersity, on the other hand, seems not to be affected by the solvent:water ratio since the produced PNPs are narrowly sized distributed as judged by the polydispersity index values always below 0.15 (Fig. 4B). Furthermore, the ζ-potential is an additional parameter of key importance since it helps to control the stability of nanoparticles besides being a significant factor affecting cellular uptake [44,45]. The ζ-potential of the prepared PLGA01 PNPs does not depend on the solvent:water ratio. The determined values ranged randomly in a narrow window from −30.0 mV to −40.0 mV. The high surface charge of the PNPs ($\zeta < -30.0$ mV) suggests good dispersion stability of the produced PNPs and prevent their aggregation due to the existence of electric repulsion forces. Consequently, the PNPs prepared under these conditions showed good stability for months when stored at 4 °C.

Accordingly, due to the time consuming procedure for acetone evaporation and taking into account that for larger amounts of acetone it has been evidenced only a gentle reduction in the dimension of the nano-objects (~6 nm), the further investigations have been performed by presetting the solvent:water ratio to 0.4.

3.2. The influence of the polymer concentration

The influence of polymer concentration in the size, size-distribution and ζ-potential of the prepared PNPs at preset acetone:water ratio (0.4) is portrayed in Fig. 5. The polymer concentration was systematically varied from 1.4 mg mL^{-1} to 15.0 mg mL^{-1}. The increase in polymer concentration resulted in a substantial increase in the mean particle size. The size (R_H) of the PNPs was determined to be linearly dependent on PLGA01 concentration ranging from 51.8 nm to 128.5 nm. It has been previously claimed that the volume of PNPs is proportional to the initial polymer concentration for PLGA-*b*-PEG [46]. However, we were not able to see any correlation between concentration and mean volume of the PNPs at our investigations.

Taking into account that the PNPs are produced in a large amount of nonsolvent, the increase in the mean particle size as a function of the polymer concentration might be explained by the nucleation-and-growth process. The organic polymer solution is introduced into the water phase during the nanoprecipitation and it is split into smaller domains. The diffusion and precipitation occurs almost simultaneously and as soon as the polymer nuclei of pure solute are formed they grow by capturing solute molecules from the surroundings until the electrostatic repulsions stabilization quenches the PNPs growth. Therefore, the final dimension of the resultant nanoparticles is determined by amount of polymer molecules in the vicinity available for aggregation. The increase in the number of available copolymer chains (higher concentration) leads to an increase in the number of nuclei and consequently in the probability of nuclei encounters. Each encounter causes aggregation of nuclei thereby increasing the nanoparticle size [36]. Additionally, the influence of polymer concentration on the viscosity of the organic polymer solution has to be taken into consideration. By increasing polymer concentration, the organic

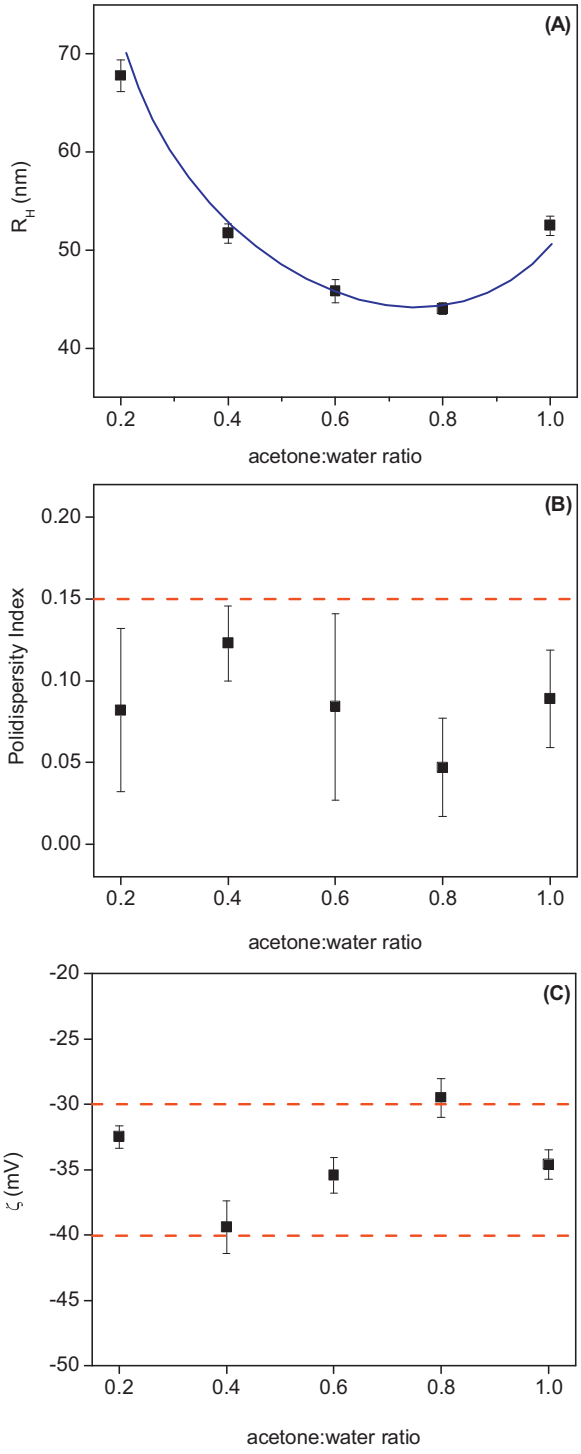

Fig. 4. Influence of acetone:water ratio on the structural features of PLGA01 nanoparticles prepared by nanoprecipitation: mean nanoparticle size (A), polydispersity index (B) and ζ-potential (C). The polymer concentration was preset to 1.4 mg mL^{-1}.

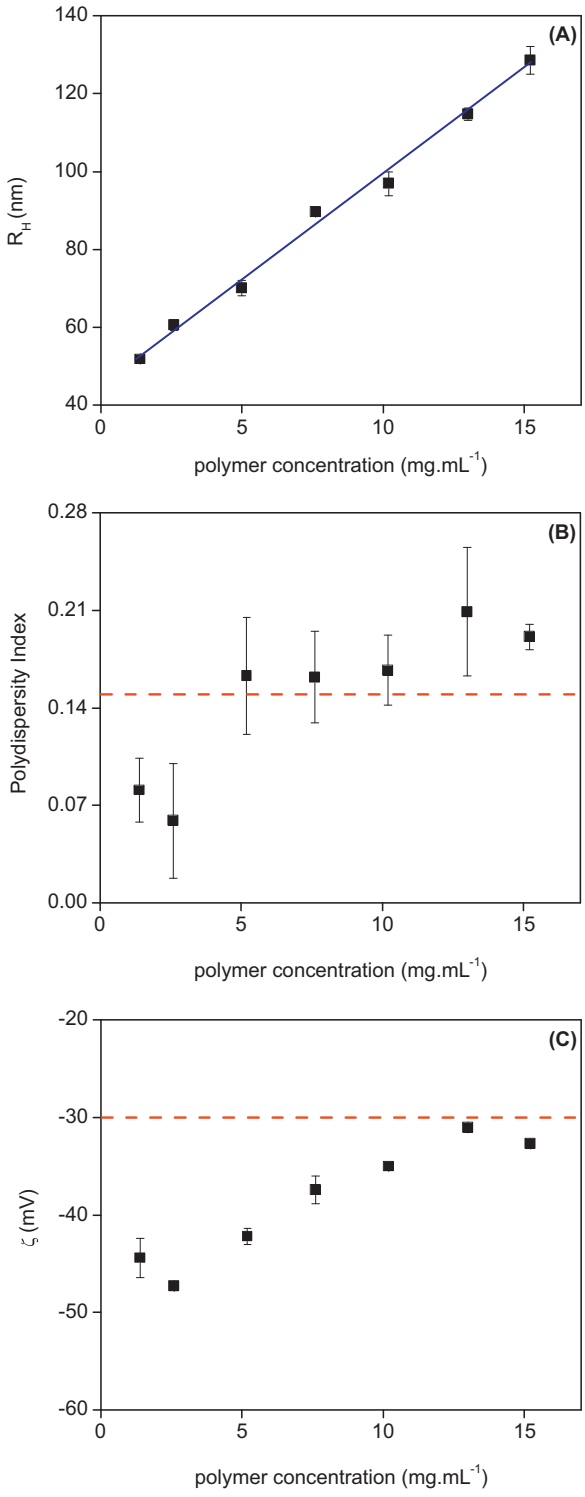

Fig. 5. Influence of the polymer concentration on the structural features of PLGA01 nanoparticles prepared by nanoprecipitation: mean nanoparticle size (A), polydispersity index (B) and ζ-potential (C). The acetone:water ratio was preset to 0.4.

solution becomes obviously more viscous due to the enhancement on polymer–polymer and polymer–solvent interactions. This leads to a higher mass transfer resistance. The diffusion of the polymer–solvent phase into the external aqueous phase is reduced and larger PNPs are formed.

Additionally, the size-distribution became broad at the condition where bigger particles were obtained (Fig. 4B) and it can be understood by considering the process of aggregation. The unsatisfactory electrostatic stabilization empowers PNPs to aggregate. The random aggregation process creates a polydisperse distribution of sizes and it predicts that the polydispersity of the distribution increases with the number of aggregation steps [47]. That is to say that the polydispersity increases as the size increases. Furthermore, the Oswald ripening cannot be ruled out in such case. The increase in concentration might cause such phenomena

enhancing the size difference between the growing nuclei due to a higher mechanical turbulence which leads to a higher polydispersity index.

Finally, a slightly dependence of the zeta potential on polymer concentration has been observed. As the size increased from 51.8 nm to 128.5 nm, the ζ-potential is slightly displaced towards smaller absolute values. Nevertheless, even for the highest concentration, the ζ-potential is still more negative than –30 mV which is used as the limit for nanoparticle stability.

3.3. Influence of the temperature

The preparation temperature was scanned from 05 °C to 55 °C and the results are portrayed in Fig. 6.

There can be noticed a substantial reduction in the mean particle size as the temperature increases. The temperature was scanned from 05 °C to 55 °C. In the investigated range, the mean particle size was reduced from 58.6 nm to 42.3 nm. As aforementioned, the nanoprecipitation relies on the fast diffusion of an organic polymer solution into an aqueous phase. The fast mixing leads to a high nucleation rate resulting in the formation of smaller nanoparticles. The increase in the temperature is supposed to enhanced the solvent–water mixing speed. This could be either due to a reduction in the viscosity or to an enhancement in the acetone–water thermodynamic affinity. The effect of the organic solvent on the mean particle size evidenced that the aqueous to non-aqueous mixing speed is not governed by the viscosity of the organic solvent (discussed hereafter). On the other hand, although the thermodynamic data is limited, the solubility parameter of water is more pronounced reduced as the temperature increases compared to acetone [48,49]. Consequently, the acetone–water affinity is enhanced at higher temperatures (the solubility parameters are closer). Additionally, by increasing the temperature, it might be supplied the required energy to overcome unfavorable solute–solvent interactions, meaning also higher solubility. Hence, the experimental results reported herein point out that that a better acetone–water affinity induces a faster organic-aqueous phase mixing, a higher nucleation rate leading to the formation of smaller PNPs at higher temperatures. As discussed hereafter, the smaller the solvent–water interaction parameter ($\chi_{solvent-water}$) the smaller the PNPs. That is to say the smallest PNPs are obtained in the most favorable solvent–water affinity. Additionally, tendencies in the polydispersity index of the samples were not observed. The value was always at ~0.07–0.10. The same is valid for the ζ-potential values which varied randomly in the negative region being always below –30 mV.

3.4. Influence of the antisolvent ionic strength

The ionic strength of the nonsolvent medium was scanned from 10^{-5} mol L^{-1} to 10^{-1} mol L^{-1} during the preparation of the PNPs. The ionic strength has been controlled by varying the NaCl concentration and the results are given in Fig. 7. There is a clear and substantial influence of the ionic strength on the mean particle size.

The mean particle size could be evaluated as a function of the ionic strength up to 0.01 mol L^{-1}. At higher ionic strength the nanoparticle dispersion flocculated upon formation and stable particles could no longer be produced. As one may notice in the range of ionic strength investigated, there is a substantial increase in the mean particle size as the ionic strength increases. The increase in NaCl concentration reduces the repulsive negative potential between PLGA polymer chains due to the screening promoted by the Na^+ ions. Therefore, the attractive van der Waals forces between the chains become dominant and the particles can collide easier leading to aggregation and the formation of bigger PNPs [50].

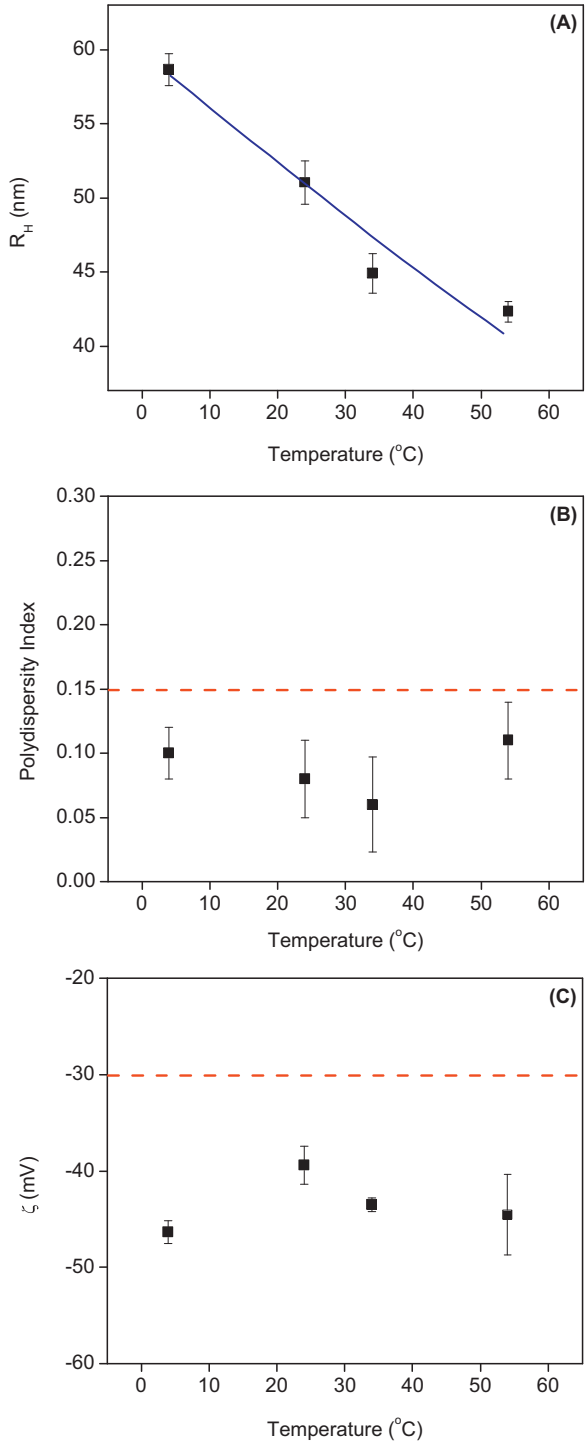

Fig. 6. Influence of the temperature on the structural features of PLGA01 nanoparticles prepared by nanoprecipitation: mean nanoparticle size (A), polydispersity index (B) and ζ-potential (C). The polymer concentration and acetone:water ratio were preset to 1.4 mg mL^{-1} and 0.4 mg mL^{-1}, respectively.

Simultaneously, a gentle reduction in the polydispersity index of the produced PNPs could be noticed.

On the other hand, a substantial reduction in the zeta potential of the PNPs was observed. This behavior can be understood by considering the PLGA surface neutralization promoted by Na^+ ions. The surface charge decreases at even higher ionic strength due to the conventional electrostatic screening.

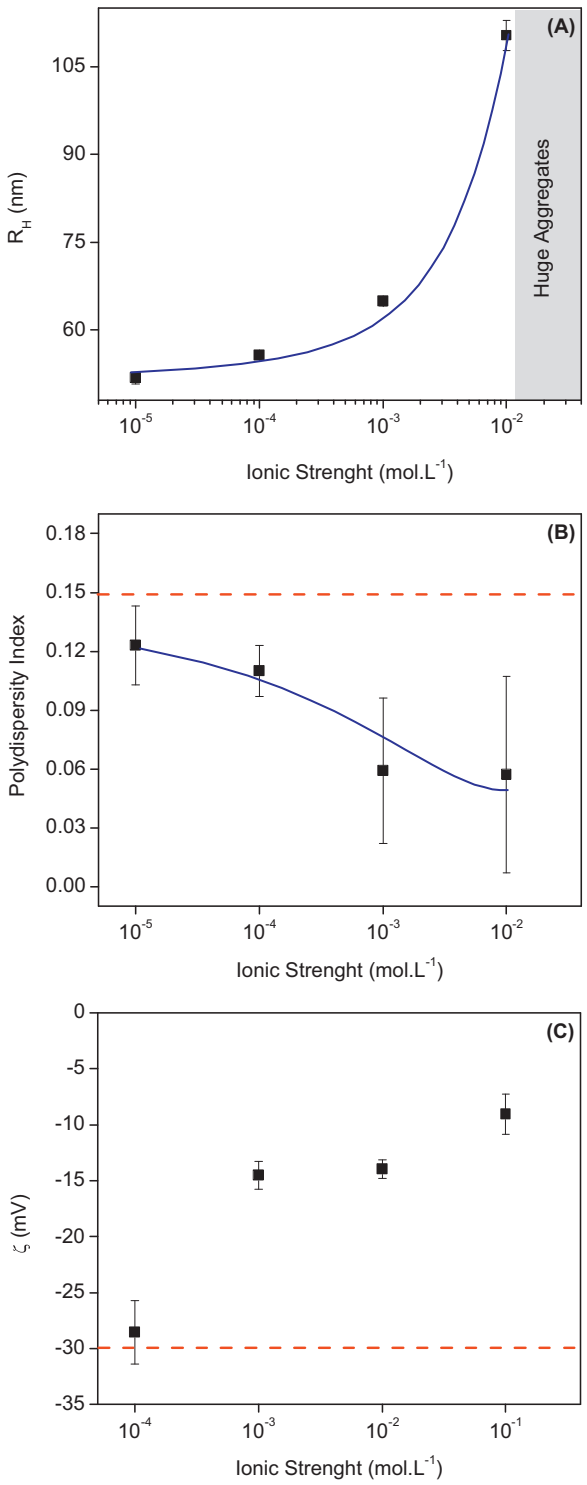

Fig. 7. Influence of the antisolvent ionic strength on the structural features of PLGA01 nanoparticles prepared by nanoprecipitation: mean nanoparticle size (A), polydispersity index (B) and ζ-potential (C). The polymer concentration and the acetone:water ratio were preset to 1.4 mg mL^{-1} and 0.4 mg mL^{-1}, respectively.

3.5. Influence of the polymer properties

The nanoprecipitation has been performed also by using different biodegradable polymers and by fixing all other investigated parameters. The results are reported in Table 1.

Qualitatively, the molecular weight as well as the molecular structure of the biodegradable polymer seem to influence the mean nanoparticle size. PLGA01 and PBS:PBDL are the polymers which led to the smallest PNPs. In the PLGA series, the size increased in the order PLGA01 < PLGA02 < PLGA03. The particle growth rate is related to the polymer molecular weight and super-saturation (linked to the solubility of the polymer in the solvent mixture) [34]. Indeed, the hydrophobicity seems to play a substantial role in the final size since PCL, which has similar molecular weight compared to PBS:PBDL and PLGA01 however it is more hydrophobic [51,52], led to much bigger PNPs ($R_H \sim 90$ nm). The hydrophobicity of PLGA can be estimated by the lactide:glycolide ratio. The higher the lactide:glycolide ratio the strong the hydrophobic character [52] of the polymer chains and its tendency to aggregate upon water contact. The mean particle size is larger when they were prepared by using more hydrophobic polymers since the nuclei require more polymer chains to be stabilized. Additionally, due to higher nuclei hydrophobicity, the aggregation step is supposed to be favored earlier during the nucleation-and-growth process. The rapid solvent diffusion towards the aqueous phase could be hindered by the increase in mass transfer due to the enhancement in polymer–polymer and/or polymer–solvent interactions. This can be evidenced by comparing PNPs prepared by using PLGA02 and PLGA03.

Additionally, the mean particle size increases with molecular weight. This trend is explained by the increased size of the collapsed polymer chains and the lower charge density contributed by each chain, resulting in larger particles when they aggregate.

Table 1
Macromolecular characteristics of the biodegradable polymers and physicochemical properties of the produced nano-objects as determined by DLS and ELS.

Entry	M_w (g mol^{-1})	Lactide:glycolide	M_w/M_n	R_H(nm)	*PDI*	ζ (mV)
PLGA0I	60,000	50:50	2.0	51.8	0.12	−39.4
PLGA02	75,000	65:35	1.9	72.1	0.15	−34.0
PLGA03	75,000	85:15	1.5	85.0	0.15	−36.0
PCL	65,000	–	1.6	88.6	0.10	−23.0
PBS:PBDL	66,000		1.9	49.2	0.06	−35.0

Table 2
Physicochemical properties of solvents (at 25 °C) and polymers employed in the nanoprecipitation protocols: η (viscosity), ε (dielectric constant) δ (solubility parameter) and γ (surface tension).

Entiy	η (mPa s^{-1})	ε	γ (in N m^{-1})	δ (MPa$^{1/2}$)
Water	0.891	80.20	72.0	47.9
DMSO	1.987	47.24	42.9	26.4
DMF	0.794	38.25	36.4	24.7
Acetonitrile	0.369	36.64	28.7	24.3
Acetone	0.306	21.01	23.5	19.7
THF	0.456	7.52	27.1	18.5
PCL	–	–		20.4
PLGA	–	–		22.3

3.6. Influence of the organic solvent

The nanoprecipitation procedures were performed by using the following water miscible solvents: DMSO, DMF, acetone, acetonitrile and THF. In Table 2, the most important physicochemical parameters of these solvents and polymers are listed. The informations are important to discuss the reported experimental data.

The formation of PNPs through nanoprecipitation is a complex process and so far there are not enough experimental evidences to support a specific mechanism of formation. The experimental results reported herein evidenced that there is not a correlation between the viscosity of the solvent and the final dimension of the PNPs since by using the solvents of highest viscosity (DMSO and DMF) it has been produced the smallest nanoparticles (Supplementary information file—Fig. S1). Similarly, the particle size does not correlate properly with water–solvent interfacial

tension (Supplementary information file—Fig. S2). Huge differences in $\Delta\gamma_{water-solvent}$ led to similar mean nanoparticle size (comparing data for DMSO, DMF and acetonitrile). Furthermore, in the case of the highest $\Delta\gamma_{water-solvent}$ (acetone) it was not found the largest PNPs. These results made us to believe that the nucleation-and-growth mechanism is supposed to prevail the Gibbs–Marangoni effect in such conditions (polymer concentration 1.4 mg mL^{-1}; solvent:water ratio 0.4). Therefore, it is possibly the rate of diffusion of the solvent into the antisolvent phase the main responsible for the final dimension of the PNPs. The rate of diffusion is related to the solvent–water thermodynamic affinity. Quantitatively, the solvent–water compatibility can be expressed by the interaction parameter ($\chi_{solvent-water}$) based on the Hildebrand solubility parameters δ (Table 2).

$$\chi_{solvent-water} = \frac{V_{water}}{RT}(\delta_{solvent} - \delta_{water})^2 \quad (6)$$

The parameter $\chi_{solvent-water}$ describes the interaction between the molecules of water and the molecules of the organic solvent and V_{water} stands for the molar volume of water (calculated based on its molar mass and density), being R the gas constant, T the absolute temperature and δ_{water} and $\delta_{solvent}$ the solubility parameters of the water and organic solvent, respectively.

The mean particle size was plotted as a function of the interaction parameter and the profile is given in Fig. 8A. In such case, there is a consistent tendency of size increase as a function of $\chi_{water-solvent}$, where the lower the $\chi_{water-solvent}$ the smaller the PNPs. The mean particle size increases in the following order: DMSO–DMF < acetonitrile < acetone < THF. This is the trend from the smallest towards the highest $\chi_{water-solvent}$. The results suggest that a high water–solvent affinity allows a high water–solvent blending rate leading to the formation of smaller PNPs therefore confirming that water–solvent miscibility is of chief importance in the diffusion-stranding phenomenon and thus in the formation of PNPs by nanoprecipitation. Furthermore, the same tendency has been observed as a function of the solvent dielectric constant (Supplementary information file—Fig. S3) where the smaller the $\Delta\varepsilon_{water-solvent}$ the smaller the PNPs.

Indeed the manufacturing of EUDRAGIT® L 100-55 (an anionic copolymer based on methacrylic acid and ethyl acrylate) PNPs by using the nanoprecipitation protocol starting from different solvents (ethanol, DMSO, isopropyl alcohol, acetone and ethyl lactate) led to a similar trend [53]. The same was also observed in the manufacturing of pegylated PLGA NPs [46]. Additionally, considering that the relation between $\chi_{water-solvent}$ and particle size is not linear, possibly the mechanical and nucleation phenomena take place simultaneously during the formation of the PNPs. The polydispersity index (Fig. 8B) and the ζ-potential (Fig. 8C) of the produced PNPs seem not to be systematically affected by the nature of the organic solvent. The average values were always below 0.15 and −30.0 mV, respectively.

The manufacturing of PCL and PBS:PBDL polymeric NPs have also been performed in DMF, acetone and THF. The results compared to PLGA are given in Table 3.

As it can be noticed, whatever the polymer, the size increased in the order DMF < acetone < THF. We consider these results of fundamental importance because they clearly confirm that solvent–water interaction is one of the main factors affecting the mean PNPs size independently of the biodegradable polymer nature. Furthermore, the ζ-potential of PNPs prepared in THF is more negative independently of the polyester, which is probably due to the higher number of aggregation of PNPs prepared in such a solvent. Moreover, although the same trend has been observed, clearly the PCL NPs are substantially larger than the others at any solvent. Such behavior is probably due to the higher hydrophobicity of PCL compared to the other biodegradable polymers (Table 3).

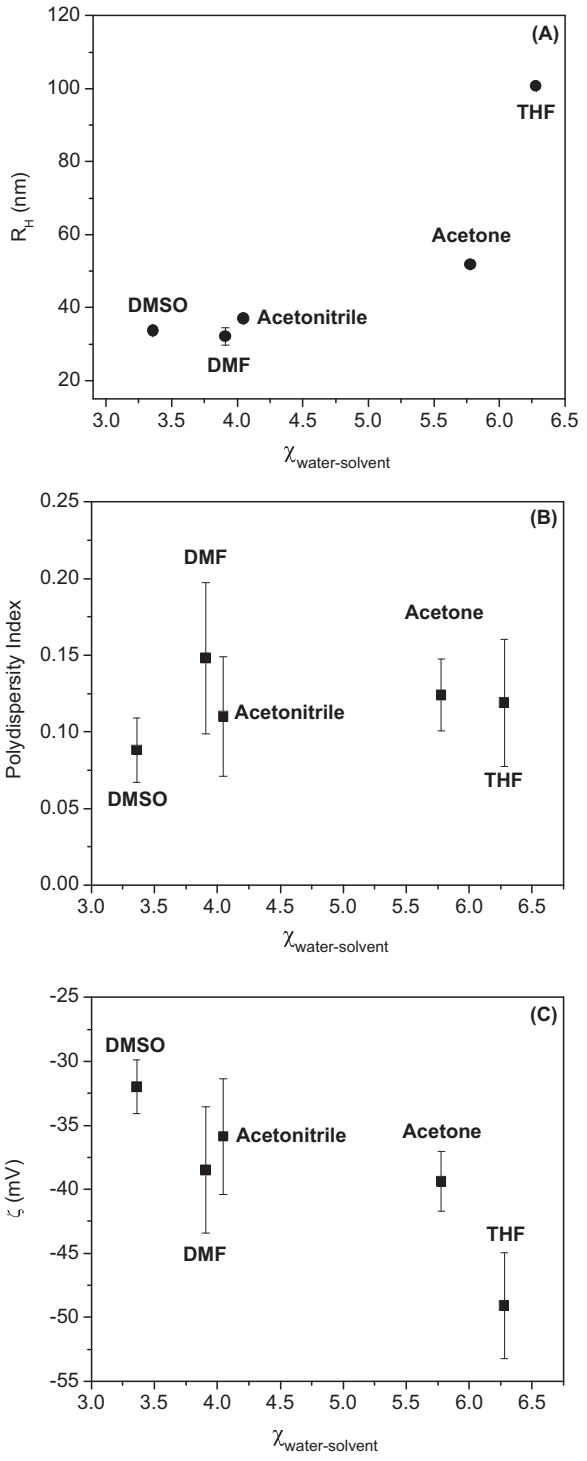

Fig. 8. Influence of the water–solvent interaction parameter ($\chi_{water-solvent}$) on the mean nanoparticle size (A), polydispersity index (B) and ζ-potential (C) of PLGA01 nanoparticles prepared by nanoprecipitation. The polymer concentration and the solvent:water ratio were preset to 1.4 mg.mL^{-1} and 0.4 mg.mL^{-1}, respectively.

The polymer–solvent interactions and the viscosity of the organic phase, on the other hand, seem to have a minor influence on the final particle size.

Finally, although we were not able to detect a linear correlation between interaction parameter ($\chi_{water-solvent}$) and mean particle size, we have evidenced that the size of the PNPs can be easily and precisely tuned by using mixture of solvents as the organic phase. By mixing DMF and THF we were able to linearly tune

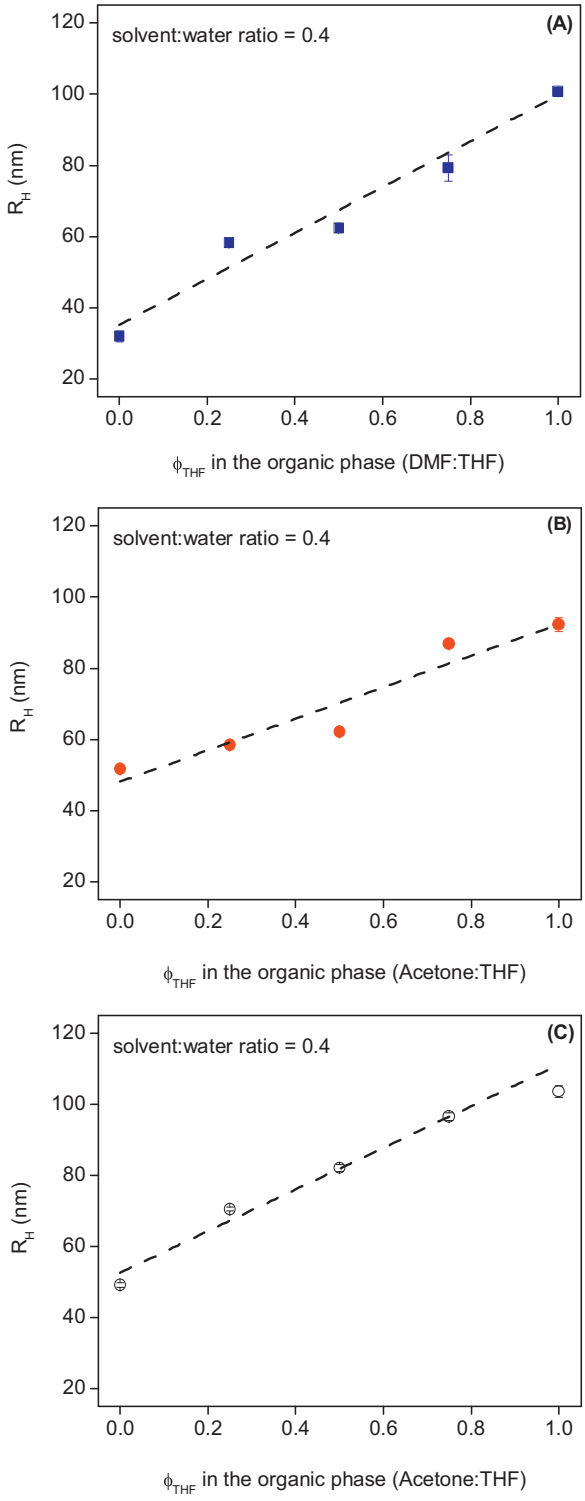

Fig. 9. R_H of PLGA01 polymeric nanoparticles prepared by nanoprecipitation as a function of the ϕ_{THF} in DMF:THF (A) and acetone:THF mixtures (B). R_H of PBS:PBDL polymeric nanoparticles prepared by nanoprecipitation as a function of the ϕ_{THF} in acetone:THF mixtures (C). The polymer concentration and organic solvent:water ratio were preset to 1.4 mg mL^{-1} and 0.4 mg mL^{-1}, respectively.

the size of PLGA01 PNPs from the lowest (~30 nm) to its highest value (~100 nm). The same procedure has been employed in mixtures of acetone and THF and the results are given in Fig. 9B. In all the cases, the organic solvent:water ratio was kept fixed at 0.4 and only the composition of the organic phase was systematically changed. By using DMF:THF mixtures, there is a simple relationship between size and the ratio between the employed solvents. The same behavior was also evidenced by manufacturing PNPs starting from different biodegradable polymers. The representative example for PBS:PBDL NPs is given in Fig. 9C. Similar to the results in pure solvent, the polydispersity index and the ζ-potential of the produced PNPs do not seem to be systematically affected by the nature of the organic phase (results not shown).

To this end, it is believed that we brought herein enough experimental evidences to suggest that the mean particle size depends chiefly on solvent:antisolvent and antisolvent:polymer interactions rather the solvent–polymer interactions.

Table 3
Mean particle size (R_H), polydispersity index and zeta-potential (ζ) of a variety of polymeric nanoparticles prepared by nanoprecipitation at different starting organic solvents.

Polymer	Solvent	R_H (nm)	Polydispersity index	ζ (mV)
PBS:PBDL	DMF	25.1	0.23	−36.8
	Acetone	49.1	0.03	−33.9
	THF	103.8	0.13	−37.4
PLGA01	DMF	29.9	0.27	−38.5
	Acetone	52.1	0.12	−39.4
	THF	109.7	0.05	−49.1
PLGA03	DMF	58.1	0.04	−32.4
	Acetone	70.8	0.09	−24.6
	THF	131.1	0.09	−33.7
PCL	DMF	63.9	0.24	−28.7
	Acetone	88.6	0.10	−23.0
	THF	212.1	0.28	−52.5

4. Conclusions

Surfactant-free PLGA nanoparticles with hydrodynamic radius (R_H) ranging from 28.5 nm to 128.5 nm were successfully obtained through nanoprecipitation by controlling a variety of physicochemical parameters. The size of the produced PLGA PNPs can be controlled by adjusting the polymer concentration, the choice of organic solvent, mixing different solvent or by changing temperature and ionic strength. By optimizing such parameters sub-100 nm uniform PNPs can be generated through nanoprecipitation which allows the ability to scale-up production. The size of the PNPs is mainly dependent on the organic solvent used and the polymer nature. Indeed, the solvent–water interaction is the main factor affecting the mean PNPs size independently of the biodegradable polymer. On the other hand, the polymer–solvent interaction does not seem to play a substantial role in the dimension of the polymer colloids. Finally, it has been also shown that the size of the PNPs can be precisely and linearly tuned by using solvent mixtures as the organic phase without affecting their polydispersity index and ζ-potential.

Acknowledgements

This work has been sponsored by FAPESP (Grant No. 2012/14087-8) and GACR (202/09/2078). A.M.O thanks the fellowship granted by FAPESP (Grant No. 2012/17841-5). The CEM at UFABC is acknowledged for the accessibility to the Malvern light scattering equipment. The LNLS is acknowledged for supplying the SAXS beam time (proposal 12536). Dr. Miroslav Slouf is acknowledged for helping during TEM measurements. A.J and E.J thank the fellowships granted by the Charles University.

Appendix A. Supplementary data

Supplementary data associated with this article can be found, in the online version, at http://dx.doi.org/10.1016/j.colsurfa.2013.08.056.

References

[1] W. Sun, H. Wang, C. Xie, Y. Hu, X. Yang, H. Xu, An attempt to directly trace polymeric nanoparticles in vivo with electron microscopy, J. Controlled Release 115 (2006) 259–265.
[2] A. Castaldello, E. Brocca-Cofano, R. Voltan, C. Triulzi, G. Altavilla, M. Laus, DNA prime and protein boost immunization with innovative polymeric cationic core-shell nanoparticles elicits broad immune responses and strongly enhance cellular responses of HIV-1 tat DNA vaccination, Vaccine 24 (2006) 5655–5669.
[3] T. Houchin-Ray, K. Whittlesey, L. Shea, Spatially patterned gene delivery for localized neuron survival and neurite extension, Mol. Ther. 15 (2007) 705–712.
[4] D. Peer, J.M. Karp, S. Hong, O.C. Farokhzad, R. Margalit, R. Langer, Nanocarriers as an emerging platform for cancer therapy, Nat. Nanotechnol. 2 (2007) 751–760.
[5] K.L. Wooley, M. Elsabahy, Design of polymeric nanoparticles for biomedical delivery applications, Chem. Soc. Rev. 41 (2012) 2545–2561.
[6] L.Y.T. Chou, K. Ming, W.C.W. Chan, Strategies for the intracellular delivery of nanoparticles, Chem. Soc. Rev. 40 (2011) 233–245.
[7] L. Zhang, J.M. Chan, F.X. Gu, J.W. Rhee, A.Z. Wang, A.F. Radovic-Moreno, F. Alexis, R. Langer, O.C. Farokhzad, Self-assembled lipid-polymer hybrid nanoparticles: a robust drug delivery platform, ACS Nano 2 (2008) 1696–1702.
[8] N. Kamaly, Z. Xiao, P.M. Valencia, A.F. Radovi-Moreno, O.C. Farokhzad, Targeted polymeric therapeutic nanoparticles: design, development and clinical translation, Chem. Soc. Rev. 41 (2012) 2971–3010.
[9] M.M. Yallapu, B.K. Gupta, M. Jaggi, S.C. Chauhan, Fabrication of curcumin encapsulated PLGA nanoparticles for improved therapeutic effects in metastatic cancer cells, J. Colloid Interface Sci. 351 (2010) 19–29.
[10] U. Bilati, E. Allémann, E. Doelker, Development of a nanoprecipitation method intended for the entrapment of hydrophilic drugs into nanoparticles, Eur. J. Pharm. Sci. 24 (2005) 67–75.
[11] M. Beck-Broichsitter, E. Rytting, T. Lebhardt, X. Wang, T. Kissel, Preparation of nanoparticles by solvent displacement for drug delivery: a shift in the ouzo region upon drug loading, Eur. J. Pharm. Sci. 41 (2010) 244–253.
[12] H. Xie, W. Smith, Fabrication of PLGA nanoparticles with a fluidic nanoprecipitation system, J. Nanobiotechnol. 8 (2010) 18.
[13] M.S. Shive, J.M. Anderson, Biodegradation and biocompatibility of PLA and PLGA microspheres, Adv. Drug Delivery Rev. 28 (1997) 5–24.
[14] M.S. Muthu, M.K. Rawat, A. Mishra, S. Singh, Preparation and characterization of nanoparticles containing an atypical antipsychotic agent, Nanomedicine 5 (2009) 323–333.
[15] M. Chorny, I. Fishbein, H.D. Danenberg, G. Golomb, Study of the drug release mechanism from tyrphostin AG-1295-loaded nanospheres by in situ and external sink methods, J. Controlled Release 83 (2002) 401–414.
[16] R. Gref, Y. Minamitake, M.T. Peracchia, V. Trubetskoy, V. Torchilin, R. Langer, Biodegradable long-circulating polymeric nanospheres, Science 263 (1994) 1600–1603.
[17] G. Gaucher, R.H. Marchessault, J. Leroux, Polyester-based micelles and nanoparticles for the parenteral delivery of taxanes, J. Controlled Release 143 (2010) 2–12.
[18] T. Govender, S. Stolnik, M.C. Garnett, L. Illum, S.S. Davis, PLGA nanoparticles prepared by nanoprecipitation: drug loading and release studies of a water soluble drug, J. Controlled Release 57 (1999) 171–185.
[19] M.G. Cascone, P.M. Pot, L. Lazzeri, Z. Zhu, Release of dexamethasone from PLGA nanoparticles entrapped into dextran/poly(vinyl alcohol) hydrogels, J. Mater. Sci. Mater. Med. 13 (2002) 265–269.
[20] J. Fang, H. Nakamura, H. Maeda, The EPR effect: unique features of tumor blood vessels for drug delivery, factors involved, and limitations and augmentation of the effect, Adv. Drug Delivery Rev. 63 (2011) 136–151.
[21] M.E. Fox, F.C. Szoka, J.M. Fréchet, Soluble polymer carriers for the treatment of cancer: the importance of molecular architecture, Acc. Chem. Res. 42 (2009) 1141–1151.
[22] K. Cho, X. Wang, S. Nie, Z. Chen, D.M. Shin, Therapeutic nanoparticles for drug delivery in cancer, Clin. Cancer Res. 14 (2008) 1310–1316.
[23] H. Cabral, Y. Matsumoto, K. Mizuno, Q. Chen, M. Murakami, M. Kimura, Y. Terada, M.R. Kano, K. Miyazono, M. Uesaka, N. Nishiyama, K. Kataoka, Accumulation of sub-100 nmpolymeric micelles in poorly permeable tumours depends on size, Nat. Nanotechnol. 6 (2011) 815–823.
[24] D.E. Owens, N.A. Peppas, Opsonization, biodistribution, and pharmacokinetics of polymeric nanoparticles, Int. J. Pharm. 307 (2006) 93–102.
[25] H.S. Choi, W. Liu, P. Misra, E. Tanaka, J.P. Zimmer, B. Itty-Ipe, M.G. Bawendi, J.V. Frangioni, Renal clearance of quantum dots, Nat. Biotechnol. 25 (2007) 1165–1170.
[26] M. Longmire, P.L. Choyke, H. Kobayashi, Clearance properties of nano-sized particles and molecules as imaging agents: considerations and caveats, Nanomedicine 3 (2008) 703–717.
[27] W. Jiang, B.Y.S. Kim, J.T. Rutka, W.C.W. Chan, Nanoparticle-mediated cellular response is size-dependent, Nat. Nanotechnol. 3 (2008) 145–150.
[28] S.E. Gratton, P.A. Ropp, P.D. Pohlhaus, J.C. Luft, V.J. Madden, M.E. Napier, J.M. DeSimone, The effect of particle design on cellular internalization pathways, PNAS 105 (2008) 11613–11618.
[29] S.M. Moghimi, S.S. Davis, Innovations in avoiding particle clearance from blood by Kupffer cells—cause for reflection, Crit. Rev. Ther. Drug Carrier Syst. 11 (1994) 31–59.
[30] J.P. Rao, E. Kurt, K.E. Geckeler, Polymer nanoparticles: preparation techniques and size-control parameters, Prog. Polym. Sci. 36 (2011) 887–913.
[31] C. Zhang, V.J. Pansare, R.K. Prud'homme, R.D. Priestley, Flash nanoprecipitation of polystyrene nanoparticles, Soft Matter 8 (2012) 86–93.
[32] S.M. D'Addio, R.K. Prud'homme, Controlling drug nanoparticle formation by rapid precipitation, Adv. Drug Delivery Rev. 63 (2011) 417–426.
[33] H. Fessi, F. Puisieux, J.P. Devissaguet, N. Ammoury, S. Benita, Nanocapsule formation by interfacial polymer deposition following solvent displacement, Int. J. Pharm. 55 (1989) R1–R4.
[34] C.E. Mora-Huertas, H. Fessi, A.A. Elaissari, Influence of process and formulation parameters on the formation of submicron particles by solvent displacement and emulsification–diffusion methods critical comparison, Adv. Colloid Interface Sci. 163 (2011) 90–122.
[35] F. Lince, D.L. Marchisio, A.A. Barresi, Strategies to control the particle size distribution of poly-*e*-caprolactone nanoparticles for pharmaceutical applications, J. Colloid Interface Sci. 322 (2008) 505–515.
[36] J. Aubry, F. Ganachaud, J.P. Cohen-Addad, B. Cabane, Nanoprecipitation of polymethylmethacrylate by solvent shifting: 1. Boundaries, Langmuir 25 (2009) 1970–1979.
[37] K.S. Soppimath, T.M. Aminabhavi, A.R. Kulkarni, W.E. Rudzinski, Biodegradable polymeric nanoparticles as drug delivery devices, J. Controlled Release 70 (2001) 01–20.
[38] A. Jager, D. Gromadzki, E. Jager, F.C. Giacomelli, A. Kozlowska, L. Kobera, J. Brus, B. Rihova, M. El Fray, K. Ulbrich, P. Stepánek, Novel "soft" biodegradable nanoparticles prepared from aliphatic based monomers as a potential drug delivery system, Soft Matter 8 (2012) 4343–4354.
[39] P. Stepánek, in: W. Brown (Ed.), Dynamic Light Scattering: The Method and Some Applications, Oxford Science Publications, Oxford, 1993.
[40] P. Stepanek, C. Konak, Quasielastic light-scattering from polymers, colloids and gels, Adv. Colloid Interface Sci. 21 (1984) 195–274.
[41] J. Jakes, Regularized positive exponential sum (REPES) program—a way of inverting Laplace transform data obtained by dynamic light scattering, Collect. Czech. Chem. Commun. 60 (1995) 1781–1797.
[42] F. Quaglia, L. Ostacolo, G. De Rosa, M.I. La Rotonda, M. Ammendola, G. Nesse, G. Maglio, R. Palumbo, C. Vauthier, Nanoscopic core-shell drug carriers made of amphiphilic triblock and star-diblock copolymers, Int. J. Pharm. 324 (2006) 56–66.
[43] I.Y. Perevyazko, J.T. Delaney Jr., A. Vollrath, G.M. Pavlov, S. Schubert, U.S. Schubert, Examination and optimization of the self-assembly of biocompatible, polymeric nanoparticles by high-throughput nanoprecipitation, Soft Matter 7 (2011) 5030–5035.
[44] S. Patil, A. Sandberg, E. Heckert, W. Self, S. Seal, Protein adsorption and cellular uptake of cerium oxide nanoparticles as a function of zeta potential, Biomaterials 28 (2007) 4600–4607.
[45] M.R. Lorenz, V. Holzapfel, A. Musyanovych, K. Nothelfer, P. Walther, H. Frank, K. Landfester, H. Schrezenmeier, V. Mailänder, Uptake of functionalized, fluorescent-labeled polymeric particles in different cell lines and stem cells, Biomaterials 27 (2006) 2820–2828.
[46] J. Cheng, B.A. Teply, I. Sherifi, J. Sung, G. Luther, F.X. Gu, E. Levy-Nissenbaum, A.F. Radovic-Moreno, R. Langer, O.C. Farokhzad, Formulation of functionalized PLGA-PEG nanoparticles for in vivo targeted drug delivery, Biomaterials 28 (2007) 869–876.
[47] M.E. Gindy, A.Z. Panagiotopoulos, R.K. Prud'homme, Composite block copolymer stabilized nanoparticles: simultaneous encapsulation of organic actives and inorganic nanostructures, Langmuir 24 (2008) 83–90.
[48] K. Srinivas, J.W. King, Supercritical carbon dioxide and subcritical water: complementary agents in the processing of functional foods, in: J. Smith, E. Charter (Eds.), Functional Food Product Development, Blackwell Publishing Ltd, Oxford, 2010, pp. 39–78.
[49] C.M. Hansen, Hansen Solubility Parameters: A User's Handbook, second ed., CRC Press Taylor and Francis Group, Boca Raton, FL, 2007.
[50] C. Gavory, A. Durand, J.L. Six, C. Nouvel, E. Marie, M. Leonard, Polysaccharide-covered nanoparticles prepared by nanoprecipitation, Carbohydr. Polym. 84 (2011) 133–140.
[51] C. Bordes, V. Fréville, E. Ruffin, P. Marote, J.Y. Gauvrit, S. Briançon, P. Lantéri, Determination of poly(ε-caprolactone) solubility parameters: application to solvent substitution in a microencapsulation process, Int. J. Pharm. 383 (2010) 236–243.
[52] S. Schenderlein, M. Lück, B.W. Müller, Partial solubility parameters of poly(D,L-lactide-*co*-glycolide), Int. J. Pharm. 286 (2004) 19–26.
[53] S. Galindo-Rodriguez, E. Allémann, H. Fessi, E. Doelker, Physicochemical parameters associated with nanoparticle formation in the salting-out, emulsification–diffusion, and nanoprecipitation methods, Pharm. Res. 21 (2004) 1428–1439.

Soft Matter

Dynamic Article Links

Cite this: *Soft Matter*, 2012, **8**, 4343

www.rsc.org/softmatter

PAPER

Novel "soft" biodegradable nanoparticles prepared from aliphatic based monomers as a potential drug delivery system†

Alessandro Jäger,*[a] Daniel Gromadzki,[a] Eliézer Jäger,[a] Fernando Carlos Giacomelli,[b] Agnieszka Kozlowska,[c] Libor Kobera,[a] Jiří Brus,[a] Blanka Říhová,[d] Miroslawa El Fray,[c] Karel Ulbrich[a] and Petr Štěpánek*[a]

Received 24th November 2011, Accepted 6th February 2012
DOI: 10.1039/c2sm07247e

The search for new biomaterials intended for biomedical applications has considerably intensified in recent years. Herein, the synthesis and characterization of a new aliphatic biodegradable copolyester named PBS/PBDL (poly(butylene succinate-*co*-butylene dilinoleate)) is reported. Surfactant-free, narrowly distributed, nanosized spherical particles (R_H < 60 nm) have been produced from the biodegradable material by applying a single-step nanoprecipitation protocol. Their structure was characterized in detail by employing a variety of scattering techniques and transmission electron microscopy (TEM). Combined SLS and DLS measurements suggested that the nanoparticles comprise a porous core conferring a non-compact characteristic. Their porosity enables water to be entrapped which is responsible for their pronounced stability and relatively fast degradation as followed by size exclusion chromatography (SEC). The polymeric nanoparticles could be loaded with the hydrophobic model drug paclitaxel (PTX) with an encapsulation efficiency of ~95% and drug loading content of ~6–7% $w_{drug}/w_{polymer}$. The drug release was followed by HPLC and scattering measurements (DLS, SLS and SAXS). The drug encapsulation and release modifies the inner structure of the nanoparticles, which holds a large amount of entrapped water in the drug-free condition. PTX encapsulation leads to replacement of the entrapped water by the hydrophobic model drug and to shrinking of the nanoparticles, probably due to favorable drug–polymer hydrophobic interactions. Cell viability experiments demonstrated that the nanoparticles are biocompatible and non-toxic, making them potentially useful for applications in nanomedicine.

1. Introduction

The use of pharmaceutical polymeric nanocarriers has become one of the most important areas of nanomedicine. Particularly, the manufacturing of efficient drug delivery systems that enable drug targeting and specific delivery of difficult-to-deliver molecules has been extensively investigated.[1,2] Thanks to the advances in polymer chemistry and polymer colloids, it is now possible to prepare polymeric nanoparticles with unique, finely tuned properties that are required to achieve the goal of drug targeting.[3–5]

Over the past decades, the use of biodegradable polymers in the preparation of pharmaceutical formulations and biomedical devices has increased dramatically. Among these the most promising applications are the ones focused on the development of controlled drug delivery systems.[6,7] The use of biodegradable polymers is very attractive because controlled drug release can be optimized by suitable degradation strategies and it allows clearance of the polymeric material from the body, avoiding its accumulation and possible toxicity.[8,9] Nevertheless, the available biodegradable polymers that are suitable for biomedical applications are limited due to the essential requirement of biocompatibility. Furthermore, the degradation mechanism must also not lead to the formation of poisonous products.[10]

Among the FDA-approved polymers, the aliphatic polyesters such as poly(caprolactone) (PCL), polylactic acid (PLA) and poly(lactic-*co*-glycolic acid) (PLGA) have been extensively and routinely used in the manufacturing of drug delivery devices[11] because of their good hydrolyzability, biocompatibility and drug release properties.[9,12] In addition, polybutylene succinate (PBS) is also an important commercially available

[a]*Institute of Macromolecular Chemistry, Academy of Sciences of the Czech Republic, Heyrovsky Sq. 2, 162 06 Prague 6, Czech Republic. E-mail: jager@imc.cas.cz; stepanek@imc.cas.cz; Tel: +420 296 809211; +420 296 809322*

[b]*Centro de Ciências Naturais e Humanas, Universidade Federal do ABC, 09210-170 Santo André, Brazil*

[c]*Division of Biomaterials and Microbiological Technologies Polymer Institute, West Pomeranian University of Technology Szczecin, ul. Pulaskiego 10, 70-322 Szczecin, Poland*

[d]*Institute of Microbiology, Academy of Sciences of the Czech Republic, v. v. i., Vídeňská 1083, 142 20 Prague 4, Czech Republic*

† Electronic supplementary information (ESI) available. See DOI: 10.1039/c2sm07247e

biodegradable aliphatic polyester derived from fatty C-4 compounds.[13–15] Recently, its copolymerization with different comonomers led to novel biomedical materials exhibiting particular biodegradation behaviors and good biocompatibility.[16–18] The absence of cytotoxic degradation products, *e.g.* succinic acid is an intermediate in the TCA cycle (tricarboxylic acid cycle, citric acid cycle), makes PBS copolyesters prospective candidates aiming the development of drug delivery structures.[19] Furthermore, fatty acids (FA) are suitable components for the preparation of biodegradable polymers since they are hydrophobic compounds that naturally occur in the body. Consequently, they might retain encapsulated hydrophobic drugs *via* hydrophobic interactions when used as drug nanocarriers.[20] Heretofore, different fatty acid monomers obtained from natural sources have been suggested as starting materials to produce devices focusing on biomedical applications.[21] Among those, dilinoleic acid (DLA) is dimerized linoleic acid and it is a suitable monomer for step growth polycondensation resulting in copolymers of numerous structures.[22–25] Recently, multiblock copolymers containing DLA monomer units were proposed as biomaterials for bone and tissue engineering that demonstrated good biocompatibility.[26,27] Although copolymers containing FA monomers as building blocks were extensively proposed in the literature as devices in many biomedical applications, their application as nanocarriers for drug release was not reported to date. Hence, DLA copolymer-based biodegradable and biocompatible polyesters can render very interesting biomaterials that are useful as nanocarriers and they deserve to be investigated for such a purpose.

Herein a new biodegradable and biocompatible copolyester composed of succinic acid (SA), butanediol (BD) and DLA as building block monomers is proposed for the production of polymeric nanocarriers. The copolyester was synthesized by environmentally benign melt polycondensation[28] using commercially available "green" monomers and characterized in detail by employing standard techniques. By using the novel copolyester, sub-120 nm surfactant-free nanocarriers have been prepared by a well-known nanoprecipitation protocol. The nanoprecipitation constitutes an easy and reproducible procedure that has been widely used in the preparation of polyester-based nanoparticles.[9,29,30] Among its advantages are: *i*) large amounts of hazardous solvents are avoided; *ii*) narrowly distributed nanosized spherical particles can be obtained; *iii*) external energy sources are unnecessary and *iv*) the process can be easily scaled-up.[9,31,32] Their biodegradability, biocompatibility and controlled drug release properties have been further verified by using paclitaxel (PTX) as the model drug. The drug encapsulation and drug release changes the inner structure of the polymeric nanoparticles and this issue has been deeply detailed and discussed throughout the manuscript.

2. Experimental

2.1 Materials and reagents

Dilinoleic acid (DLA) Pripol 1009 (Croda Coatings & Polymers), 1,4-butanediol (BD) (BASF), succinic acid (SA) (Aldrich Chemie) and acetone (Merck) were used as received. The water consumed was ultrapure MilliQ®.

2.2 Synthesis of the copolyester

The copolyester PBS/PBDL was synthesized by the typical melt polycondensation protocol.[28] The procedures were carried out on a stainless steel pressure-vacuum reactor. The esterification was conducted under vigorous stirring in presence of a magnesium–titanate organometallic complex (Mg–Ti) as catalyst and upon preset temperature ramping from 100 °C to 200 °C (heating rate = 1.5 °C min^{-1}). The reaction was stopped when the acid value was less than 2 mg KOH g^{-1}.

The polycondensation reaction was carried out at 245–250 °C, ~0,4 hPa and in the presence of the Mg–Ti catalyst. The reaction was considered complete when the observed power consumption of the stirrer motor signaled that the polymer had obtained the highest melt viscosity. The reaction mass was extruded by means of compressed nitrogen. The copolyester was purified by dissolution in chloroform and further precipitation in methanol. The poly(butylene succinate-*co*-butylene dilinoleate) herein referred to as PBS/PBDL was synthesized to have a segment composition of 50/50 wt% (Fig. 1).

2.3 Characterization of the copolyester

2.3.1. NMR characterization. ^{1}H NMR and ^{13}C NMR spectra were obtained on a Bruker AMX-300 spectrometer at 25 °C operating at 300.1 MHz (^{1}H NMR) or 75.5 MHz (^{13}C NMR). The copolyester was dissolved in deuterated chloroform ($CDCl_3$) and the spectra were internally referenced to tetramethylsilane (TMS). Sixty-four scans for ^{1}H NMR and 1000–10 000 scans for ^{13}C NMR were acquired with 32 K and 62 K data points and delay times of 1 and 2 s respectively. Quantitative ^{1}H NMR spectra were recorded with pulse widths of 6 ms ($\pi/3$) and delay time of 20 s. For ^{13}C NMR, the pulse and spectral widths were 4.3 ms ($\pi/2$) and 18 kHz respectively.

2.3.2. Size exclusion chromatography (SEC). The number-average molar mass (M_n) and molar mass distribution (M_w/M_n) values of the novel synthesized copolyester and the same quantities during the degradability studies were determined by SEC (Deltachrom pump, Watrex Comp., autosampler Midas, Spark Instruments, two columns with PL gel MIXED-B LS (10 μm), separating in the range of molar masses approximately 400–1 × 10^7 g mol^{-1}). Tetrahydrofuran (THF) was used as the mobile phase at flow-rate 0.5 mL min^{-1}. The injection-loop volume was 0.1 mL. Measurements were performed with triple viscosity/concentration/light-scattering detection. The set was connected to a light-scattering photometer DAWN DSP-F (Wyatt Technology Corp.) measuring at 18 angles of observation, a modified differential viscometer Viscotek model TDA 301 (without internal light scattering and concentration detectors) and a differential refractometer Shodex RI 71. The data were accumulated and processed using the Astra and triSEC softwares. The evaluation of the triple-detection data is detailed elsewhere.[33]

2.4 Preparation of the nanoparticles (NPs)

The polymeric nanoparticles were prepared by using a nanoprecipitation protocol in water and varying the copolymer concentration from 0.25 to 1.00 wt%. The PBS/PBDL copolyester was first completely dissolved in acetone at 40 °C and

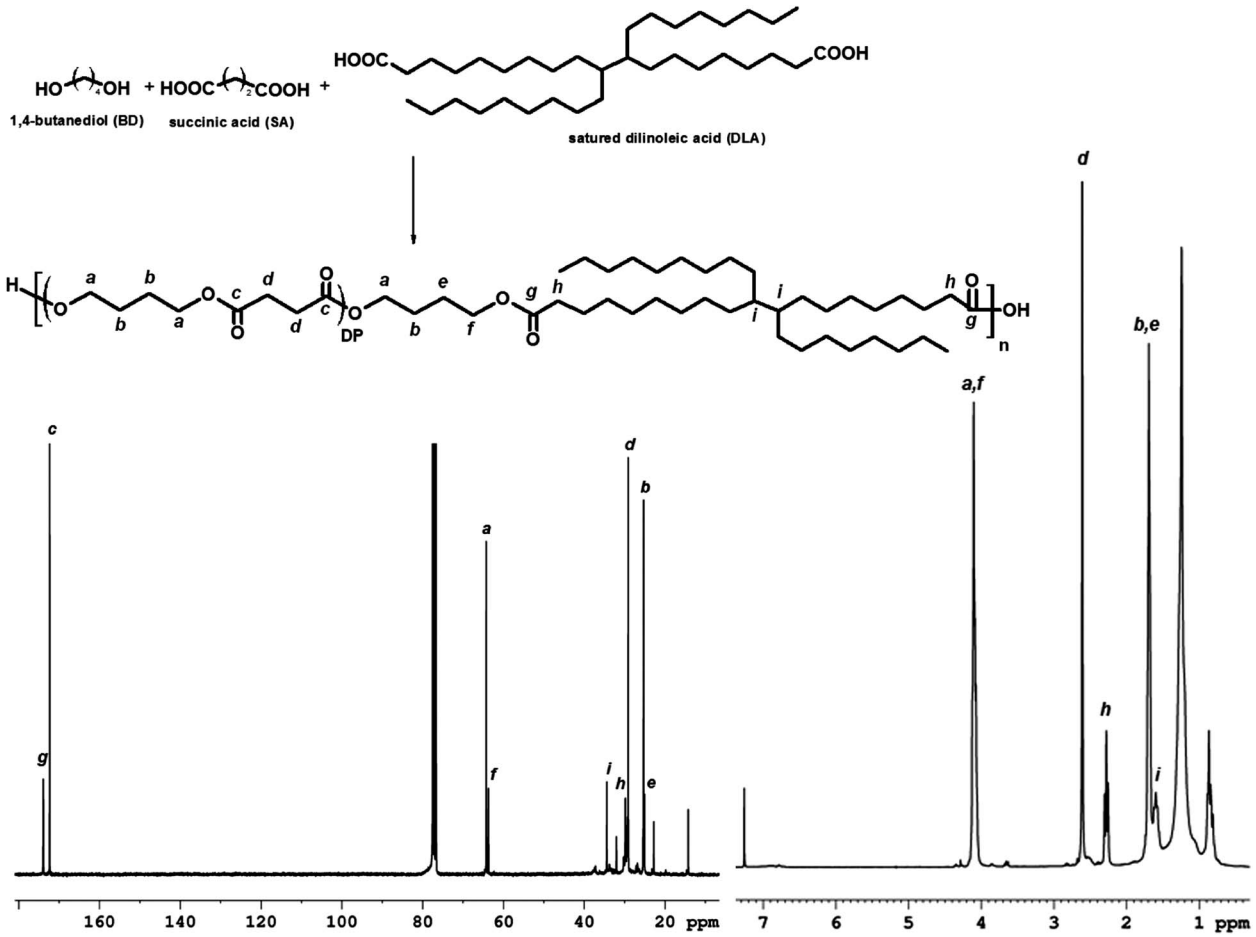

Fig. 1 Structure, ^{1}H (right) and ^{13}C (left) NMR of the poly(butylene succinate-*co*-butylene dilinoleate) aliphatic copolyester.

subsequently the organic phase was added drop-wise (EW-74900-00, Cole-Parmer®) to pure water (20 mL) under stirring (Ultra-Turrax T25, IKA, Germany). The organic solvent was further removed by evaporation under reduced pressure at room temperature and the aqueous solution was concentrated to 5 mL. The prepared NPs were used immediately or stored at 4 °C.

2.5 Characterization of the nanoparticles

2.5.1. Dynamic Light Scattering (DLS). The DLS measurements were performed using an ALV CGE laser goniometer consisting of a 22 mW HeNe linear polarized laser operating at a wavelength ($\lambda = 632.8$ nm), an ALV 6010 correlator, and a pair of avalanche photodiodes operating in the pseudo cross-correlation mode. The samples were loaded into 10 mm diameter glass cells and maintained at 25 ± 1 °C. The data were collected using the ALV Correlator Control software and the counting time was 30 s. In order to avoid multiple light scattering, the samples were diluted 100 times before the measurements.[34] The measured intensity correlation functions $g_2(t)$ were analyzed using the algorithm REPES (incorporated in the GENDIST program)[35] resulting in the distributions of relaxation times shown in equal area representation as $\tau A(\tau)$. The mean relaxation time or relaxation frequency ($\Gamma = \tau^{-1}$) is related to the diffusion coefficient (D) of the nanoparticles as $D = \dfrac{\Gamma}{q^2}$ where $q = \dfrac{4\pi n \sin(\theta/2)}{\lambda}$ is the scattering vector being n the refractive index of the solvent and θ the scattering angle. The hydrodynamic radius (R_H) or the distributions of R_H were calculated[36] by using the well-known Stokes–Einstein relation:

$$R_H = \frac{k_B T}{6\pi\eta\, D} \quad (1)$$

where k_B is the Boltzmann constant, T is the absolute temperature and η is the viscosity of the solvent.

2.5.2. Static light scattering (SLS). In the SLS mode, the scattering angle was varied from 30 to 150° with a 10° stepwise increase. The absolute light scattering is related to the weight-averaged molar mass ($M_{w(NP)}$) and to the radius of gyration (R_G) of the nanoparticles by the Zimm formalism represented as:

$$\frac{Kc}{R_\theta} = \frac{1}{M_w}\left(1 + \frac{R_G^2 q^2}{3}\right) \quad (2)$$

where K is the optical constant which includes the square of the refractive index increment (dn/dc), R_θ is the excess normalized scattered intensity (toluene was applied as standard solvent) and c is the polymer concentration given in mg mL^{-1}. The refractive index increment (dn/dc) of the PBS/PBDL NPs in pure water (0.153 mL g^{-1}) was determined using a Brice–Phoenix differential refractometer operating at $\lambda = 632.8$ nm.

2.5.3 Electrophoretic Light Scattering (ELS). The ELS measurements were employed in order to determine the average zeta potential (ζ) of the nanoparticles, which was done using the Zetasizer NanoZS instrument (Malvern Instruments, UK). The equipment measures the electrophoretic mobility (U_E) of the nanoparticles and converts the value to the ζ-potential (mV) through Henry's equation. Henry's function was calculated through the Smoluchowski approximation.

2.5.4. Small Angle X-ray Scattering (SAXS). The SAXS experiments were conducted at the SWING SAXS beamline of the Synchrotron SOLEIL (Gif-sur-Yvette, France). The samples were loaded into sealed borosilicate capillaries (~2 mm diameter). The collimated beam ($\lambda = 1.033$ Å) crossed the samples towards an evacuated flight tube and was scattered to a 17 cm × 17 cm PCCD-170170 CCD Detector (Aviex). The sample-to-detector distance was chosen in such way that the q-range 0.02–2.1 nm^{-1} could be covered. At each measurement, 10 frames of 0.1s exposure time were collected. They were further normalized by the sample transmission and subsequently averaged and converted to $I(q)$ *vs.* q profiles using the Foxtrot software. The resulting $I(q)$ *vs.* q scattering curves were corrected by the subtraction of the scattering of the pure solvent and they could be fitted by using the form factor of homogeneous spheres. The fitting procedures were performed using the SASfit software which makes use the least-squares fitting approach for minimizing the chi squared (χ^2) parameter. The SASfit software package was developed by J. Kohlbrecher.[37]

2.5.5. Transmission electron microscopy (TEM). The TEM images were recorded using a JEM 200CX (Jeol, Japan) microscope operating at 100 kV and equipped with a digital camera. Brightness, contrast and gamma corrections were performed with standard software. The nanoparticles were diluted 100 times and 5 μL of the aqueous solutions were dropped onto a copper TEM grid (300 mesh) coated with carbon film. The TEM images were analyzed using the ImageJ software. The reported particle size and size distribution are the results of the analysis of 150 particles.

2.6 Paclitaxel (PTX) drug loading and loading efficiency

The total amount of the hydrophobic model drug paclitaxel (PTX) loaded into the NPs (total drug feeding subtracted from the free-drug amount collect after the ultrafiltration–centrifugation step described below) was measured by HPLC (Shimadzu, Japan) using a reverse-phase column Chromolith Performance RP-18e (100 × 4.6 mm, eluent water–acetonitrile with acetonitrile gradient 0–100 vol%, flow rate = 1.0 mL min^{-1}).

To start, 100 μL of the drug-loaded NPs was collected from the bulk sample and diluted to 900 μL with acetonitrile. Afterwards, 20 μL of the final sample was injected through a sample loop. PTX was detected at 227 nm using ultraviolet (UV) detection. The retention time of PTX was 11.80 min in such experimental conditions. An analytical curve with linear response in the range (0.5–100 μg mL^{-1}) was obtained and used to determined PTX contents. The free-drug was separated from the drug-loaded NPs by ultrafiltration–centrifugation (Ultrafree-MC 10 000 MW, Millipore) as detailed elsewhere.[38] The samples were centrifuged at 6000 rpm for 30 min. The amount of PTX in the nanoparticles was measured in the filtrate after the dissolution of NPs by using acetonitrile as described earlier. The drug-loading content (LC) and the drug-loading efficiency (LE) were calculated by using the following equations:

$$\text{LC } (\%) = \frac{\text{drug amount in nanoparticles}}{\text{mass of nanoparticles}} \times 100 \quad (3)$$

$$\text{LE } (\%) = \frac{\text{drug amount in nanoparticles}}{\text{drug feeding}} \times 100 \quad (4)$$

2.7 Drug release

The release experiments were carried out at 37 °C by using water as the release media.[39] Aliquots (0.5 mL) of drug-loaded NPs were loaded into 36 Slide-A-Lyzer MINI dialysis microtubes with MWCO 10 kDa (Pierce, Rockford, IL). These microtubes were dialyzed against 3 L of water with gentle stirring. The drug release experiments were performed in triplicate. At each sampling time, three microtubes were removed from the dialysis system and 0.3 mL from each microtube was sampled and diluted to a final volume of 1.0 mL with acetonitrile. The PTX content at each sampling time was then determined *via* HPLC by applying the same procedure previously described. The 0.2 mL remaining in the microtubes was removed and the dimensions of the PTX-loaded NPs were probed by DLS and SLS. The drug diffusion through the membrane was not the rate-limiting step as recently evidenced.[40]

2.8 Biodegradability studies

The biodegradation rate of the PBS/PBDL NPs was followed by SEC. The suspension of nanoparticles (~20 mg of NPs) was loaded in a membrane dialysis bag with MWCO 6–8 kDa (Spectra-Pore®) and then incubated in 0.10 M phosphate buffer solution (PBS) (pH 7.4, 37 °C). At each sampling time, an aliquot of 2 mL of the incubated NPs was removed and their hydrodynamic dimension probed by DLS. The sample was further lyophilized and analyzed by SEC. All the measurements were done in triplicate.

2.9 Cytotoxicity assays

2.9.1. Mouse splenocytes. The mice (C57B/6, H- 2b; Balb/c, H-2d) were killed by cervical dislocation. The spleens were removed aseptically, stripped of fat and placed in an ice-cold RPMI 1640 culture medium (Sigma, USA) supplemented with 4 mM L-glutamine, 50 mM 2-mercaptoethanol, 1 mM sodium pyruvate, 4.5g L^{-1} glucose, antibiotics (penicillin/streptomycin, Sigma, USA), and 10% v/v heat-inactivated fetal calf serum (FCS). Cells were grown in cultivation flasks at 37 °C with 5% CO_2. Single-cell suspensions were obtained by gentle homogenization of mouse spleen in a tissue homogenizer. The spleen lymphocytes were separated from the debris and then washed twice (5 min at 800 g at 4 °C). Red blood cells were lysed with Tris-buffered ammonium chloride solution. Lymphocyte viability was assessed by Trypan Blue exclusion test. The viability of the cells used was >95%. All procedures were approved by the Animal Welfare Committee of the Institute of Microbiology, AS CR, v.v.i.

2.9.2. Proliferation assay of mouse splenocytes. To estimate cell proliferation, [3H]-thymidine incorporation was assessed using a [3H]-thymidine incorporation assay. NUNCLON 96-well, flat-bottomed plates were seeded with 5×10^4 splenocytes/well. Concentrations of 0.01 to 1.00 mg mL^{-1} of the NPs were then added to the wells to a final well volume of 200 μL. The plates were cultured in 5% CO_2 for 48 h at 37 °C. Before the last 6 h of incubation, 18.5 kBq of [3H]-thymidine was added per well. The cells were then collected onto glass fiber filters (Filtermat, Wallac, Finland) using a cell harvester (Tomtec, Orange, CT). After drying, the fibre filter was placed into a sample bag, a solid scintillator (MeltiLex, Wallac) was applied and the bags were sealed (Microsealer, Wallac). Counting was performed in a 1450 MicroBeta Trilux (Wallac). Cells cultivated in fresh medium were used as control. The results were calculated as the arithmetic mean of the c.p.m. in four individual wells. Data represent cell number in relation with the control standard deviation was lower than 15%. The stimulation index (SI) was calculated by the following formula:

$$\mathrm{SI} = \frac{\text{mean cpm in cell cultures}}{\text{mean cpm in control cultures}} \quad (5)$$

3. Results and discussion

3.1 Characterization of the PBS/PBDL copolyester

The synthetic strategies were already fully detailed elsewhere.[28] The structure of the synthesized poly(butylene succinate-*co*-butylene dilinoleate) PBS/PBDL copolyester is portrayed in Fig. 1 and its characteristics are given in Table 1.

The number-average molar mass (M_n) of the copolyester was estimated by SEC as 35×10^3 g mol^{-1} and it holds a reasonable degree of polydispersity ($M_w/M_n = 1.88$). The composition of the copolyester was determined from ^{1}H and ^{13}C NMR (Fig. 1). In ^{1}H NMR the methylene protons of the BD segments appear at 1.69 (*b*, *e*) and 4.1 ppm (*a*, *f*). The signals at 2.61 ppm (*d*) are due to the methylene protons of the SA segment. Methylene protons of the DLA segment adjacent to the ester bond appear as the duplet at 2.27 ppm (*h*) and the protons of the tertiary carbon appear at 1.59 ppm (*i*). The remaining protons at 7.23, 1.24 and 0.87 ppm are related respectively to the hydroxyl groups of the copolyester and to the ethyl and methyl carbon chains of DLA. The ^{13}C NMR spectra signals of BD in the PBS segment appear at 25.3 ppm (*b*) and 64.2 ppm (*a*). These signals are shifted to 25.0 ppm (*e*) and 63.7 ppm (*f*) in the PBDL segment. Additionally, the carbonyl signal of SA in the PBS segment and the carbonyl signal of the DLA segment shifted to 172.3 ppm (*c*) and 173.9 ppm (*g*) respectively, suggesting a complete polycondensation reaction. The molar composition of the copolyester was determined using the relative integrals of SA arising from PBS (*d* or *c*) and the dimerized fatty acid from PBDL (*h* or *g*). The ratio composition was calculated as 3 : 1 (PBS : PBDL) which is close to the feeding monomer ratio (3.6 : 1 for 50/50 wt%). Characteristic signals of the "couplings" in ^{1}H-NMR and ^{13}C-NMR spectra were not found, meaning that the resulting copolymer exhibits a statistical distribution of monomer units. This was confirmed by ^{13}C NMR spectra, which describes the division of the carbonyl groups (C=O) in the copolymer, area ~64 ppm. Both signals of carbonyl groups correspond to the ratio 1 : 3 confirming statistical distribution of monomer units (Fig. S1, ESI†).

The nanoprecipitation protocol requires an organic solvent in which the PBS/PBDL is fully soluble. The solvent must be also miscible in water and it must have a low boiling point to allow further easy evaporation. Among the standard solvents, the best choice was acetone. The distribution of sizes of the dissolved PBS/PBDL copolyester in acetone was assessed by DLS and it is given in Fig. 2.

The size distribution of PBS/PBDL in acetone suggests the presence of diffusing scattering objects having hydrodynamic radius $R_H = 9.5$ nm and it is certainly related to the presence of single dissolved PBS/PBDL copolyester chains in acetone.

3.2 Characterization of the nanoparticles

The nanocarriers were prepared by means of nanoprecipitation. The PBS/PBDL copolymer is insoluble in water and it is expected to undergo precipitation after the diffusion of the solvent (acetone) into the aqueous phase leading to the formation of well-defined nanoparticles. Primarily, the size, size distribution and the stability of the nanoparticles were investigated. It is worth mentioning that all nanoparticles prepared were

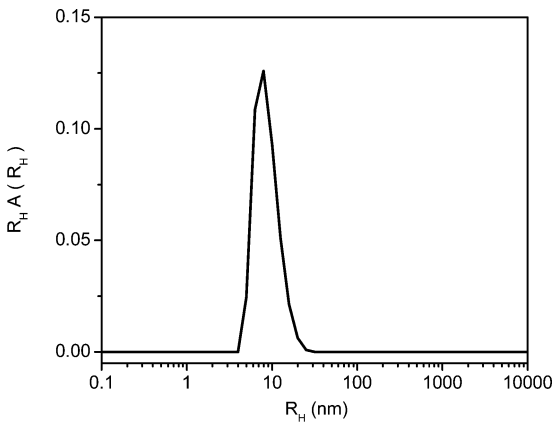

Fig. 2 R_H distribution for PBS/PBDL dissolved in acetone at 5 mg mL^{-1} (40 °C).

Table 1 Characteristics of the synthesized PBS/PBDL copolyester

PBS (wt%)[a]	PBDL (wt%)[b]	DP[a]	$M_n/10^3$ g mol^{-1}[b]	M_w/M_n[b]	T_g/°C	d/g mL^{-1}[c]
50.0	50.0	3	35.0	1.88	−61.0	1.08

[a] Composition and degree of polycondensation estimated by NMR. [b] Measured by SEC. [c] Density measured by flotation in aqueous zinc chloride solution.

macroscopically homogeneous and they showed good macroscopic temporal stability over months. The nanoparticles were probed by dynamic light scattering and the results are given in Fig. 3.

The autocorrelation functions measured at 90° and the respective normalized distributions of relaxation times $\tau A(\tau)$ for different starting polymer concentrations are given in Fig. 3a. The diffusive behavior of the investigated nanoparticles was confirmed by the linear q^2 dependence of the decay rate. Therefore, the Stokes–Einstein equation could be used to determine hydrodynamic radii (R_H) of the assembled objects (Table 2). The existence of a narrow, unimodal particle size distribution with an increase in size as a function of the starting polymer concentration was detected. This tendency is clearly observed by looking at Fig. 3b where the higher the starting polymer concentration the lower is the slope of the linear profiles that quantitatively gives the diffusion coefficient of the NPs, which is finally inversely proportional to their hydrodynamic radius (eqn (1)).

The size of the NPs ranges from 34.5 to 56.7 nm (*i.e.* mean diameters from 69.0 to 113.4 nm). By taking into account that the NPs are produced in a large amount of the nonsolvent water, the increase in nanoparticle size as a function of the polymer concentration might be explained by the nucleation-aggregation

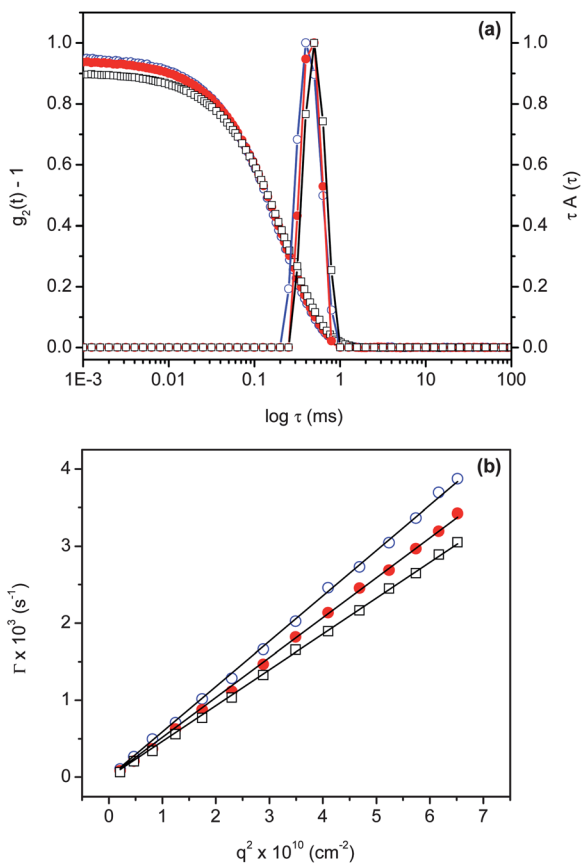

Fig. 3 (a) Autocorrelation functions $g_2(t) - 1$ measured at scattering angle 90° and the respective distributions of the relaxation times $\tau A(\tau)$ revealed by REPES analysis for PBS/PBDL nanoparticles at starting polymer concentrations 2.5 mg mL^{-1} (◯), 5.0 mg mL^{-1} (●) and 10 mg mL^{-1} (□). (b) Angular variation of the frequency $\Gamma = 1/\tau$ as a function of q^2.

mechanism.[41] Therefore, when the solution is sufficiently saturated, critical nuclei of pure solute are formed and they grow by capturing solute molecules from the surroundings. The increase in the number of available copolymer chains (higher concentration) leads to an increase in the number of nuclei and consequently in the probability of nuclei encounters. Each encounter causes aggregation of nuclei thereby increasing the nanoparticle size (and the molar mass of the nanoparticles $M_{w(NP)}$) when nanoprecipitation occurs (Table 2).

The formation of spherical nanoparticles was confirmed by transmission electron microscopy (TEM) and is shown in Fig. 4 (inset). The size distribution histogram resulting from the image analysis is given in the ESI† (Fig. S2). The number-average mean diameter (D_N) and the polydispersity index ($P_{TEM} = D_W/D_N$) were determined as detailed elsewhere[42] and were equal to 72.4 nm and 1.12, respectively ($c_{polymer}$ = 5.0 mg mL^{-1}). This confirms the relatively narrow size distribution of the NPs, although the determined mean size from the TEM image analysis is evidently smaller than the determined by DLS. This is in part due to dehydration of the entities caused by solvent evaporation under the high vacuum conditions employed during TEM imaging. However, discrepancies are also expected because DLS reports an intensity-average dimension whereas TEM reports a number-average dimension. Therefore, TEM images generally undersize relative to DLS data. SAXS measurements were also performed to probe the size, shape and dispersity of the nanoparticles. Fig. 4 shows the SAXS profile of the PBS/PBDL nanoparticles for the polymer concentration 5.0 mg mL^{-1} as the representative example.

In widely separated systems (as in the current case), $I(q)$ is due to the form factor $P(q)$ of the scattering objects. Herein $P(q)$ was modelled geometrically as homogenous spheres:

$$I(q) = V_p^2 \Delta\sigma^2 P(q,R) = \left(\frac{4}{3}\pi R^3 \Delta\sigma\right)^2 \left(\frac{3[\sin(qR) - qR\cos(qR)]}{(qR)^3}\right)^2 \quad (6)$$

The sample polydispersity was considered using the log-normal distribution for which the probability density function is given by:

$$f\ (R,\mu,\delta)\ = \frac{1}{\sqrt{2\pi}\delta R}\exp - \frac{\ln(R/\mu)^2}{2\delta^2} \quad (7)$$

where R is the average radius, μ is the location parameter and δ^2 is the variance. The parameter δ is the standard deviation which gives the quantitative information about the width of the distribution. This fitting approach described the experimental results reasonably well and led to values of $D = 2R = 79.8$ nm and $\delta = 0.144$. It is also worth noting that the high quality of the fitting, particularly at the low-q range of the SAXS profile, hints at the absence of aggregating nanoparticles due their electrostatic stabilization as hereafter discussed. The size of the nanoparticles is within the optimal range for injectable drug release and drug delivery systems where the particle size should be smaller than 200 nm.[43,44] Another requirement for drug delivery nanoparticles which plays an important role in colloidal stability and later in controlled drug release is the narrow size distribution. The nanoparticle distribution width calculated by the cumulant

Table 2 Physico-chemical characteristics of the produced PBS/PBDL nanoparticles

Entry	$c_{polymer}$/mg mL^{-1}	R_H/nm	R_G/nm	R_G/R_H	$M_{w(NP)}/10^8$ g mol^{-1}	d/g mL^{-1}	Dispersity	ζ/mV
NP1	2.5	34.5	40.5	1.17	0.78	0.38	0.067	−36.0
NP2	5.0	46.7	52.6	1.13	1.03	0.39	0.083	−37.0
NP3	10.0	56.7	59.0	1.04	1.74	0.35	0.094	−35.0

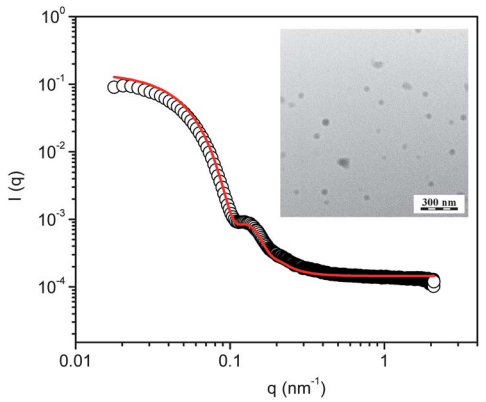

Fig. 4 SAXS data (circles) and corresponding curve fitting (line) for PBS/PBDL nanoparticles produced from starting polymer concentration $c_{polymer}$ = 5.0 mg mL^{-1}. The inset portrays the TEM image in the same conditions.

analysis[45] ranges from 0.067 to 0.094 (Table 2, dispersity). These values are even lower than the values found in similar nanoparticulate systems using surfactants.[29,46,47]

The partial Zimm plot results are reported in Fig. 5 and Table 2. The dn/dc value of the copolyester nanoparticles in water was found to be equal to 0.153 mL g^{-1}. The values of the molar mass of the nanoparticles ($M_{w(NP)}$) and their radius of gyration (R_G) were estimated from the slope of the curves and from the inverse of the intercepts in Fig. 5 (eqn (2)). The concentration of polymeric nanoparticles was preset to 0.1 mg mL^{-1}. The full Zimm plot of NP3 ($c_{polymer}$ = 10.0 mg mL^{-1}) is given in the ESI†

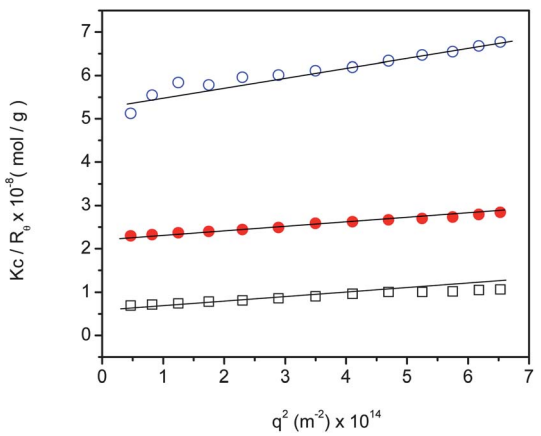

Fig. 5 Static light scattering (Kc/R_θ *vs.* q^2) for PBS/PBDL nanoparticles prepared starting at 2.5 mg mL^{-1} (◯), 5.0 mg mL^{-1} (●) and 10 mg mL^{-1} (□) polymer concentrations. The concentration of polymeric nanoparticles in all the samples was fixed at 0.1 mg mL^{-1}.

(Figure S3). The very similar results allow the use of the partial Zimm plot version.

The $M_{w(NP)}$ increases as a function of the copolymer concentration for the reasons aforementioned. The static and hydrodynamic dimensions of a scattering object are functions of the macromolecular structure and the combination of both provides qualitative information about its architecture. It is well established that the ratio $\rho = R_G/R_H$ is a characteristic parameter related to the conformation of polymer chains and self-assembled macromolecular objects in solution. For hard-spheres, random coils and rod-like structures ρ-values of 0.775, 1.78, and ≥2 have been reported.[48] Furthermore, the ρ-value of spherical objects is dependent on the inner structure and compactness,[49] being close to 0.775 for very compact spheres, $\rho \sim$ 0.8–0.9 for block copolymer micelles due to solvation phenomena[50] and $\rho \sim$ 1.0 for hollow spheres and vesicles. Moreover, R_G/R_H for spherical nanoparticles made from regular branched polymers or statistical randomly polycondensates are found to be within 0.977–1.127.[51–53] These values were found for polymeric nanoparticles following the soft sphere model.[48,51] The R_G/R_H ratios of the PBS/PBDL nanoparticles at different copolymer concentrations (Table 2) are found to be in the same range suggesting that the nanoparticles are not compact. Similar ratios from 1.06 to 1.2 and density lower than 0.01 g mL^{-1} were found for poly(sebacic anhydride)-*co*-polyanhydride nanoparticles prepared by using the nanoprecitation protocol.[54,55] The authors suggested that the results are related to the hyperbranched structure of the nanoparticles and to high amounts of water entrapped inside the assemblies. The average density (d) of the investigated nanoparticles was calculated by using the determined values of $M_{w(NP)}$ and R_H as:[56]

$$d = \frac{3M_{w(NP)}}{4\pi N_A (R_H)^3} \quad (8)$$

wherein N_A is the Avogadro constant. The d-values are independent of the copolymer concentration and at about 0.37 g mL^{-1} (Table 2). The density of the nanoparticles is reasonably low, suggesting that they are porous and probably water-swollen. This is also suggested by the calculated ρ-values characteristic of soft spherical nanoparticles. The soft behavior linked to the water entrapment can explain the remarkable particle stability without the addition of stabilizers (surfactants). The entrapped water inside the particles reduces their density and hydrophobicity and simultaneously increases the particle charge, as is revealed by the ζ-potential measurements (Table 2). The negative ζ-potentials were attributed to the presence of negative charges in the oxygen of the carbonyl group in the ester bounds and to the remaining carboxyl terminal groups in the multiblock copolymer nanoparticles.[48,57] The entrapped water should increase electron

delocalization in the oxygen of the carbonyl group in the ester bounds and increase the particle charge and consequently their stability.

3.3 Drug-loading and loading efficiency

The loading content (LC) is the drug-loading capacity of a nanocarrier and it is related to its mass (eqn (3)) whereas LE is the drug-loading efficiency and it is related to the total drug feeding (eqn (4)). Ideally, a successful nanoparticulate system should have a high drug-loading capacity thereby reducing the quantity of matrix material for administration and a high loading-efficiency to avoid drug losses and therapy commitment. Drug loading and entrapment efficiency are strongly dependent on the solid-state drug solubility in the polymer matrix[29,58] which is dependent on the polymer composition, molar mass, polymer–drug interactions and the presence of terminal functional groups (ester or carboxyl).[59] To investigate the LC and LE of the PBS/PBDL nanocarriers, PTX was used as the hydrophobic drug model and loaded to the novel copolyester NPs. The drug-loaded NPs were prepared using essentially the same procedure previously described except that in such a case a known amount of PTX was dissolved in acetone along with the PBS/PBDL copolyester. The LC of the PBS/PBDL NPs was investigated in the range 1–10% $w_{drug}/w_{polymer}$. It has been found that the stability of the drug-loaded PBS/PBDL NPs was limited to ~6–7% $w_{drug}/w_{polymer}$ drug feeding. For comparison, two well-known FDA-approved polyesters (PLGA and PLA) were also used to prepare PTX-loading NPs. PBS/PBDL, PLGA and PLA PTX-loaded NPs were prepared at 2.5% $w_{drug}/w_{polymer}$ drug feeding. In such conditions, the LC of the PBS/PBDL NPs was ~2.5% $w_{drug}/w_{polymer}$ and LE ~100%. On the other hand, the PXT LC was ~0.90% $w_{drug}/w_{polymer}$ and LE ~89% for PLGA NPs and for PLA NPs the LC and LE were significantly lower ~0.73% and ~70% respectively. These results show that the novel synthesized polyester exhibits higher entrapment efficiency and drug loading capacity compared to PLA or PLGA suggesting stronger hydrophobic interactions between the PBS/PBDL copolyester matrix and the PTX drug. Accordingly, PBS/PBDL copolyester nanoparticles seem to be a promising alternative to hydrophobic drug encapsulation in biomedical and drug delivery applications.

3.4 Drug release experiments

Generally, the drug release is governed by two different mechanisms: *i*) a standard diffusion-controlled release or *ii*) a triggered pathway initiated by changing the environmental conditions such as pH or temperature. Additionally, considering nanoparticles produced from biodegradable polymers, the drug release is also supposed to be controlled by the bulk erosion rate.[39] It is well-known that the drug diffusion-controlled release depends on its effective diffusion coefficient throughout the polymer matrix, which in turn depends on its porosity and tortuosity.[29,58] As mentioned above, the stability of the drug-loaded PBS/PBDL NPs is limited to ~6–7% $w_{drug}/w_{polymer}$ drug feeding. Accordingly, the release experiments were carried out by setting the loading content at LC = 5.0% $w_{drug}/w_{polymer}$. The LE was reasonably reproducible and nearly constant at ~95% and the drug release was monitored by HPLC and light scattering (DLS and SLS). The results are shown in Fig. 6.

The release experiments indicate that approximately 40% of the encapsulated PTX is released within the first 12 h whilst only 10% is sustained in the polymeric core after 120 h (Fig. 6a). The slow pharmacokinetic release might be attributed to the hydrophobicity of the manufactured PBS/PBDL nanocarriers and to the poor water solubility (~0.3 μg mL^{-1}) of the entrapped drug. In the current case, certainly the drug release is controlled by the

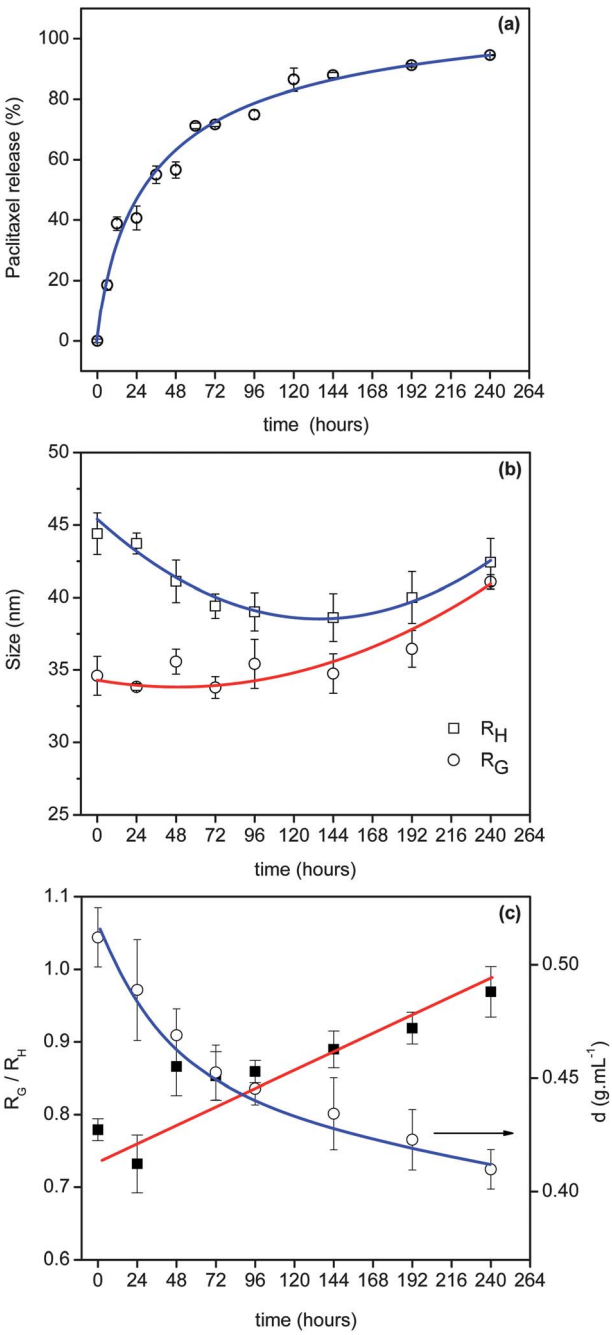

Fig. 6 Drug release profile from PTX-loaded PBS/PBDL NPs prepared using $c_{polymer}$ = 5.0 mg mL^{-1} (a). R_G and R_H (b) and R_G/R_H and nanoparticle density (c) *vs.* time during PTX release.

diffusion of the drug through the polymer matrix and by the hydrolysis of the PBS/PBDL copolymer.

As previously mentioned, the combination of SLS and DLS measurements is appropriate to measure hydrodynamic dimensions of nanoparticles and it might also provide informations on the shape and inner structure of the scattering objects. Furthermore, quantitative information on the density of the nanoparticles and draining properties might be further probed.[48] The drug encapsulation and release was also followed by DLS and SLS measurements and the data in Fig. 6b clearly indicate that the drug encapsulation reduces the dimensions of the nanocarriers. By comparing with the dimensions of the drug-free NPs (Table 2, $c_{polymer} = 5.0$ mg mL^{-1}), the hydrodynamic dimension (R_H) was reduced from 46.7 (drug-free) to 44.0 nm (drug-loaded at $t = 0$ h) whereas their radius of gyration (R_G) has been reduced from 52.6 (drug-free) to 35.0 nm (drug-loaded at $t = 0$ h).

The reduction in R_G is more pronounced than the reduction in R_H and it consequently reflects the reduction on the ρ-value from 1.13 (drug-free) to 0.79 (drug-loaded at $t = 0$ h). Simultaneously, the density of the particles increases from 0.39 g mL^{-1} to 0.51 g mL^{-1}. These experimental data certainly reflect the softness of the NPs[60] and the transition of the inner structure from a water-swollen condition (drug-free NPs) towards a higher degree of compactness (drug-loaded NPs). The PTX encapsulation led to a higher degree of compactness once the ρ-value was displaced towards the hard-sphere character. Indeed, the stability of the drug-free PBS/PBDL nanoparticles in pure water suggests that they are partially drained or that the polymer chains forming the NPs are not fully collapsed. The values of their density (~0.37 g mL^{-1}) are much lower than the density of the bulk copolymer (1.08 g mL^{-1}) pointing out that the polymer chains forming the NPs are loosely packed and therefore, they must certainly be swollen by water. The PBS/PBDL copolyester comprises a less hydrophobic segment (PBS) containing numerous ester bonds. Accordingly, it is reasonable to accept the water-swollen characteristic of the NPs in the drug-free conditions. As matter of fact, PLA nanoparticles (which are hydrophobic) are generally highly swollen by water ($d \sim 0.15$ g mL^{-1}), which confers them considerable stability.[61]

The swelling–collapse transition of the polymeric nanoparticles caused by the hydrophobic drug loading is unmistakably supported by the SAXS data (Fig. 7). The SAXS data of the unloaded and PTX-loaded NPs were fitted with the form factor of homogeneous spheres. The electron density of PBS/PBDL was calculated by using the average chemical composition of the copolyester and its density as being equal to 0.353 e$^-$ Å^{-3}. The electron density of water (0.334 e$^-$ Å^{-3}) is incidentally close to the one calculated for the copolyester. Consequently, contrast changes are hardly seen in the swelling–collapse evolution. Nevertheless, the reduction in the dimension of the NPs caused by drug-loading is clearly evidenced by the displacement of the bump at $q \sim 0.15$ nm^{-1} towards the high-q range. The average radius (R) of the NPs is reduced from 39.9 to 35.2 nm by the addition of 5.0% $w_{drug}/w_{polymer}$ of the hydrophobic guest molecule. It suggests that PTX is entrapped inside the copolyester matrix during the drug encapsulation resulting in the shrinking of the nanoparticles caused by water draining. The less hydrophobic segment of the copolyester (PBS) is supposed to be responsible for a thick stabilizing layer and the NPs packing is

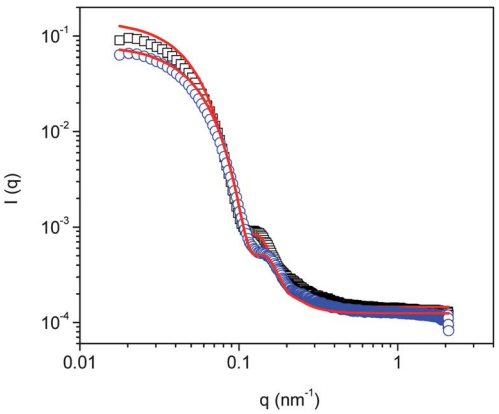

Fig. 7 SAXS data (circles) and corresponding curve fitting (line) for unloaded (□) and 5.0% $w_{drug}/w_{polymer}$ PTX-loaded (◯) PBS/PBDL nanoparticles produced from starting polymer concentration $c_{polymer} = 5.0$ mg mL^{-1}.

mostly due to the strong hydrophobic interactions expected between the model drug and the highly hydrophobic PBDL segment.

The speculated swelling–collapse transition is schematically represented in Fig. 8.

The drug release is accompanied by a continuous increase of R_G/R_H simultaneous to a continuous reduction in the density of the nanoparticles (Fig. 6c). The R_G of the nanoparticles remained nearly constant whereas R_H reduces within the first 96 h followed by a slightly increase after 144 h, suggesting diffusion release of the entrapped drug. The initial R_H reduction should be related to the PTX diffusion from the PBS/PBDL NPs core towards their surface. This drug-diffusion evolution is linked to simultaneous changes in the inner structure of the NPs. The amount of water remaining in the outer shell of the nanoparticles might be drained out due to the PTX diffusion from the core towards the aqueous media. This leads to an increase in the hydrophobicity along the nanoparticles and to the shrinking of the copolyester matrix as experimentally evidenced by the reduction of the hydrodynamic dimension of the NPs within the first 96 h when PTX diffusion and water draining towards the aqueous media is faster than water draining towards the core. At the end of the PTX release (240 h, 100% PTX released) the R_G increases, approaching the initial value (Fig. 6b) and the density of the particles decreases to

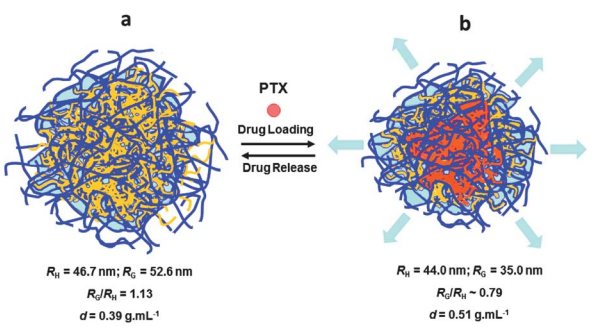

Fig. 8 Schematic representation of the PTX-loading effect. Unloaded (a) and PTX-loaded PBS/PBDL NPs (b). The PTX drug is represented as filled circles and the islands of water are represented in blue.

0.41 g mL^{-1} (Fig. 6c). The experimental results clearly suggest that when the hydrophobic PTX is totally released, the nanoparticles acquire the initial soft characteristic once the inner core is again water-swollen due to the reduction in its hydrophobicity caused by the drug release. These results point out that the PTX release from PBS/PBDL NPs is mainly governed by drug diffusion and water draining through the polymer matrix. To the best of our knowledge, the combined DLS and SLS measurements used to study structural changes of polymeric nanoparticles induced by the hydrophobic drug encapsulation and drug release have no precedent in the literature. Therefore, these preliminary results demonstrate the feasibility of combined DLS and SLS as a powerful tool to investigate the correlations between the drug release profile and the structure of soft and porous polymeric nanocarriers.

3.5 Degradation behavior of the novel copolyester nanoparticles

The potential biomedical application of hydrophobic biodegradable polymers requires the knowledge of their biodegradation rates. Although PLA, PCL and PLGA are FDA-approved biocompatible and biodegradable polymers, their slow degradation rates limits the polymer concentration threshold for injectable drug release systems. Water-insoluble biodegradable polymers can be degraded by bulk erosion, surface erosion or both simultaneously.[39] The degradation mechanism depends on the diffusivity of water inside the polymeric matrix, susceptibility to hydrolysis of the functional groups, and the matrix dimensions. Considering polymeric nanoparticles, as in the current case, water diffusion within the nanoparticles should be faster than bond hydrolysis and therefore, the prevailing eroding mechanism will probably involve bulk degradation.[62]

The biodegradation rate of the PBS/PBDL copolyester was followed by SEC (by monitoring its molar mass over time) as shown in Fig. 9.

The PBS/PBDL copolyester has an initial weight-average molar mass $M_w = 66 \times 10^3$ g mol^{-1} and as expected, it continuously decreases as a function of time. A pronounced reduction in M_w can be observed in the second week whereas only slight changes were observed in the hydrodynamic dimension of the polymeric nanoparticles. At the end of the second week, precipitates could be observed by the naked eye in the dialysis bag and at the end of the third week, the nanoparticles collapsed and only large ill-defined aggregates were detected by light scattering. In Fig. 9c one can observe that as the degradation progresses, the SEC peak curves shifts towards longer elution time. The initial main peak is essentially decomposed into two smaller peaks indicating the formation of lower molecular weight macromolecules and broadening molar mass distribution due to hydrolytic cleavage of ester bonds. This degradation behavior is strictly connected to the structure of the nanoparticles. As previously mentioned, the PBS/PBDL NPs have a soft characteristic and density equal to 0.37 g mL^{-1} meaning that they contain a substantial amount of water inside which probably accelerate the hydrolysis process. This is supported by the fast copolyester degradation after two weeks although without a clear reduction in the hydrodynamic dimension of the biodegradable nanoparticles.

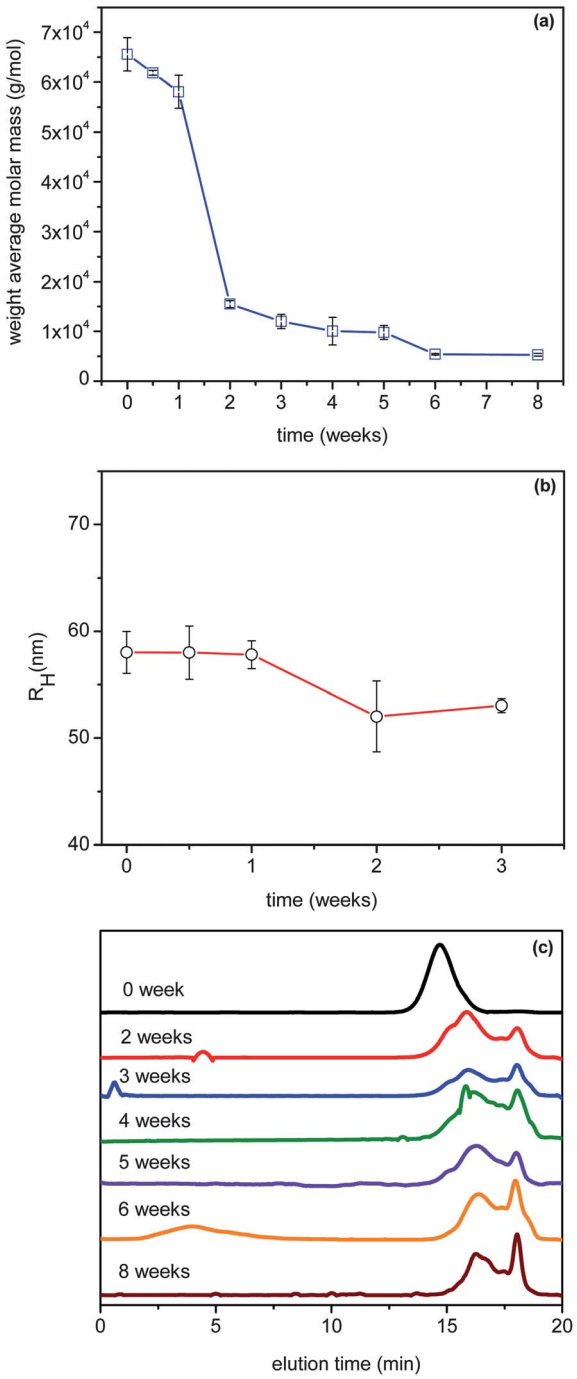

Fig. 9 Weight-average molar mass (M_w) of polymers fragments (a) and hydrodynamic radius (R_H) of the nanoparticles (b) as a function of time during incubation in PBS (pH 7.4). Respective SEC profiles (c).

3.6 Cytotoxicity

The *in vitro* cell proliferation was determined by [3H]-thymidine incorporation into mice C57B/6 and Balb/c unstimulated (spontaneously proliferating) splenocytes incubated with PBS/PBDL NPs, and was used to evaluate the toxicity of the NPs. The results (Fig. 10) show a significant increase in cell proliferation for NPs incubated with both types of mice splenocytes cells in all concentrations evaluated.

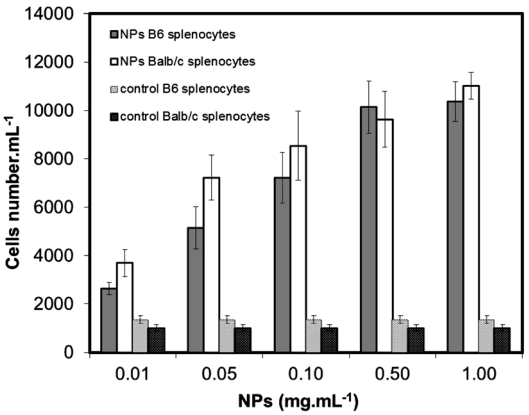

Fig. 10 *In vitro* effect of PBS/PBDL NPs (mg mL^{-1}) on mice Balb/c and B6 splenocytes cell proliferation.

Similar increases in cell proliferation with an increase in the concentration of NPs were also observed on surfactant-containing systems at low surfactant concentrations.[63] Surfactant concentrations higher than 0.1–0.5 mg mL^{-1} disrupt the physiological membranes and become highly toxic to cells. For the current case, surprisingly, the enhanced cell proliferation was observed also at higher NPs concentration. These imply that the investigated PBS/PBDL NPs should be non-toxic in contact with the living systems. This fulfils the basic requirement of good biocompatibility, which is a prerequisite for the biomedical applications.

4. Conclusion

Novel biocompatible and biodegradable PBS/PBDL nanoparticles were produced from aliphatic based monomers consisting of succinic acid, butanediol and dilinoleic acid and their potential applicability in the biomedical field was evaluated. The NPs were prepared by dissolving the PBS/PBDL copolyester in acetone followed by the single-step nanoprecipitation protocol in pure water. TEM and SAXS measurements indicated the spherical shape of the PBS/PBDL NPs. The DLS measurements confirmed the formation of narrowly distributed nanosized particles (R_H < 60 nm) suggesting optimized conditions for drug delivery systems. The structure sensitive parameter of the nanoparticles ($\rho = R_G/R_H$) and their density determined by combined DLS and SLS measurements suggested that they are soft and probably composed of a water-swollen core that confers a non-compact character. The water entrapped in the NPs seems to play a crucial role in the particle's stability and in their relatively fast degradation. The polymeric nanoparticles could be loaded with the poorly water-soluble anti-cancer drug paclitaxel (PTX) with encapsulation efficiency ~95% and drug loading content ~6–7% $w_{drug}/w_{polymer}$. The drug encapsulation and release was followed by HPLC and light scattering measurements (DLS and SLS). The drug encapsulation and release were found to modify the inner structure of the nanoparticles and the mechanism is controlled by both water draining and drug diffusion through the polymer matrix. The drug encapsulation leads to shrinking and to a higher degree of compactness of the NPs due to hydrophobic interactions between the polymeric core and the anticancer drug. The system returns to its initial character as the drug release proceeds. The cell viability experiments demonstrated that the nanoparticles are biocompatible and non-toxic, making them potentially useful for applications in nanomedicine.

Acknowledgements

This work has been sponsored by the Grant Agency of the Czech Republic (Grants IAAX00500803 and P208/10/1600). F. C. G acknowledges financial support from FAPESP (Grant 2010/06348-0). A. Kozlowska and M. El Fray acknowledge financial support from the Polish Ministry of Science and Higher Education (Project N° N209 216538). The authors are grateful to SOLEIL (proposal SWING 20110302) for provision of SAXS beamtime and to S. Meneau and M. Šlouf for assistance during SAXS and TEM measurements respectively. Dr Zdeněk Tuzar is acknowledged for helpful discussions.

References

1 M. E. Davis, J. E. Zuckerman, C. H. J. Choi, D. Seligson, A. Tolcher, C. A. Alabi, Y. Yen, J. D. Heidel and A. Ribas, *Nature*, 2010, **464**, 1067–1071.
2 D. Peer, J. M. Karp, S. Hong, O. C. Farokhzad, R. Margalit and R. Langer, *Nat. Nanotechnol.*, 2007, **2**, 751–760.
3 L. Y. T. Chou, K. Ming and W. C. W. Chan, *Chem. Soc. Rev.*, 2011, **40**, 233–245.
4 C.-A. J. Lin, R. A. Sperling, J. K. Li, T.-Y. Yang, P.-Y. Li, M. Zanella, W. H. Chang and W. J. Parak, *Small*, 2008, **4**, 334–341.
5 L. E. Euliss, J. A. DuPont, S. Gratton and J. DeSimone, *Chem. Soc. Rev.*, 2006, **35**, 1095–1104.
6 A. Kumari, S. K. Yadav and S. C. Yadav, *Colloids Surf., B*, 2010, **75**, 1–18.
7 M. Goldberg, R. Langer and X. Q. Jia, *J. Biomater. Sci., Polym. Ed.*, 2007, **18**, 241–268.
8 C. S. Ha and J. A. Gardella Jr., *Chem. Rev.*, 2005, **105**, 4205–4232.
9 S. Schubert, J. T. Delaney Jr. and U. S. Schubert, *Soft Matter*, 2011, **7**, 1581–1588.
10 M. J. Campolongo and D. Luo, *Nat. Mater.*, 2009, **8**, 447–449.
11 J. Panyam and V. Labhasetwar, *Adv. Drug Delivery Rev.*, 2003, **55**, 329–347.
12 J. M. Anderson and M. S. Shive, *Adv. Drug Delivery Rev.*, 1997, **28**, 5–24.
13 H. Li, J. Chang, A. Cao and J. Wang, *Macromol. Biosci.*, 2005, **5**, 433–440.
14 J. Yang, W. Tian, Q. Li, Y. Li and A. Cao, *Biomacromolecules*, 2004, **5**, 2258–2268.
15 I. Bechthold, K. Bretz, S. Kabasci, R. Kopitzky and A. Springer, *Chem. Eng. Technol.*, 2008, **31**, 647–654.
16 R. van Dijkhuizen-Radersma, J. R. Roosma, P. Kaim, S. Metairie, F. L. A. M. A. Péters, J. de Wijn, P. G. Zijlstra, K. de Groot and J. M. Bezemer, *J. Biomed. Mater. Res.*, 2003, **67A**, 1294–1304.
17 R. van Dijkhuizen-Radersma, J. R. Roosma, J. Sohier, F. L. A. M. A. Péters, M. van den Doel, C. A. van Blitterswijk, K. de Groot and J. M. Bezemer, *J. Biomed. Mater. Res.*, 2004, **71A**, 118–127.
18 L. Wang, J. Chen, H. Liu, Z. Chen, Y. Zhang, C. Wang and Z. Feng, *Polym. Int.*, 2004, **53**, 2145–2154.
19 A. Lindström, A. C. Albertsson and M. Hakkarainen, *Polym. Degrad. Stab.*, 2004, **83**, 487–493.
20 J. Bremer and H. Osmundensen, *Fatty acid oxidation and regulation*, Amsterdam, Elsevier, 1984.
21 J. P. Jain, M. Sokolsky, N. Kumar and A. J. Domb, *Polym. Rev.*, 2008, **48**, 156–191.
22 A. J. Domb and M. Maniar, *J. Polym. Sci., Part A: Polym. Chem.*, 1993, **31**, 1275–1285.
23 P. Prowans, M. El Fray and J. Slonecki, *Biomaterials*, 2002, **23**, 2973–2978.

24 M. Renke-Gluszko and M. El Fray, *Biomaterials*, 2004, **25**, 5191–5198.
25 M. El Fray, M. Feldmann, G. Ziegler and P. Prowans, *J. Mater. Sci.: Mater. Med.*, 2007, **18**, 501–506.
26 M. El Fray, *Adv. Eng. Mater.*, 2009, **11**, B35–40.
27 M. El Fray, A. Piegat and P. Prowans, *Adv. Eng. Mater.*, 2009, **11**, B200–203.
28 A. Kozlowska, D. Gromadzki, M. El Fray and P. Štěpánek, *Fib. Text. East Eur.*, 2008, **71**, 85–88.
29 E. Jäger, C. G. Venturini, F. S. Poletto, L. M. Colomé, J. P. U. Pohlmann, A. Bernardi, A. M. O. Battastini, S. S. Guterres and A. R. Pohlmann, *J. Biomed. Nanotechnol.*, 2009, **5**, 130–63.
30 S. Hornig, T. Heinze, R. Becer and U. S. Schubert, *J. Mater. Chem.*, 2009, **19**, 3838–3840.
31 I. Y. Perevyazko, J. T. Delaney Jr, A. Vollrath, G. M. Pavlov, S. Schubert and U. S. Schubert, *Soft Matter*, 2011, **7**, 5030–5035.
32 S. A. Galindo-Rodríguez, P. François, S. Briançon, E. Allémann, E. Doelker and H. Fessi, *Eur. J. Pharm. Sci.*, 2005, **25**, 357–367.
33 M. Netopilík, F. Schallausky, S. Reichelt, A. Lederer and P. Kratochvíl, *Int. J. Polym. Anal. Charact.*, 2007, **12**, 285–284.
34 P. Štěpánek, *J. Chem. Phys.*, 1993, **99**, 6384–6393.
35 J. Jakes, *Czech. J. Phys.*, 1988, **38**, 1305.
36 P. Štěpánek and Č. Koňák, *Polymer*, 1984, **21**, 195–274.
37 J. Kohlbrecher, Software Package SASfit for Fitting Small-Angle Scattering Curves, http://kur.web.psi.ch/sans1/SANSSoft/sasfit.html, 2010.
38 E. Penott-Chang, A. Walther, P. Millard, A. Jäger, E. Jäger, A. H. E. Müller, S. S. Guterres and A. R. Pohlmann, *J. Biomed. Nanotech.*.
39 J. M. Chan, L. Zhang, K. P. Yuet, G. Liao, J.-W. Rhee, R. Langer and O. C. Farokhzad, *Biomaterials*, 2009, **30**, 1627–1634.
40 F. C. Giacomelli, P. Štěpánek, C. Giacomelli, V. Schmidt, E. Jäger, A. Jäger and K. Ulbrich, *Soft Matter*, 2011, **7**, 9316–9325.
41 J. Aubry, F. Ganachaud, J.-P. C. Addad and B. Cabane, *Langmuir*, 2009, **25**, 1970–1979.
42 J. Rieger, H. Freichels, A. Imberty, J.-L. Putaux, T. Delair, C. Jérôme and R. Auzély-Velty, *Biomacromolecules*, 2009, **10**, 651–657.
43 V. Mailander and K. Landfester, *Biomacromolecules*, 2009, **10**, 2379–2400.
44 J. M. Chan, L. Zhang, R. Tong, G. Ghosh, W. Gao, G. Liao, K. P. Yuet, D. Gray, J. Rhee, J. Cheng, G. Golomb, P. Libby, R. Langer and O. C. Farokhzad, *Proc. Natl. Acad. Sci. U. S. A.*, 2010, **107**, 2213–2218.
45 P. Stepánek, in *Dynamic light scattering: The Method and Some Applications*, ed. W. Brown, Oxford Science Publications, Oxford, 1993.
46 A. Besheer, J. Vogel, D. Glanz, J. Kressler, T. Groth and K. Mäder, *Mol. Pharmaceutics*, 2009, **6**, 407–415.
47 A. Jäger, V. Stefani, S. S. Guterres and A. R. Pohlmann, *Int. J. Pharm.*, 2007, **338**, 297–305.
48 M. Seldák and Č. Koňák, *Macromolecules*, 2009, **42**, 7430–7438.
49 M. Li, M. Jiang, L. Zhu and C. Wu, *Macromolecules*, 1997, **30**, 2201–2203.
50 F. C. Giacomelli, I. C. Riegel, C. L. Petzhold, N. P. Silveira and P. Stepánek, *Langmuir*, 2009, **25**, 731–738.
51 W. Burchard, K. Kajiwara and D. Nerger, *J. Polym. Sci., Polym. Phys. Ed.*, 1982, **20**, 157–171.
52 K. Kajiwara, *Polymer*, 1971, **12**, 57–66.
53 W. Burchard, in *Light Scattering from Polymers*, ed. W. Burchard, G. D. Patterson, *Advances in Polymer Science*, 48, Springer-Verlag, New York, 1983; pp. 66–78.
54 J. Fu and C. Wu, *J. Polym. Sci., Part B: Polym. Phys.*, 2001, **39**, 703–708.
55 J. Fu, X. Li, D. K. P. Ng and C. Wu, *Langmuir*, 2002, **18**, 3843–3847.
56 Č. Koňák, V. Šubr, L. Kostka, S. Štěpánek, K. Ulbrich and H. Schlaad, *Langmuir*, 2008, **24**, 7092–7098.
57 F. Quaglia, L. Ostacolo, G. De Rosa, M. I. La Rotonda, M. Ammendola, G. Nese, G. Maglio, R. Palumbo and C. Vauthier, *Int. J. Pharm.*, 2006, **324**, 56–66.
58 L. A. Fiel, L. M. Rebêlo, T. M. Santiago, M. D. Adorne, S. S. Guterres, J. S. Sousa and A. R. Pohlmann, *Soft Matter*, 2011, **7**, 7240–7247.
59 J. Panyam, D. Williams, A. Dash, D. Leslie-Pelecky and V. Labhasetwar, *J. Pharm. Sci.*, 2004, **93**, 1804–1814.
60 Y. Tu, X. Wan, D. Zhang, Q. Zhou and C. Wu, *J. Am. Chem. Soc.*, 2000, **122**, 10201–10205.
61 Y. Zhao, J. Fu, D. K. P. Ng and C. Wu, *Macromol. Biosci.*, 2004, **4**, 901–906.
62 F. von Burkersroda, L. Schedl and A. Göopferich, *Biomaterials*, 2002, **23**, 4221–4231.
63 G. Wei, Y. Li, G. Du and J. Chen, *Process Biochem.*, 2003, **38**, 1133–1138.

Shrinkage/Swelling of Polymeric Nanoparticles Induced by Hydrophobic Drug Entrapment

Alessandro Jäger,[a]* *Eliézer Jäger,*[a]* *Fernando Carlos Giacomelli,*[b] *Frédéric Nallet,*[c] *Miloš Steinhart,*[a] *Jean-Luc Putaux,*[d,e] *Karel Ulbrich*[a] *and Petr Štěpánek*[a]

[a] Institute of Macromolecular Chemistry, Heyrovsky Sq. 2, 162 06 Prague 6, Czech Republic;

[b] Centro de Ciências Naturais e Humanas, Universidade Federal do ABC, 09210-170 Santo André, Brazil;

[c] Centre de Recherche Paul-Pascal, CNRS, Université de Bordeaux, 115 Avenue Schweitzer, 33600 Pessac, France.

[d] Université Grenoble Alpes, Centre de Recherches sur les Macromolécules Végétales (CERMAV), F-38000 Grenoble, France

[e] CNRS, CERMAV, F-38000 Grenoble, France

* Corresponding Author: Alessandro Jäger, email: jager@imc.cas.cz

Eliézer Jäger, email: jagereliezer@gmail.com

Abstract

The potential use of polyester polymeric nanoparticles (NPs) as drug nanocarriers is well-documented. Nevertheless, structural changes due to hydrophobic drug loading and release have been rarely explored. Herein, we have used static and dynamic light scattering (SDLS), small-angle X-ray scattering (SAXS), transmission electron microscopy (TEM) and cryo-TEM to probe how the entrapment of a hydrophobic guest molecule (drug) changes the nanoparticle´s feature. The presence of the hydrophobic guest molecule modifies the inner structure of the NPs. The polymeric assemblies are characterized by differences in their densities (~ 0.06 g/cm^3 for PLA or PLGA and 0.39 g/cm^3 for PBSBDL). They are thus water swollen in the guest-free condition. The NPs were further prepared by using the same polyesters and given amounts of the highly hydrophobic guest drug paclitaxel (PTX). The density (d_{NP}), R_G (radius of gyration), R_H (hydrodynamic radius), R_G/R_H and R (contrast radius) have been monitored as a function of the amount of drug loaded. The drug entrapment increased the size of PLA and PLGA NPs. On the other hand, it also promoted the shrinkage of PBSBDL NPs. These observations revealed that changes in the inner structure of soft nanoparticles caused by drug loading is not straightforward and it mainly depends on the strength of wan der Walls interactions between the polyester core and the probe which is connected to their chemical composition and hydrophobicity.

Introduction

Polymer chemistry has reached the necessary sophistication to allow the production of macromolecules with accurate control over their structure, composition, and properties. Thanks to the advances in polymer chemistry and polymer colloids, polyester nanoparticles (NPs) have emerged into the biotechnology field and are rapidly heading to the forefront of drug delivery systems, diagnostics and other areas.[1,2] Nowadays, the development of biocompatible polyester-based nanocarriers and their detailed inner characterization is a challenge endeavor in the field of nanotechnology. A substantial volume of literature has been dedicated to the investigation of the effects of particle preparation process on particle properties. It was demonstrated that solvents, emulsifiers and particle composition affect particle size and cargo release. Particular interest is devoted to their biocompatibility and bioabsorbability which has already shown to be very useful in numerous biomedical applications. Moreover, these characteristics can be easily tailored to modify the release, degradation and loading capacity.[3,4]

Recently, the appropriate combination of static and dynamic light scattering (SDLS) has been employed to probe the radius of gyration (R_G) and the hydrodynamic dimension (R_H) of NPs.[5] These techniques can later provide information on the shape and inner structure of scattering objects.[5] Quantitative information on the density of the NPs and draining properties might be also accessed.[6] It is well established that the ratio $\rho = R_G/R_H$ is a characteristic parameter related to the conformation of polymer chains and self-assembled macromolecular objects in solution. For hard-spheres, random coils and rod-like structures ρ-values of 0.775, 1.78, and $\geq$ 2 have been reported. Furthermore, the ρ-value of spherical objects is dependent on the inner structure and

compactness[7] being close to 0.775 for compact spheres, $\rho \sim$ 0.8-0.9 for block copolymer micelles due to solvation phenomena[8] and $\rho \sim$ 1.0 for hollow spheres and vesicles. Additionally, the R_G/R_H ratio of spherical NPs of regular branched polymers or statistical randomly polycondensates are found to be within the range 0.977-1.127.[9,10,11] These values are related to the high amounts of water entrapped inside the assemblies which is reported as the soft sphere model.[12,13]

In this report, scattering and imaging techniques have been used to probe the structural changes of polymeric nanocarriers due to hydrophobic drug loading and release. The NPs were prepared by using various polyesters and different amounts of the highly hydrophobic drug paclitaxel (PTX). The NPs density (d_{NP}), R_H (DLS), R_G (SLS), R_G/R_H and R (SAXS) have been monitored as a function of the amount of loaded PTX. It is worth mentioning that scattering techniques are powerful tools to probe the inner structure of nanostructured systems. The entrapment of the hydrophobic guest molecule changes the polymeric nanoparticle's matrix leading to the swelling or to the collapse of the entities. These observations are being discussed throughout the manuscript based on polymer architecture, chemical composition, as well as hydrophobicity.

Experimental

The synthesis of the aliphatic copolyester PBSBDL was performed following the two-steps melt polycondensation (esterification and polycondensation) as previously described and detailed in Supplementary Information.[14] The NPs were prepared using the nanoprecipitation protocol where a preheated (40 °C) acetone solution (5 mL) containing the PBSBDL copolyester (50 mg) and PTX (preset amounts) were added drop-wise (2.5 mL.min^{-1}, KDS Gemini 88 pumps system; KD Scientific, Holliston, MA, USA) into preheated (40 °C) Milli-Q® water media followed by acetone evaporation.

The same procedure has been employed to prepare the PLA and PLGA NPs. They were further characterized by scattering analysis and imaging. The static and dynamic light scattering data were acquired by using an ALV CGE laser goniometer. SAXS experiments were conducted at the ID02 SAXS beamline of the European Synchrotron Radiation Facility (Grenoble, France). Negatively stained dry preparations and quench-frozen thin films of NP suspensions were observed using a Philips CM200 'Cryo' microscope operating at 80 kV. Images were recorded on Kodak SO163 films. Technical details of the whole set of characterization techniques are given in Supplementary Information File.

Results and Discussions

Representative raw static light scattering data are reported in Figure 1 (A) for PBSBDL poly[(butylene succinate)-*co*-(butylene dilinoleate)] in guest-free (open circles) and 5% *wt* guest-loaded (filled circles) conditions.

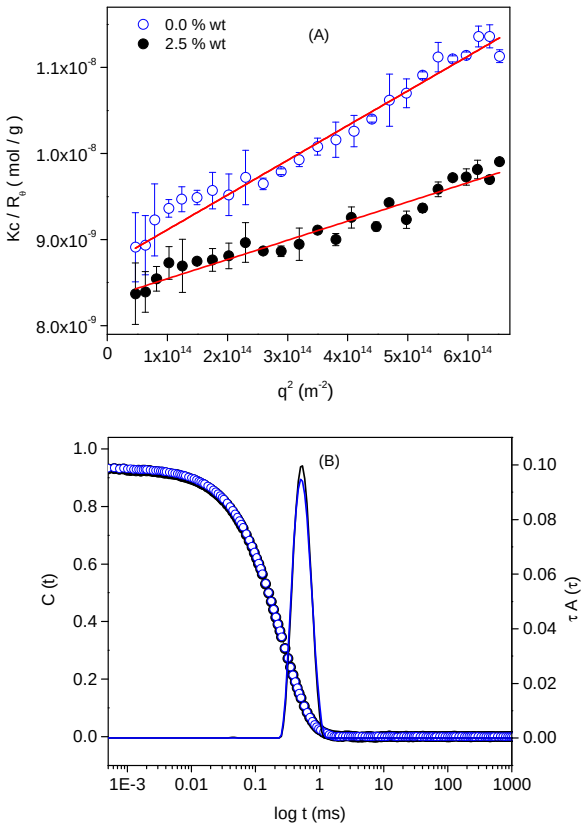

Figure 1. Static light scattering (Kc/R_θ *vs.* q^2) (A) and autocorrelation functions along to the respective distributions of relaxation times (B) for guest-free (○) and guest-loaded (●) PBSBDL NPs.

The d*n*/d*c* value of PBSBDL in water was determined to be 0.153 mL.g^{-1}.[15] The concentration of NPs was preset to 0.5 mg.mL^{-1}. The values of the molecular weight of the nanoparticles ($M_{w(NPs)}$) and their radius of gyration (R_G) were estimated from the inverse of the intercepts and from the slope of the curves respectively (Table 1). Simultaneously, the hydrodynamic dimension has been determined *via* dynamic light scattering. The representative autocorrelation functions along to the respective distributions of relaxation times are also given in Figure 1 (B). The hydrodynamic dimension (R_H) was determined by using the well-known Stokes-Einstein equation.

The determined values of R_G and R_H of PBSBDL NPs as a function of the amount of the loaded PTX are given in Figure 2 (A).

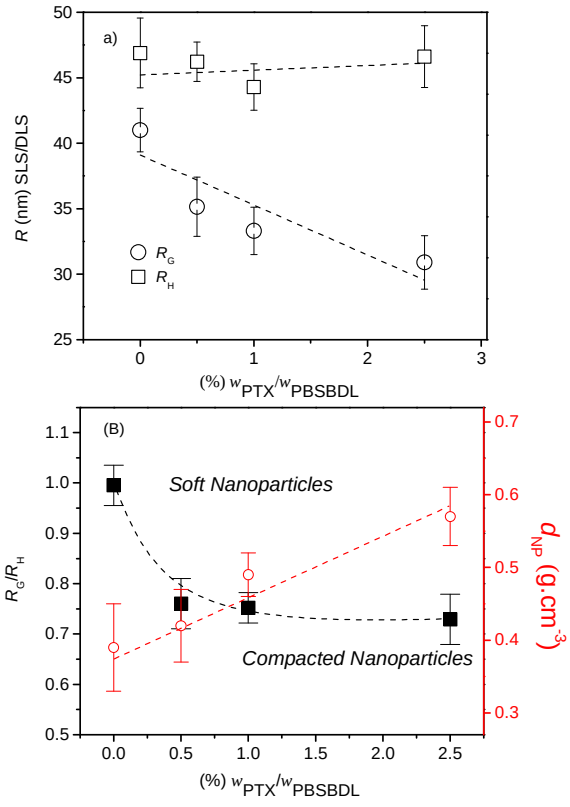

Figure 2. R_H (□) and R_G (○) (A); R_G/R_H and d_{NP} (B) for guest-free and guest-loaded PBSBDL NPs.

The reduction in R_G is clearly observed (dR_G/dwPTX = -3.82) whereas the hydrodynamic dimension (R_H) remained roughly the same (dR_H/dwPTX = +0.36). Indeed, the reduction in R_G can be also qualitatively observed in the raw SLS data (Figure 1A) where a visible reduction in the slope of the Kc/R_θ *vs.* q^2 profile is observed when comparing the guest-free to 5% *wt* guest-loaded NPs. The pronounced reduction in R_G consequently caused a reduction on the structure sensitive parameter ρ (R_G/R_H) from ~ 1.13 (guest-free) to ~ 0.78 (guest-loaded). Simultaneously, the density of the NPs linearly increased from ~ 0.37 g.mL^{-1} to ~ 0.54 g.mL^{-1} with $d\rho/dw$PTX = 0.07. These data are all reported in Figure 2. The $M_{w(NP)}$ systematically increases as a function of loaded PTX meaning that the added hydrophobic guest amount does also influence the number of aggregation of the NPs. This can be qualitatively observed by the displacement of the intercept towards lower values in Figure 1 (A). The quantitative values are given in Table 1.

Table 1. Structural parameters of guest-free and guest-loaded PBSBDL NPs.

guest-loaded	$M_{w(NP)}$ (10^8 g.mol^{-1})	d_{NP} (g.cm^{-3})	ϕ_{water} [a] (%)
0.0%	1.11	0.39	63.8
1.0 %	1.15	0.42	61.1
2.5%	1.18	0.49	54.6
5.0%	1.21	0.57	47.2

[a] determined as $[(d_{NP}/1.08) -1] \times 100$, being $d_{PBS/PBDL}$ = 1.08 g.cm^{-3}

The density of the NPs ($d_{NP} \sim M_{w(NP)}/R_H^3$; Supporting Information, Eq. S4) was calculated as described elsewhere.[16] Since the hydrodynamic dimension remains roughly constant, the increase in their density is explained by the increase in the molecular weight (or number of aggregation). Taking into account that PTX is a highly hydrophobic probe, it considerably increases the hydrophobicity of the system promoting simultaneously a favorable hydrophobic drug-polymer interaction which ultimately increases the number of aggregation of the NPs. These experimental data reflects the softness of the NPs and the transition of the inner structure from a water-swollen (guest-free NPs) towards a higher degree of compactness (guest-loaded NPs) once the increase in $M_{w(NP)}$ along to the reduction in R_G demonstrates that the overall weight of the NPs is located closer to its center of mass. The density of the guest-free NPs is reasonably low and indeed much lower than the density of the bulk PBSBDL copolyester (1.08 $g.mL^{-1}$) pointing out that the polymer chains forming the NPs are loosely packed and the assemblies are water-swollen. Based on the determined $M_{w(NPs)}$, d_{NP} and on the density of the bulk PBSBDL copolymer, the amount of water entrapped inside of NPs in such condition was estimated as 63.8% *v*/*v*. The same approach has been employed to determine the amount of water inside the assemblies as a function of the amount of guest-loaded and the results are also given in Table 1. A considerable reduction on the entrapped water is observed as the amount of PTX increases up to 5 % *wt* (from 63.8% to 47.2%). Along to the reduction in the structure sensitive parameter ($\rho = R_G/R_H$) as it is given in Figure 2, the behavior evidences the compaction of the loaded NPs.

The PBSBDL NPs shrinkage was also evidenced by SAXS (Figure 3). The SAXS data of guest-free and guest-loaded NPs were fitted by using the form factor of homogeneous spheres. This fitting approach describes the experimental results reasonably well. The electron density of PBSBDL was calculated as being equal to

0.353 e^{-} $Å^{-3}$ by using the average chemical composition of the copolyester and its density. The electron density of water (0.334 e^{-} $Å^{-3}$) is incidentally close to the one calculated for the copolyester. Consequently, contrast changes (or changes in the electron density of the NPs) are hardly seen in the collapse evolution. Nevertheless, the reduction in the dimension of the NPs caused by drug-loading is clearly evidenced by the displacement of the form-factor bump at $q \sim 0.15$ nm^{-1} towards the high-q range as higher amounts of PTX are present.

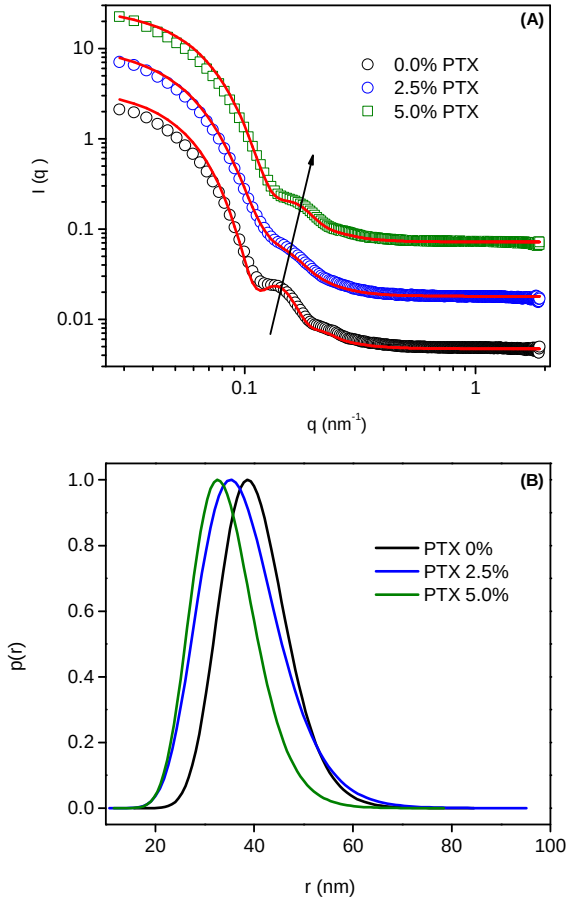

Figure 3. SAXS patterns of guest-free (○), 2.5 % $w_{PTX}/w_{PBS/PBDL}$ (○) and 5 % w_{PTX}/w_{PBSBDL} guest-loaded (□) PBSBDL NPs along to the fitting results - solid lines (A) and the respective p(r) *vs*. r profiles (B).

The average radius (R) of the NPs is reduced from 37.3 to 30.3 nm by the addition of 5 % w_{PTX}/w_{PBSBDL}. Hence, the reduction in the contrast SAXS radius (R) and in R_G confirms their collapse. Indeed, by taking into account the geometric size monitored by SAXS, there is a substantial reduction in the volume of the NPs where by loading 5 % *wt* of the guest-probe this parameter is reduced to almost half of its original value. This is surely caused by the draining process. The increase in d_{NPs} supports such conclusion.

This compaction tendency is herein claimed to be associated to the copolyester structure and with the kinetics of particle formation. The PBSBDL copolyester possesses monomeric units with distinct degrees of hydrophobicity. The butylene succinate (BS) units (derived from succinic acid) are less hydrophobic in comparison to butylene dilinoleate (BDL) (derived from saturated dilinoleic acid). Truly, the BDL segment of the polyesters is basically a branched hydrocarbon chain and therefore it is exceedingly hydrophobic. The polymer structure is given in Figure S1 of the Supporting Information File. Bearing in mind that the monomeric units are statistically distributed[15] in the polymer chains (Figure S2), an imbalance is expected between BS and BDL content in distinct copolyester chains.[17,18] Accordingly, some of the copolymer chains might contain more BS whereas others contain more BDL. During the nanoprecipitation procedure[19] the nucleation rate increases whenever the supersaturation increases.[20,21] Therefore, by the addition of the hydrophobic guest molecule, the polymer chains with higher content of BDL are spontaneously selected *via* hydrophobic interactions and they nucleate faster along to the guest probe when compared to the nucleation of the polyester chains with higher amount of BS (less hydrophobic). Consequently, it is supposed that during the earliest stages of nucleation, the primary nuclei are mainly composed by PBSBDL polymer chains with higher amount of BDL along to the

hydrophobic guest probe. As the nucleation proceeds[22] these highly hydrophobic nuclei aggregate initially since they are unstable and they give rise to matured particles “core” characterized by a high degree of compaction and low water content. Afterwards, they are presumably covered and stabilized by the less hydrophobic nuclei composed by PBSBDL polymer chains with higher amount of BS.

The soft nature of the PBSBDL NPs (guest-free) is also supported by the TEM image shown in Figure 4a. The contrast of the negatively stained particles suggests that they are substantially flattened due to drying, which is expected from liquid-like or soft objects. The apparent diameter of the particle is thus unreliable and coalescence on the carbon film cannot be excluded. The soft nature is likely due to the plasticizing effect of the long BDL chain segments which softens the PBSBDL copolyester.[23] Cryo-TEM observation was expected to provide more reliable size measurements as the particles were fast frozen inside the embedding film of water. As seen in Figure 4b, the particles are significantly smaller than those observed in dry preparations. The particle diameter typically varies from 30 to 100 nm which is in rather good agreement with the size obtained by DLS.[24]

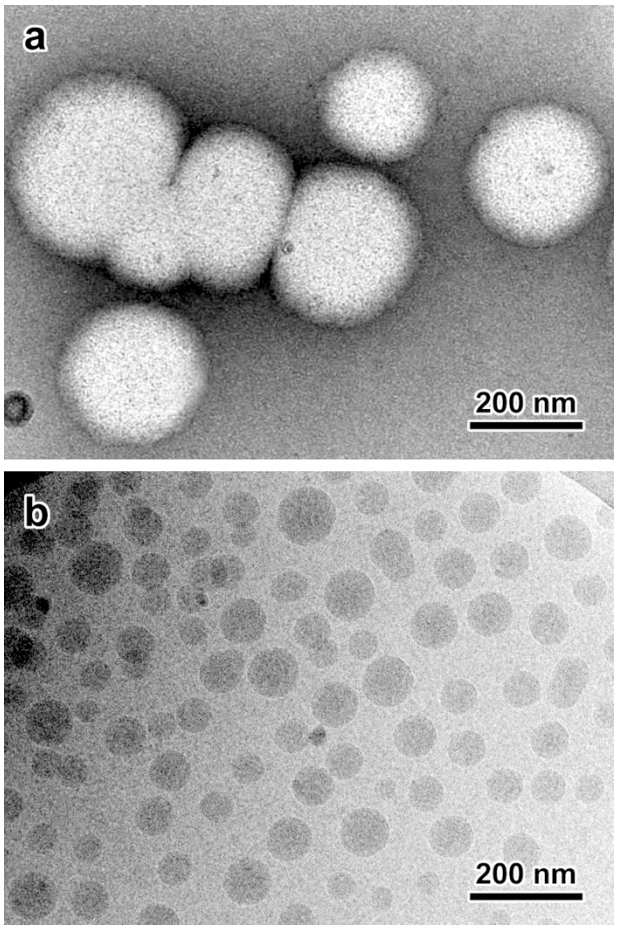

Figure 4. PBSBDL NPs observed by TEM after negative staining (a) and cryo-TEM (b).

In order to better understand these experimental evidences, the same approach has been applied to produce poly-D,L lactide (PLA) and poly(lactic-*co*-glycolic acid) (PLGA) NPs. The set of data similar to the ones reported for PBSBDL is given in Table 2 for guest-free and guest-loaded (2.0 % *wt*) NPs. It is worth mentioning that this was the highest concentration of PTX feasible to load to PLA or PLGA NPs without observing precipitation even by the naked eye. Surprisingly, in such case an opposite behavior has been observed. The increase in R_H and R_G is observed as PTX is loaded (Table 2).

Table 2. Physicochemical characteristics of the guest-loaded NPs

Entry	R_H (nm)	dispersity[a]	ζ (mV)	$M_{w(NP)}$ (10^7 g.mol^{-1})	R_G (nm)	R_G/R_H	d_{NPs} (g.cm^{-3})	d [b] (*bulk polymer*)
PLGA	31.3	0.10	-37.0	1.7	26.7	0.85	0.06	1.34
PLGA 2.0%	38.2	0.12	-30.0	3.2	32.1	0.84	0.05	
PLA	32.1	0.10	-35.0	4.7	26.0	0.81	0.06	1.32
PLA 2.0%	34.7	0.11	-32.0	10.7	31.3	0.90	0.05	
PBSBDL	46.7	0.10	-37.0	10.3	52.6	1.13	0.39	1.08

[a] estimated by using the Cumulant method; [b] g.cm^{-3}

This was also confirmed by fitting the SAXS data of such systems (Figure 5) by using the form factor of homogeneous spheres. Although the NPs are more polydisperse, the shift towards the right-hand side of the p(r) maximum as PTX is present fully confirms the size increase of the supramolecular aggregates. This is indeed understandable since opposing to PBSBDL, PLA is a homopolyester and in such a case all the chains have roughly the same hydrophobicity which therefore prevents chain-selectivity during the first steps of NPs formation. Consequently, variances are not observed during nucleation rate and one should expect the whole set of primary nuclei similar in composition. Furthermore, PLA is less hydrophobic compared to PBSBDL.**Error! Bookmark not defined.** Thus, the produced nuclei are expected to be not as compact as the ones produced from PBSBDL. This assumption is confirmed by the lower density values of PLA NPs (Table 2). Further aggregation of PLA nuclei generates particles which will reach the thermodynamic size as soon as the electrostatic repulsion stabilization quenches their growth.[15] Hence, the increase in R_G and R_H as PTX is loaded is explained by considering the higher number of polymer chains

required for the stabilization of the primary nuclei. In this case, pronounced structural changes have not been observed.

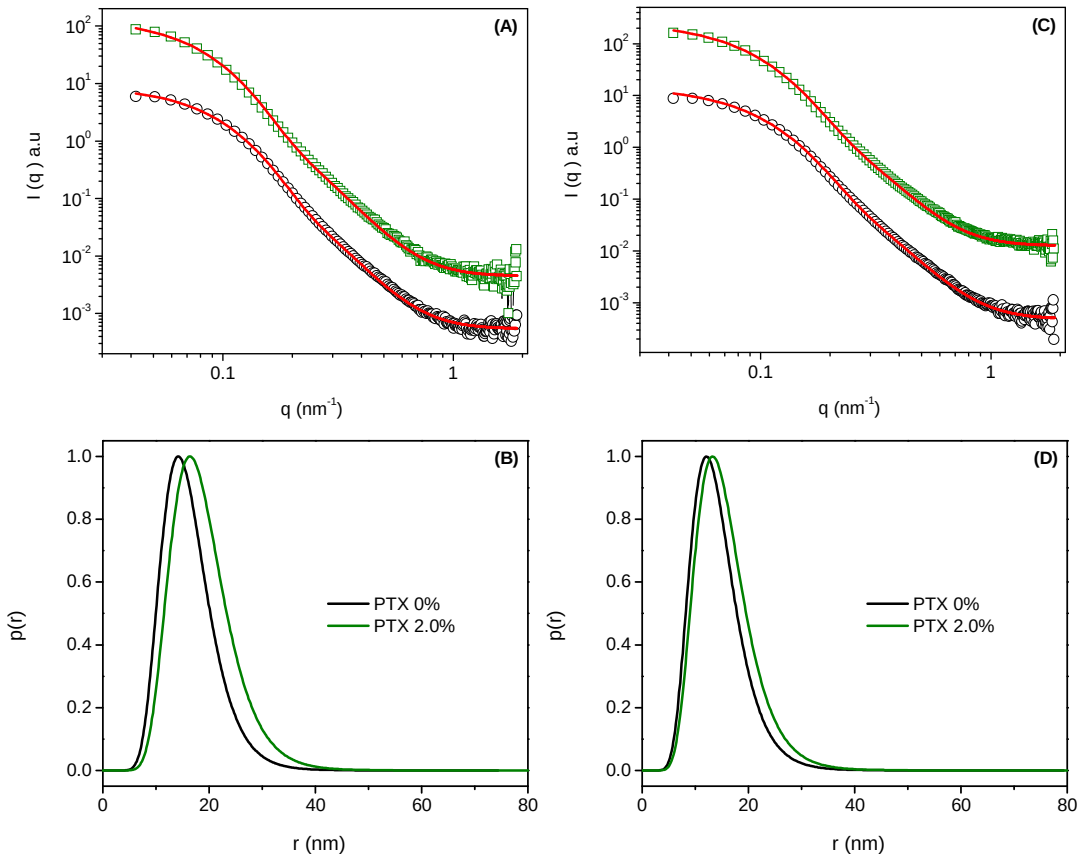

Figure 5. SAXS patterns of guest-free (○) and 2.0 % w_{PTX}/w_{PLA} guest-loaded NPs (○) (A) and respective $p(r)$ *vs.* r (B). Analogous data for PLGA NPs (C and D).

Additionally, although PLGA being statistical copolyester synthesized *via* ring opening polymerization, the similar hydrophobicity of lactide and glycolide monomeric units hides the behavior observed for PBSBDL. Consequently, the experimental results are similar to the ones observed for PLA NPs. In both cases, lower density values and higher amounts of water entrapped were determined in comparison to PBSBDL NPs (Tables 1 and 2). Likewise, previous investigations also reported similar particle density (~ 0.10 to 0.16) and entrapped water amount (~ 70 to 90%) in PLA and PLGA NPs[25]

and several studies of PLA and PLGA NPs have reported similar increases in the hydrodynamic dimensions of the NPs caused by drug entrapment.[26,27,28]

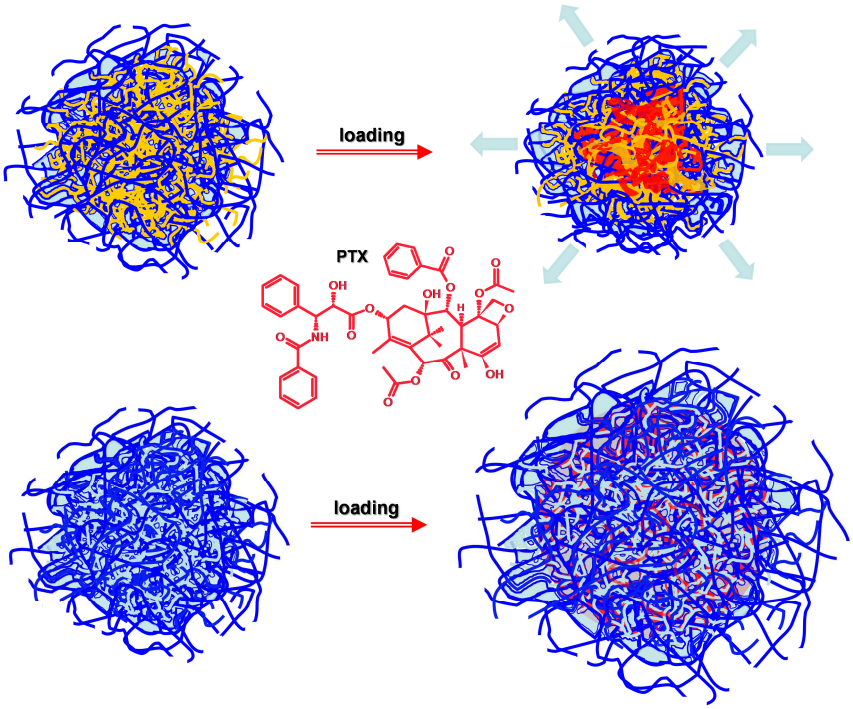

The shrinkage (PBSBDL) and swelling (PLA and PLGA) of the investigated NPs are cartooned in Figure 6.

Figure 6. Schematic representation of the hydrophobic guest loading effect in PBSBDL (top) and PLA or PLGA NPs (bottom). The hydrophobic guest molecule (PTX) is represented in red, yellow represents PBDL in the top and the islands of water are represented in light blue.

As a summary, it could be possible to demonstrate that scattering techniques are undeniably powerful tools to investigate and follow structural changes of polymeric nanocarriers induced by hydrophobic drug entrapment. These changes are connected to the chemical structure/composition and hydrophobicity of the polymer sample and guest molecule.

Conclusions

The structural changes in the inner structure of copolyester polymeric nanoparticles caused by drug loading have been investigated. The highly hydrophobic paclitaxel molecule has been used as a model probe. The combination of scattering and imaging techniques provided accurate and reliable experimental data which have been discussed with the eyes on the chemical structure and hydrophobicity of the investigated polymers. The drug encapsulation affects the inner structure of PBSBDL in a completely different way as compared to PLA or PLGA NPs. This was clearly observed specially *via* SAXS measurements. While drug loading promotes a swelling of PLA or PLGA NPs, it oppositely induces shrinkage of PBSBDL NPs. The experimental results are suggested to be related to a chain-selection during the earliest stages of aggregation where polymer chains with higher PBDL content nucleate faster along to the guest probe when compared to the nucleation of the polyester chains with higher amounts of

PBS (more hydrophilic chains). This leads to nanoparticles characterized by a dense core and containing lower amount of water entrapped. These bare structures are presumably further covered and stabilized by the less hydrophobic nuclei composed by PBSBDL polymer chains with higher amount of PBS as the process goes on. The similar chemical nature and hydrophobicity of the whole PLGA or PLA chains induces a more homogenous process of nucleation as compared to PBSBDL which consequently a dissimilar behavior. The knowledge of NPs characteristics as shown herein can lead to the tailoring of the drug release, degradation and drug cargo capacity.

Acknowledgments

The investigations have been sponsored by the Grant Agency of the Czech Republic (Grant P208/10/1600). A.J and E.J acknowledge the financial support of Charles University (Prague, CZ). F.C.G acknowledges financial support from FAPESP (Grant 2012/14087-8). The authors are grateful to European Synchrotron Radiation Facility (ESRF) and to the staff of the high brilliance beamline ID02 (proposal SC-3264).

References

[1] L.Y.T. Chou, K. Ming and W.C.W Chan. Strategies for the intracellular delivery of nanoparticles. *Chem. Soc. Rev.* **2011**, *40*, 233-245.

[2] K.L. Wooley, J.S. Moore, C. Wu, Y. Yang. Novel polymers: Molecular to nanoscale order in three dimensions. *Proc. Natl. Acad. Sci. U.S.A* **2000**, *97*, 11147-11148.

[3] M.J. Campolongo and D. Luo. Drug delivery: Old polymer learns new tracts. *Nature Mater*. **2009**, *8*, 447-448.

[4] E.M. Enlow, J.C. Luft, M.E. Napier, J.M. DeSimone. Potent Engineered PLGA Nanoparticles by Virtue of Exceptionally High Chemotherapeutic Loadings. *Nano Lett*. **2011**, *11*, 808-813.

[5] T. Hu and C. Wu. Clustering Induced Collapse of a Polymer Brush. *Phys. Rev. Lett*. **1999**, *83*, 4105-4107.

[6] Seldák, M; Koňák, Č. A new approach to polymer self-assembly into stable nanoparticles: Poly(ethylacrylic acid) homopolymers. *Macromolecules* **2009**, *42*, 7430-7438.

[7] Li, M.; Jiang, M.; Zhu, L.; Wu, C. Novel surfactant-free stable colloidal nanoparticles made of randomly carboxylated polystyrene ionomers. *Macromolecules* **1997**, *30*, 2201-2203.

[8] Giacomelli, F. C.; Riegel, I. C.; Petzhold, C. L.; Silveira, N. P.; Stepánek, P. Aggregation behavior of a new series of ABA triblock copolymers bearing short outer a blocks in b-selective solvent: From free chains to bridged micelles. *Langmuir* **2009**, *25*, 731-738.

[9] Burchard, W.; Kajiwara, K.; Nerger. Static and dynamic scattering behavior of regularly branched chains: A model of soft-sphere microgels. *J. Polymer Sci.: Polymer Physics Ed.* **1982**, *20*, 157-171.

[10] Kajiwara, K. Statistics of randomly branched polycondensates: Part 2 The application of Lagrange's expansion method to homodisperse fractions. *Polymer* **1971**, *12*, 57-66.

[11] Burchard, W. In *Light Scattering from Polymers*; Burchard, W., Patterson, G. D., Eds; Advances in Polymer Science 48; Springer-Verlag: New York, **1983**; pp.66-78.

[12] Fu, J.; Wu, C. Laser light scattering study of the degradation of poly(sebacic anhydride) nanoparticles. *J. Polym. Sci. B: Polym. Phys.* **2001**, *39*, 703-708.

[13] Fu, J.; Li, X.; Ng, D. K. P.; Wu, C. Encapsulation of phthalocyanines in biodegradable poly(sebacic anhydride) nanoparticles. *Langmuir* **2002**, *18*, 3843-3847.

[14] E. Jäger, A. Jäger, P. Chytil, T. Etrych, B. Říhova, F.C. Giacomelli, P. Štěpánek, K. Ulbrich. Combination chemotherapy using core-shell nanoparticles through the self-assembly of HPMA-based copolymers and degradable polyester *J. Controlled Rel*. **2013**, *165*, 153-161.

[15] A. Jäger, D. Gromadzki, E. Jäger, F.C. Giacomelli, A. Kozlowska, L. Kobera, J. Brus, B. Říhova, M. El-Fray, K. Ulbrich, P. Štěpánek. Novel "soft" biodegradable nanoparticles prepared from aliphatic based monomers as a potential drug delivery system. *Soft Matter* **2012**, *8*, 4343-4354.

[16] R. Šachl, M. Uchman, P. Matějíček, K. Procházka, M. Štěpánek, M. Špírkova. Preparation and characterization of self-assembled nanoparticles formed by poly(ethylene oxide)-block-poly(ε-caprolactone) copolymers with long poly(ε-caprolactone) blocks in aqueous solutions. *Langmuir* **2007**, *6*, 3395-3400.

[17] B. D. Ahn, S. H. Kim, Y. H. Kim, J. S. Yang. Synthesis and characterization of the biodegradable copolymers from succinic acid and adipic acid with 1,4-butanediol. *J. Applied Pol. Sci.* **2001**, *82*, 2808-2826.

[18] D.B. Beigzadeh, S. Sajjadi, F.A. Taromi. Kinetic study of polyesterification: unsaturated polyesters. *J. Polym., Sci. Part A. Polym., Chem.* **1995**, *33*, 1505-1510.

[19] A. M. de Oliveira, E. Jäger, A. Jäger, P. Stepánek, F. C. Giacomelli. Physicochemical aspects behind the size of biodegradable polymeric nanoparticles: A step forward. *Colloid. Surf. A*, **2013**, *436*, 1092-1102.

[20] S. M. D'Addio, R. K. Prud'homme. Controlling drug nanoparticle formation by rapid precipitation. *Adv. Drug Deliver. Rev.* **2011**, *63*, 417-426.

[21] C. E. Mora-Huertas, H. Fessi, A. A. Elaissari. Influence of process and formulation parameters on the formation of submicron particles by solvent displacement and emulsification–diffusion methods: Critical comparison. *Adv. Colloid Interface Sci.* **2011**, *163*, 90-122.

[22] E. Lepeltier, C. Bourgaux, P. Couvreur. Nanoprecipitation and the "Ouzo effect": Application to drug delivery devices. *Adv. Drug Deliver. Rev.*, **2014**, *71*, 86.

[23] A. Kozlowska, D. Gromadzki, M. El Fray, P. Stěpánek. Morphology evaluation of biodegradable copolyesters based on dimerized fatty acid studied by DSC, SAXS and WAXS. *Fib. Text. East. Eur.* **2008**, *71*, 85-88.

[24] E. Jäger, A. Jäger, T. Etrych, F.C. Giacomelli, P. Chytil, A. Jigounov, J.-L. Putaux, B. Říhova, K. Ulbrich, P. Štěpánek. Self-assembly of biodegradable copolyester and

reactive HPMA-based polymers into nanoparticles as an alternative stealth drug delivery system. *Soft Matter* **2012**, *8*, 9563-9575.

[25] Y. Zhao, J. Fu, D. K. P. Ng, C. Wu. Erosion induced controllable release of gliclazide encapsulated inside degradable polymeric particles. *Macromol. Biosci.* **2004**, *4*, 901-906

[26] C. Fonseca, S. Simoes, R. Gaspar. Paclitaxel-loaded PLGA nanoparticles: preparation, physicochemical characterization and in vitro anti-tumoral activity. *J. Controlled Rel.* **2002**, *83*, 273-286.

[27] Y. Dong, S.-S. Feng. Methoxy poly(ethylene glycol)-poly(lactide) (MPEG-PLA) nanoparticles for controlled delivery of anticancer drugs. *Biomaterials* 2004, 25, 2843-2849.

[28] D.L. Copper, S. Harirforoosh. Design and Optimization of PLGA-Based Diclofenac Loaded Nanoparticles. *PLOS One* **2014**, *9*, e87326.

TOC - Graphical Abstract

(For Table of Contents Use Only)

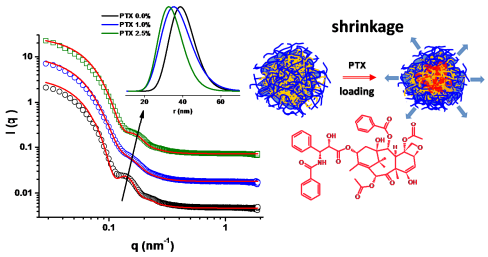
PTX 0.0%
PTX 1.0%
PTX 2.5%
I (q)
q (nm-1)
r (nm)
shrinkage
PTX
loading

Soft Matter

Dynamic Article Links

Cite this: *Soft Matter*, 2012, **8**, 9563

www.rsc.org/softmatter

PAPER

Self-assembly of biodegradable copolyester and reactive HPMA-based polymers into nanoparticles as an alternative stealth drug delivery system†

Eliézer Jäger,*[a] Alessandro Jäger,[a] Tomáš Etrych,[a] Fernando Carlos Giacomelli,[b] Petr Chytil,[a] Alexander Jigounov,[a] Jean-Luc Putaux,‡[c] Blanka Říhová,[d] Karel Ulbrich[a] and Petr Štěpánek*[a]

Received 18th May 2012, Accepted 11th July 2012
DOI: 10.1039/c2sm26150b

The surface modification of nanoparticles by physically anchoring hydrophilic biocompatible polymers is a simple and commercially attractive strategy to produce stealth drug delivery nanocarriers. Herein, we report the preparation, characterization and preliminary evaluation of the biological behaviour of polymeric nanoparticles (NPs) comprising a biodegradable poly(butylene succinate-*co*-butylene dilinoleate) – PBS/PBDL – copolyester and a non-immunogenic and non-toxic hydrophilic *N*-(2-hydroxypropyl)methacrylamide (HPMA) copolymer. Narrowly distributed sub-100 nm polymeric nanoparticles with stealth properties were successfully prepared by using a combination of interfacial nanoprecipitation and self-assembly. The assemblies were characterized by using complementary scattering techniques and cryo-transmission electron microscopy. The dimension of the NPs was found to be in the proper range to avoid fast renal clearance (D_H > 10 nm) and still below the cut-off size of the leaky pathological microvasculature of hypervascular tumours (D_H < 200 nm), thus making them candidates for application in cancer therapy based on the EPR effect. The presence of PHPMA copolymer exposed at the surface of the nanoparticles was confirmed by scattering measurements. The stealth property of the biocompatible and biodegradable NPs is responsible for their remarkable *in vitro* stability monitored in a simulated physiological environment and increased stability in concentrated NaCl solutions compared to uncoated PBS/PBDL nanoparticles, making them an alternative to PEG-shielded particles. Furthermore, a reproducible, efficient and satisfactory physical entrapment of the antitumoral drug doxorubicin (DOX) was achieved (~5.0% w_{drug}/w_{NPs}). The controlled DOX release is pH-dependent and faster under slightly acidic conditions and the cell viability experiments demonstrated that the drug-free NPs are non-toxic, whereas the DOX-loaded NPs exert *in vitro* cytostatic efficacy on EL4 T cell lymphoma.

Introduction

The use of chemotherapeutics in traditional cancer treatments is generally limited by the short blood circulation time and very low specificity of their action. Consequently, the main drawbacks are the exposure of healthy tissues to the drugs and the risk of killing and fatally damaging normal cells. The emerging field of nanomedicine provides new opportunities and different strategies to overcome the aforementioned weakness and the development of tumour-specific drug delivery nanocarriers has emerged as one of the most appealing candidates since the therapeutics can be ideally driven directly to the target tumour sites, improving the therapeutic index and limiting the exposure of healthy tissues.[1,2]

An exciting concept in nanomedicine is the use of biodegradable polymeric nanocontainers. The potential application of these nanotechnology-based drug delivery systems takes advantage of their small size, acceptable biocompatibility, high drug-loading capacity, sustained drug release rate, high cellular internalization, desired pharmacokinetics and long blood circulation half-life.[1–4] Focusing first on the size-dependency, the solid tumour-targeting drug delivery relies on the selective accumulation and uptake of therapeutics by the solid tumour due to the combination of their generally leaky microvasculature and missing or tight lymphatic capillary system. This is known as the enhanced permeability and retention (EPR) effect and such a

[a]*Institute of Macromolecular Chemistry v.v.i., Academy of Sciences of the Czech Republic, Heyrovsky Sq. 2, 162 06 Prague 6, Czech Republic. E-mail: jager@imc.cas.cz; stepanek@imc.cas.cz; Tel: +420 296 809 322; +420 296 809 211*

[b]*Centro de Ciências Naturais e Humanas, Universidade Federal do ABC, 09210-170 Santo André, Brazil*

[c]*Centre de Recherches sur les Macromolécules Végétales (CERMAV-CNRS), BP 53, 38041 Grenoble Cedex 9, France*

[d]*Institute of Microbiology v.v.i., Academy of Sciences of the Czech Republic, Vídenska 1083, 142 20 Prague 4, Czech Republic*

† Electronic supplementary information (ESI) available. See DOI: 10.1039/c2sm26150b

‡ Affiliated with Joseph Fourier University and member of the Institut de Chimie Moléculaire de Grenoble.

mechanism generally guides the principles of passive tumour-targeting. The EPR effect can be observed in almost all human solid tumours except for the hypovascular sites (prostate or pancreatic cancer).[5] Nevertheless, the EPR effect is affected by several parameters that can be either host-dependent (vascularity, vascular permeability, tumour perfusion) or nanoparticle-dependent (plasma circulation half-life, clearance, hydrodynamic size, surface charge),[6] although the size effect appears to be one of the determinant factors for the optimization of tumour-targeted drug delivery nanoparticles. Since the leaky vasculature is distinct from tumour-to-tumour, the size of the nanocarriers influences both the plasma circulation half-life and the vascular permeability. Generally, the EPR effect is optimized by using macromolecules and nanoparticles with $D_H < 100$ nm where extravasation and accumulation are inversely correlated with size.[6,7] Additionally, the EPR effect is also optimized by using nanoparticles with stealth characteristics, allowing them to escape from uptake by macrophages and from accumulation in the reticuloendothelial system (RES), thereby prolonging the circulation half-life and enhancing tumour accumulation. The blood circulating half-life of biodegradable polymer NPs can typically be enhanced by grafting, conjugating or adsorbing non-bioadhesive hydrophilic polymers[8] such as polysaccharides (usually dextran or chitosan), polyvinyl alcohol (PVA), poly(ethylene glycol) (PEG) or poly(*N*-vinyl-2-pyrrolidone) (PVP). The adsorption of hydrophilic polymers on the particle surface protects them from the interaction with macrophages and cells of the immune system and enables them to overcome opsonisation and clearance by the RES.[9] Nevertheless, despite displaying excellent non-bioadhesive properties, the mentioned hydrophilic polymers have their specific weakness and limitations when undergoing long-term applications: the polysaccharides are strong activators of the complement system,[10] PVA can reduce the uptake and sometimes must be removed to avoid associated toxicity,[11,12] while PEG and PVP can undergo oxidative degradation losing their functions *in vivo*.[13,14]

Accordingly, considerable efforts have been directed to the development of alternative bioinert polymers to improve the blood circulation time of nanomedicines.[15] Among the successful examples, the *N*-(2-hydroxypropyl)methacrylamide (HPMA) copolymers can be mentioned. These are highly hydrophilic polymers, non-immunogenic, non-toxic and characterized by an extended blood-circulation time. They have extensively been investigated as water-soluble polymeric drug delivery carriers,[16] carriers for radiochemotherapy,[17] combinatorial therapy[18] and gene delivery.[19] Additionally, several anticancer drug–HPMA copolymer conjugates have been already clinically tested.[20] The "à la carte" HPMA copolymers were also successfully used in the surface modification of polyelectrolyte complexes[21,22] where extended plasma circulation, protein-repellence and resistance to opsonisation were successfully achieved.[23]

Although the protein-repellent properties of HPMA polymers (PHPMA) are unquestionable, the self-assembly of a HPMA-based material and a degradable polyester aiming to make stealth nanoparticles has only recently been suggested.[24] However, to the best of our knowledge, this approach has never been explored. In the present paper, the preparation of stealth sub-100 nm polymeric nanoparticles through the combination of interfacial nanoprecipitation and self-assembly protocols is described. The nanomedicines were designed for potential passive targeting to solid tumours guided by the EPR effect, thus combining the desirable characteristics of biodegradable polymers while excluding some of their intrinsic limitations. The manufactured nanoparticles comprise two distinct functional components: (i) a biodegradable and biocompatible hydrophobic copolyester core that can physically encapsulate poorly water-soluble bioactive drugs *via* hydrophobic interactions and (ii) a stealth non-immunogenic and non-toxic "à la carte" hydrophilic copolymer surface providing stability to the NPs in simulated biological environments and enabling further development of targeting strategies based on the use of multiple ligands on a single surface. The dynamics and structure of the prepared polymeric nanoparticles have been characterized by small-angle X-ray scattering (SAXS), light scattering and cryo-transmission electron microscopy (cryo-TEM). Their preliminary effectiveness in the biomedical field was evaluated *in vitro* in a cytostatic model.

Experimental section

Materials and reagents

Dimerized fatty acid (DFA), dilinoleic acid (DLA) Pripol 1009 (Croda Coatings & Polymers), 1,4-butanediol (BD) (BASF), succinic acid (SA) (Aldrich Chemie) and acetone (Merck) were used as received. Tetrabutoxytitanium (TBT) used as a catalyst, methacryloyl chloride and 2,2′-azobis(isobutyronitrile) (AIBN) were purchased from Sigma-Aldrich. All other chemicals and solvents were of analytical grade. Human plasma was purchased from Sigma-Aldrich. The water was ultrapure MilliQ®. Doxorubicin hydrochloride (DOX·HCl) was purchased from Meiji Seiko (Japan).

Synthesis procedures

Synthesis of the PBS/PBDL copolyester. The synthesis of poly(butylene succinate-*co*-butylene dilinoleate), herein referred to as PBS/PBDL, was performed following the two-stage melt polycondensation (esterification and polycondensation) similar to the protocol recently described.[25] In a glass reactor SA, DLA and BD in molar ratio 1/1.2 and the catalyst TBT (4×10^{-4} mol mol^{-1} diacids) were loaded. The vessel was further evacuated and filled with argon. The reaction mixture was heated at 200 °C and stirred at a constant speed (400 rpm). This first step (esterification) was considered complete after the collection of the theoretical amount of H_2O, which was removed from the reaction mixture by distillation and collected in a graduated cylinder. The polycondensation reaction was carried out at 245 °C, ~0.8 hPa, and it has been considered complete when the observed power consumption of the stirrer motor signaled that the polymer of highest melt viscosity was obtained. The copolyester was purified by dissolution in chloroform and further precipitation in methanol. The number-average molecular weight (M_n) and molecular weight distribution (polydispersity, M_w/M_n) of the synthesized copolymer were determined by SEC (Deltachrom pump, Watrex Comp., autosampler Midas, Spark Instruments, two columns with PL gel MIXED-B LS (10 μm), separating in the range of molar masses approximately 400–1 × 10^7 g mol^{-1}). Tetrahydrofuran (THF) was used as the mobile phase at a flow-rate of 0.5 mL min^{-1}. The injection-loop volume was 0.1 mL.

Measurements were performed with triple viscosity/concentration/light-scattering detection. The set was connected to a light-scattering photometer DAWN DSP-F (Wyatt Technology Corp.) measuring at 18 angles of observation, a modified differential viscometer, Viscotek model TDA 301 (without internal light scattering and concentration detectors), and a differential refractometer, Shodex RI 71. The data were accumulated and processed using the Astra and triSEC software following the previously described methodology.[25]

^{1}H NMR and ^{13}C NMR spectra were performed on a Bruker AMX-300 spectrometer at 25 °C operating at 300.1 MHz (^{1}H NMR) or 75.5 MHz (^{13}C NMR). The PBS/PBDL copolyester was dissolved in deuterated chloroform ($CDCl_3$) and the spectra were internally referenced to tetramethylsilane (TMS). Sixty-four scans for ^{1}H NMR and 1000–10 000 scans for ^{13}C NMR were acquired with 32 K and 62 K data points and delay times of 1 and 2 s respectively. Quantitative ^{1}H NMR spectra were recorded with a pulse width of 6 ms ($\pi/3$) and a delay time of 20 s. For ^{13}C NMR, the pulse and spectral widths were 4.3 ms ($\pi/2$) and 18 kHz respectively.

Synthesis of the PHPMA–chol (amphiphilic copolymer based on HPMA bearing covalently bound cholesterol anchor). *N*-(2-Hydroxypropyl)methacrylamide (HPMA) was synthesized as previously described[26] using K_2CO_3 as a base: m.p. 70 °C, purity > 99.8% (HPLC), elemental analysis: calc. C 58.72%, H 9.15%, N 9.78%; found C 58.98%, H 9.18%, N 9.82%. Cholest-5en-3β-yl 6-methacrylamido hexanoate (MA-εAhx-cholesterol) was prepared by the reaction of MA-εAhx-OH with cholesterol as described elsewhere:[27] m.p. 98–100 °C, elemental analysis: calc. C 78.25%, H 10.83%, N 2.47%; found C 78.73%, H 10.85%, N 2.34%, TLC: ethyl acetate/hexane (1 : 1) Rf = 0.8. ^{1}H NMR ($CDCl_3$): δ 5.81 br, 1H (NH); δ 5.65 and 5.29 d, 2H (CH_2=C(CH_3)CO); δ 4.58 m, 1H (CO–O–CH–(CH_2)$_2$); δ 3.30 m, 1H (CH_2–NH); selected peaks of cholesterol part of the molecule: δ 5.35 t, 1H (C–CH–CH_2); δ 0.66 s, 3H (C(18)H3). The structure and purity of the monomers were examined by ^{1}H-NMR (Bruker spectrometer, 300 MHz) and HPLC (Shimadzu 10VP) using a C_{18} reverse-phase Chromolith Performance RP-18e (4.6 × 100 mm) column with diode array detection. The eluent was water–acetonitrile with gradient 5–95 vol% acetonitrile, 0.1% TFA and flow-rate = 1 mL min^{-1}.

The polymer precursor PHPMA–chol was prepared by solution free radical polymerization of HPMA and MA-εAhx-cholesterol in methanol using AIBN as initiator: AIBN (0.6 wt%), monomers (18 wt%), molar ratio HPMA/MA-εAhx-cholesterol (97.2 : 2.8). Subsequently, 256.1 mg (1.79 mmol) of HPMA and 30.0 mg (0.05 mmol) of MA-εAhx-cholesterol were dissolved in 1.7 mL of methanol. The solution was poured into a glass ampoule, purged with N_2 and sealed. After 22 h in a water bath kept at 60 °C, the ampoule was cooled and the reaction mixture was poured into an excess of acetone (45 mL). The precipitate was filtered and vacuum-dried. The number-average molecular weight (M_n) and molecular weight distribution (polydispersity, M_w/M_n) of the synthesized copolymer were determined by SEC: a Shimadzu HPLC system equipped with TSKgel G3000SWxl (300 × 7.8 mm; 5 μm), and UV-Vis, refractive index Optilab-rEX and multiangle light scattering DAWN EOS detectors (Wyatt Technology Co.). The eluent was methanol–sodium acetate buffer (0.3 M; pH 6.5) (80 : 20 vol%) for the TSKgel column; flow-rate 0.5 mL min^{-1}.[27] The content of cholesterol in the hydrophilic polymer was determined by ^{1}H NMR (Bruker spectrometer, 300 MHz) in $(CD_3)_2SO$ and the integral intensities of ^{1}H NMR spectra were compared: δ 5.32 t, 1H (C=CH of cholesterol); δ 8.05 d; δ 3.68 Br, 1H (CH–OH of HPMA).

Preparation of the nanoparticles

The preparation of NPs exhibiting stealth properties was successfully achieved by using a combination of interfacial nanoprecipitation and self-assembly protocols. The PBS/PBDL (5.0 mg mL^{-1}) was first solubilized in acetone at 40 °C. The standard light scattering characterization of the organic polymer solution evidenced only the presence of molecularly dissolved PBS/PBDL chains (R_H = 9.5 nm). Subsequently, the organic phase was added dropwise (EW-74900-00, Cole-Parmer®) into a pre-heated (40 °C) 5% v/v ethanol–water mixture (20 mL) containing 0.00 mg mL^{-1} (NP0), 0.25 mg mL^{-1} (NP1 : 20 $w_{HPMA–chol}/w_{PBS/PBDL}$), 0.50 mg mL^{-1} (NP1 : 10 $w_{HPMA–chol}/w_{PBS/PBDL}$), 0.75 mg mL^{-1} (NP1 : 6.7 $w_{HPMA–chol}/w_{PBS/PBDL}$), 1.00 mg mL^{-1} (NP1 : 5 $w_{HPMA–chol}/w_{PBS/PBDL}$) or 2.00 mg mL^{-1} (NP1 : 2.5 $w_{HPMA–chol}/w_{PBS/PBDL}$) of dissolved ($R_H$ = 8.0 nm) PHPMA–chol free chains (Ultra-Turrax T25, IKA, Germany). The samples were left at room temperature for 2 h to achieve equilibrium structures and the organic solvent was further removed by evaporation under reduced pressure. The remaining free polymer chains were removed by washing the NP solution several times using an Amicon Ultra-4 centrifugal filter with MWCO 30 kDa (Millipore, Czech Republic). The aqueous solutions were concentrated to the desired final concentrations and used immediately or stored at 4 °C. The DOX-loaded NPs were prepared by using essentially the same procedure except that in such a case 4.3 μmol of DOX·HCl and 12.9 μmol of triethylamine were dissolved in acetone along with the PBS/PBDL copolyester.

Scattering characterization of the nanoparticles

Dynamic light scattering (DLS). The DLS measurements were performed using an ALV CGE laser goniometer consisting of a 22 mW HeNe linear polarized laser operating at a wavelength (λ = 632.8 nm), an ALV 6010 correlator, and a pair of avalanche photodiodes operating in the pseudo cross-correlation mode. The samples were loaded into 10 mm diameter glass cells and maintained at 25 ± 1 °C. The data were collected using the ALV Correlator Control software and the counting time was 90 s. The measured intensity correlation functions $g_2(t)$ were analyzed using the REPES algorithm,[28] resulting in the distribution of relaxation times shown in equal area representation as $\tau A(\tau)$. The mean relaxation time or relaxation frequency ($\Gamma = \tau^{-1}$) is related to the diffusion coefficient (D) of the nanoparticles as $D = \Gamma/q^2$ where $q = 4\pi n\sin(\theta/2)/\lambda$ is the scattering vector, n the refractive index of the solvent and θ the scattering angle. The hydrodynamic radius (R_H) or the distributions of R_H were calculated by using the Stokes–Einstein relation:

$$R_H = \frac{k_B T}{6\pi\eta D} \quad (1)$$

where k_B is the Boltzmann constant, T the absolute temperature and η the viscosity of the solvent. At least 5 measurements were made of each sample to check the repeatability. The polydispersity of the nanoparticles was accessed by using the cumulant analysis[28] of the correlation functions measured at 90° as:

$$\ln g_1(t) = \ln C - \Gamma t + \frac{\mu_2}{2} t^2 \quad (2)$$

where C is the amplitude of the correlation function and Γ is the relaxation frequency (τ^{-1}). The parameter μ_2 is known as the second-order cumulant and it was used to compute the polydispersity index of the samples (PDI = μ_2/Γ^2).

Static Light Scattering (SLS). In the SLS mode, the samples were loaded into quartz cells (Hellma, Germany) and the scattering angle was varied from 30 to 150° with a 10° stepwise increase. The absolute light scattering is related to the weight-average molecular weight ($M_{w(NP)}$) and to the radius of gyration (R_G) of the nanoparticles by the Zimm formalism represented as:

$$\frac{K_c}{R_\theta} = \frac{1}{M_{w(NP)}}\left(1 + \frac{R_G{}^2 q^2}{3}\right) \quad (3)$$

where K is the optical constant which includes the square of the refractive index increment (dn/dc), R_θ is the excess normalized scattered intensity (toluene was applied as standard solvent) and c is the polymer concentration given in mg mL^{-1}. The refractive index increment (dn/dc) of PBS/PBDL NPs (0.153 mL g^{-1}) and PHPMA–chol (0.167 mL g^{-1}) in pure water was taken from the previous literature.[21,25] The estimation of the concentrations and refractive index increments of the NPs as a function of the molar mixing ratio was performed on the basis of the model of complex formation.[29]

The average density of the nanoparticles (d) was estimated as:

$$d = \frac{3M_{w(NP)}}{4\pi N_A (R_H)^3} \quad (4)$$

with N_A being Avogadro's number.

Electrophoretic Light Scattering (ELS). The ELS measurements were employed in order to determine the average zeta potential (ζ) of the nanoparticles, which was done by using the Zetasizer NanoZS instrument (Malvern Instruments, UK). The equipment measures the electrophoretic mobility (U_E) and converts the value to ζ-potential (mV) through Henry's equation. Henry's function was calculated through the Smoluchowski approximation. The measurements were performed at 25 °C and the reported ζ-potential values are the average of 10 measurements.

The fixed aqueous layer thickness (FALT) was calculated according to the Guy-Chapman theory.[30] Zeta potentials were measured in various NaCl concentrations and plotted against k, with k^{-1} being the Debye-length, that is, $3.3\sqrt{c + 0.0056}$ (c is the concentration of NaCl). Therefore, by plotting ln ζ *vs.* k, the slope gives the thickness (L) of the adsorbed hydrophilic polymer layer.

Small-Angle X-ray Scattering (SAXS). The SAXS data were collected using a pinhole camera (Molecular Metrology SAXS System) attached to a microfocused X-ray beam generator (Osmic MicroMax 002) operating at 45 kV and 0.66 mA (30 W) and yielding a beamline with wavelength λ = 1.54 Å. The camera was equipped with a multiwire, gas-filled area detector with an active area diameter of 20 cm (Gabriel design). The solutions were poured into 2 mm diameter glass capillaries and sealed. The scattering patterns were collected after an exposure time of about 2 h on average. The 2D-images were found to be isotropic and were normalized by the sample transmission and further converted to $I(q)$ *vs.* q profiles. The resulting $I(q)$ *vs.* q scattering curves were corrected by subtraction of the scattering of pure water and further placed on an absolute scale using glassy carbon as standard.

Cryo-Transmission Electron Microscopy (Cryo-TEM)

Cryo-TEM observations were performed to characterize the size and morphology of the polymeric nanoparticles. Thin liquid films of NP suspensions (0.5 wt% solid content) were prepared on NetMesh lacy carbon membranes (Pelco, USA) and quench-frozen in liquid ethane. Once mounted in a Gatan 626 cryo-holder cooled with liquid nitrogen, the samples were transferred to the microscope and observed at low temperature (−180 °C). The images were recorded on Kodak SO163 films using a CM200 Philips "Cryo" electron microscope operating at 80 kV. The negatives were digitized and the diameter of 650 particles was measured for each sample using the ImageJ software.[31] Number-, weight- and Z-average mean diameters ($\overline{D_N}$, $\overline{D_W}$ and $\overline{D_Z}$, respectively), as well as a polydispersity index P_{TEM}, were calculated as:

$$\overline{D_N} = \frac{\sum_i N_i D_i}{\sum_i N_i};\ \overline{D_W} = \frac{\sum_i N_i D_i{}^4}{\sum_i N_i D_i{}^3};\ \overline{D_Z} = \frac{\sum_i N_i D_i{}^6}{\sum_i N_i D_i{}^5} \quad (5)$$

$$P_{TEM} = \frac{\overline{D_W}}{\overline{D_N}} \quad (6)$$

Drug loading and encapsulation efficiency

The total amount of DOX loaded into the NPs was determined by subtracting the unloaded DOX (collected after the washing steps) from the total DOX feeding. First, a mixture of 0.1 mL of the drug-loaded NPs and 0.1 mL of buffer (0.2 M Na_2CO_3/$NaHCO_3$, pH 9.8) was extracted with 0.8 mL of chloroform. Subsequently, the DOX amount was determined in the chloroform phase by using a standard UV/Vis spectrometer operating at 488 nm and referenced to a DOX calibration curve in chloroform. The drug-loading content (LC) and drug encapsulation efficiency (LE) were determined by using the following equations:

$$\text{LC (\%)} = \frac{\text{drug amount in nanoparticles}}{\text{mass of nanoparticles}} \times 100 \quad (7)$$

$$\text{LE (\%)} = \frac{\text{drug amount in nanoparticles}}{\text{drug feeding}} \times 100 \quad (8)$$

Drug release experiments

The drug release experiments were carried out at 37 °C in pH-adjusted release media (pH 7.4 and 5.0). Aliquots (500 μL) of drug-loaded NPs were loaded into 36 Slide-A-Lyzer MINI dialysis microtubes with MWCO 10 kDa (Pierce, Rockford, IL). These microtubes were dialyzed against 3 L of pH-adjusted PBS buffer gently stirred. The drug release experiments were performed in triplicate. At each sampling time, three microtubes were removed from the dialysis system and 0.1 mL from each microtube was sampled and the remaining drug was extracted by using chloroform as described above. The reported data are expressed as the amount of released DOX relative to the total DOX content in the NPs.

Stability of the nanoparticles in simulated physiological media

The stability of the NPs in diluted human plasma was performed as previously described.[32] Briefly, the NPs were incubated in 10% v/v human plasma (Sigma-Aldrich, Czech Republic) at 37 °C under gentle stirring at a concentration equal to 1 mg mL^{-1}. At each sampling time, an aliquot of the NPs was collected and the DLS measurements were performed in triplicate to probe the hydrodynamic radius and size-dispersity index of the entities. The hydrodynamic radius and size-dispersity of the NPs as a function of ionic strength (NaCl) were also determined (as described above).

Cell culture

Mouse splenocytes. The mice (C57B/6, H-2^b; Balb/c, H-2^d) were killed by cervical dislocation. The spleens were removed aseptically, stripped of fat and placed in an ice-cold RPMI 1640 culture medium (Sigma, USA) supplemented with 4 mM L-glutamine, 50 mM 2-mercaptoethanol, 1 mM sodium pyruvate, 4.5 g L^{-1} glucose, antibiotics (penicillin/streptomycin, Sigma, USA), and 10% v/v heat-inactivated fetal calf serum (FCS). Cells were grown in cultivation flasks at 37 °C with 5% CO_2. Single-cell suspensions were obtained by gentle homogenization of mouse spleen in a tissue homogenizer. The spleen lymphocytes were separated from the debris and then washed twice (5 min at 800 × *g* at 4 °C). Red blood cells were lysed with Tris-buffered ammonium chloride solution. Lymphocyte viability was assessed by the Trypan Blue exclusion test. The viability of the cells used was always >95%.

Proliferation assay of mouse splenocytes. In order to estimate cell proliferation, [^{3}H]-thymidine incorporation was assessed using a [^{3}H]-thymidine incorporation assay. NUNCLON 96-well, flat-bottomed plates were seeded with 5×10^4 splenocytes per well. Concentrations from 0.01 to 1.00 mg mL^{-1} of NPs were then added to the wells to a final well volume of 200 μL. The plates were cultured in 5% CO_2 for 48 h at 37 °C. Before the last 6 h of incubation, 18.5 kBq of [3H]-thymidine was added per well. The cells were then collected onto glass fiber filters (Filtermat, Wallac, Finland) using a cell harvester (Tomtec, Orange, CT). After drying, the fibre filter was placed into a sample bag, a solid scintillator-Meltilex (Wallac) was applied and the bags were sealed (Microsealer, Wallac). Counting was performed in a 1450 MicroBeta Trilux (Wallac). Cells cultivated in fresh medium were used as control. The results were calculated as the arithmetic mean of the c.p.m. in four individual wells. The stimulation index (SI) was calculated by the following formula:

$$\mathrm{SI} = \frac{\text{mean cpm in cell cultures}}{\text{mean cpm in control cultures}} \quad (9)$$

Cancer cell line

Murine T cell EL4 T cell lymphoma was purchased from the American Type Culture Collection (ATCC, Rockville, MD, USA) and cultured as described above. The cytostatic potential of the NPs was assessed using a [^{3}H]-thymidine incorporation assay as mentioned above. NUNCLON 96-well, flat-bottomed plates were seeded with 5×10^4 per well of EL4 cells.

Results and discussion

Synthesis and characterization of the starting polymers

The structure of the synthesized poly(butylene succinate-*co*-butylene dilinoleate) PBS/PBDL copolyester (core-forming NPs) and of the PHPMA–chol (stabilizing shell-forming NPs) is depicted in Fig. 1. The number-average molecular weight (M_n) of PBS/PBDL was estimated by SEC (Fig. S1a, ESI†) as 32.0 kDa and it holds a reasonable degree of polydispersity (M_w/M_n = 1.76). The composition of the copolyester was determined from ^{1}H and ^{13}C NMR data (Fig. S2, ESI†) by using the relative integrals of SA arising from PBS (*a* or *b*) and the dimerized fatty acid from PBDL (*c* or *d*). The ratio composition was calculated as 3 : 1 (PBS : PBDL) which leads to the weight segment composition of 50/50 w/w. The characteristic signals of the "couplings" in the ^{1}H-NMR and ^{13}C-NMR spectra were not found, confirming statistical distribution of monomer units. This was also supported by ^{13}C NMR spectra, which describes the division of the carbonyl groups (C=O) in the copolymer, area ~ 64 ppm (Fig. S3†). Both signals of carbonyl groups correspond to the ratio 3 : 1.

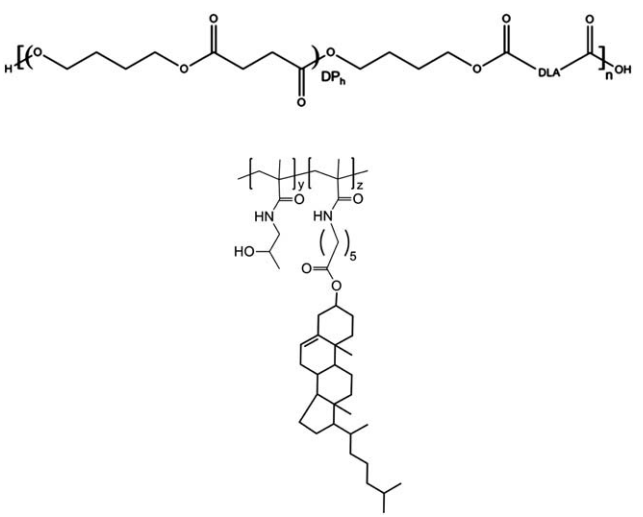

Fig. 1 Molecular structure of the PBS/PBDL copolyester (top) and PHPMA–chol (bottom).

The "à la carte" PHPMA–chol was synthesized by having M_w = 32.5 kDa and M_w/M_n = 1.65 as determined by SEC (Fig. S1b†). The polymer M_w ranging between 30 and 35 kDa ($M_w/M_n \sim 1.8$) was selected to have all polymer fractions below the renal threshold ($M_w \sim 50$ kDa) therefore allowing the amphiphile to undergo "renal clearance" and thus avoiding accumulation of polymeric material in the body in possible further *in vivo* applications.[27] Previously, the HPMA-based copolymers with cholesterol contents between 1.5 and 6.0 mol% were evaluated (data not shown). Nevertheless, to allow adequate solubilization, the cholesterol content was chosen to be 2.8 mol% during the preparation of the NPs.

Preparation and characterization of the nanoparticles

The successful preparation and characterization of novel sub-100 nm diameter biodegradable and biocompatible PBS/PBDL surfactant-free NPs was recently reported.[25] The biodegradable NPs are composed of a water-swollen inner structure which is responsible for a relatively fast degradation rate which is a critical parameter for drug delivery application. Nevertheless, uncoated PBS/PBDL NPs are unstable in a simulated physiological environment due to the screening of the surface charge by salt ions. Accordingly, they require a stealth surface to avoid undesirable interactions therefore prolonging their blood circulation time, which is a prerequisite for achieving the time-dependent tumor tissue accumulation of these drug delivery vessels. Herein, the NP self-assembly and the particular features of an introduced PHPMA hydrophilic surface have been investigated.

The formation of the NPs is explained by the nucleation–aggregation mechanism.[33] When the solution is sufficiently saturated, critical nuclei of pure solute are formed and they grow by capturing solute molecules from the surroundings. Nevertheless, when PHPMA–chol is present in the aqueous medium, impure nuclei formation is expected since PHPMA–chol will nucleate along with PBS/PBDL. Accordingly, PHPMA–chol might stabilize the system, reducing the surface tension between water and the polymer solution, leading to smaller and narrowly distributed polymeric NPs. Consequently, the PHPMA–chol is responsible for the interface between the hydrophobic copolyester and the external aqueous environment, although the presence of PHPMA–chol copolymer chains entrapped inside the NPs and the formation of a small fraction of free amphiphiles could not be completely prevented using the current method.

Typical autocorrelation functions measured at 90° and the respective normalized distributions of R_H for NPs prepared at different $w_{HPMA-chol}/w_{PBS/PBDL}$ ratios are given in Fig. 2.

The q^2-dependence of the relaxation frequency Γ (Fig. 2c) suggests the Brownian diffusive motion of the particles. The experimental data suggest that up to 1 : 5 $w_{HPMA-chol}/w_{PBS/PBDL}$ single narrowly distributed nanosized particles are obtained (Fig. 2b). The physicochemical characteristics of the produced NPs are summarized in Table 1.

The NPs distribution width calculated by the cumulant method is relatively narrow, ranging from 0.08 to 0.12. The size of the stealth NPs ($2R_H$ < 100 nm) always remains below the cut-off size of the leaky pathological vasculature, possibly making them suitable candidates for use in cancer therapy based on the EPR

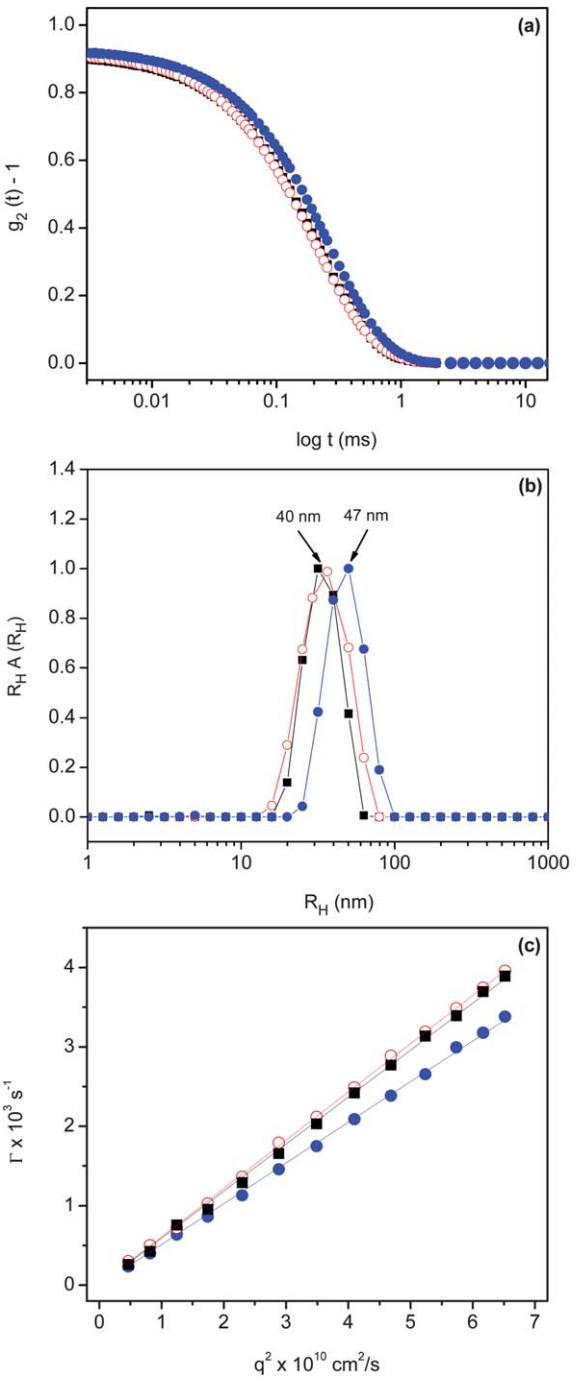

Fig. 2 Autocorrelation functions $g_2(t)$ measured at 90° (a), respective distributions of R_H as revealed by the REPES analysis (b) and q^2-dependence of Γ (c) for NP0 (●), NP1 : 20 (■) and NP1 : 5 (○) in water at 25 °C.

effect. The determined ζ-potentials at about −38 mV prevent the aggregation of the particles due to electrostatic repulsion. The negative ζ-potentials are attributed to the delocalization of the negative charges of the ester bonds[25,34] and to the negative charges of the partially ionized carboxylic groups of PBS/PBDL. Furthermore, it is important to note that the PHPMA coated nanoparticles (up to 1 : 5 $w_{HPMA-chol}/w_{PBS/PBDL}$) were stable for months when stored at 4 °C, where the hydrodynamic diameter,

Table 1 Physicochemical characteristics of the produced NPs as determined by DLS/SLS and zetametry

Entry	R_H (nm)	Dispersity[a]	ζ (mV)	$M_{w(NP)}$ (10^7 g mol^{-1})	R_G (nm)	d (g mL^{-1})	L^b (nm)
NP0	47.0	0.10	−37.0	12.9	47.0	0.49	0.0
NP1 : 20	40.0	0.10	−40.0	5.78	35.0	0.36	1.8
NP1 : 10	38.0	0.09	−39.0	4.25	32.0	0.28	2.2
NP1 : 6.7	37.0	0.08	−39.0	3.85	28.0	0.28	2.3
NP1 : 5	40.0	0.12	−35.0	4.04	37.0	0.24	2.5

[a] Estimated using the cumulant method. [b] Thickness of the adsorbed PHPMA layer.

size distribution and light scattering intensity remained roughly constant (not shown here). Nevertheless, higher amounts of PHPMA–chol led to a reasonable increase in the NP dispersity index (0.16). This can be explained by the presence of PHPMA–chol aggregates as it was evidenced by DLS even after the washing steps (ESI, Fig. S4†). This is typically observed when an excess of standard surfactants is used to stabilize biodegradable polymeric NPs[35] leading to the formation of secondary structures.[2,35,36] The excess of stabilizers is not desired since it leads to sample instability mainly manifested by the broadening of size distribution. Hence, further experiments were limited to $w_{HPMA-chol}/w_{PBS/PBDL}$ equal to 1 : 5.

The SLS results for NP0 and NP1 : 6.7 are shown in Fig. 3. The radius of gyration R_G of the NPs and their molecular weight $M_{w(NP)}$ were estimated from the slope of the curves and from the inverse of the intercepts (eqn (3)), respectively.

The structure-sensitive parameter $\rho = R_G/R_H$ related to the shape and inner structure of the NPs, and their density (eqn (4)) could also be determined. The comparison to the naked NP0 confirms that the parameters $M_{w(NP)}$, R_H, R_G and d are influenced by the addition of PHPMA–chol (Table 1). The presence of the PHPMA–chol clearly results in a reduction in $M_{w(NP)}$ and R_H. Generally, the use of stabilizers (standard surfactants) leads to reductions in the size of biodegradable NPs prepared by nanoprecipitation.[2,35,37] This points out that the NPs are composed of a smaller number of PBS/PBDL chains. The density and ρ-values and, consequently, the inner structure of the nanoparticles are also influenced by the presence of the hydrophilic PHPMA–chol. It is well established that the R_G/R_H ratio is related to the shape of NPs where ρ-values of 0.775, 1.78, and ≥ 2 have been reported for hard spheres, random coils and rod-like structures, respectively.[38] The ρ-value of spherical objects depends on their inner structure and compactness,[39] being close to 0.775 for compact spheres, 0.8–0.9 for block copolymer micelles due to solvation phenomena[40] and ~1.0 for hollow spheres and vesicles. Fig. 4 shows R_G/R_H and density (d) of the nanoparticles as a function of PHPMA–chol concentration.

The density continuously decreases due to the formation of a progressively highly hydrated nanoparticle as the PHPMA–chol concentration increases. Simultaneously, R_G decreases whereas R_H remains nearly constant (Table 1), which results in the reduction of $\rho = R_G/R_H$ (Fig. 4) up to PHPMA–chol of 0.75 mg mL^{-1}. It is important to note that, in such concentration regime, the PHPMA is responsible for a maximum of 13% of the overall NP mass ($w_{HPMA-chol}/w_{PBS/PBDL}$) which implies that the R_G/R_H ratio is chiefly governed by the properties of the PBS/PBDL hydrophobic biodegradable copolyester. Accordingly, the observed trend is attributed to the shrinking of the hydrophobic core of the nanoparticles.[41]

It has been recently demonstrated that the PBS/PBDL NPs are loosely packed and not fully collapsed. Therefore, they are characterized by a water-swollen inner structure.[25] The current results evidence that the addition of PHPMA–chol leads to the formation of more collapsed nanoparticles (as suggested by the reduction of the R_G/R_H factor). Presumably, chol–PBS/PBDL hydrophobic interactions are likely to occur, favoring a draining process and therefore the collapsing of the PBS/PBDL segment. On the other hand, the hydrophilic and thus highly hydrated PHPMA segment is exposed as the outer shell of the self-assembled NPs leading to the reduction in the overall density of the NPs as schematically

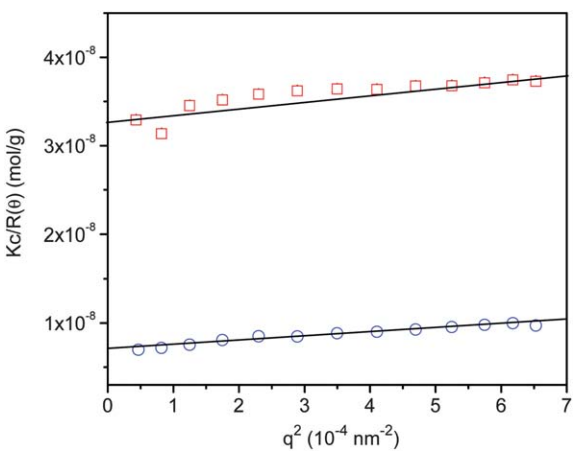

Fig. 3 Static light scattering measurements (K_c/R_θ *vs.* q^2) for NP0 (○) and NP1 : 6.7 (□) in water at 25 °C.

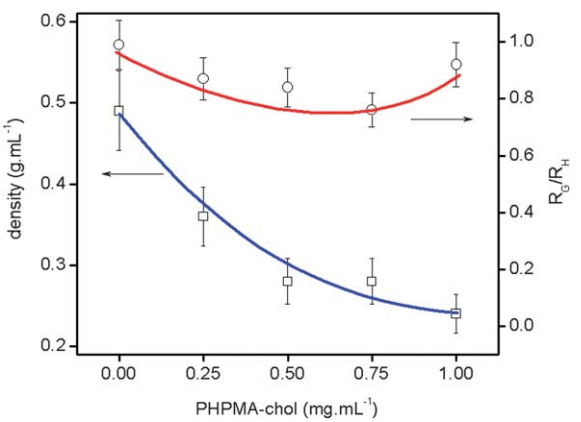

Fig. 4 R_G/R_H and density of the nanoparticles (d) as a function of PHPMA–chol concentration.

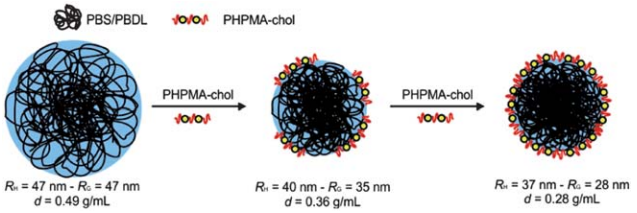

Fig. 5 Schematic representation of the prepared NPs: NP0 (left), NP1 : 20 (middle) and NP1 : 6.7 (right).

represented in Fig. 5. These considerations are fully corroborated by the results reported in Fig. 4. A similar behavior has previously been evidenced in the self-assembly of poly(lactid acid) (PLA) and dextran bearing phenoxy groups.[42]

Furthermore, the increase in PHPMA–chol concentration (from 0.75 to 1.0 mg mL^{-1}) resulted in an increase in R_G of the NPs. Since R_H is about 40 nm, the structure-sensitive parameter ρ has increased to 0.92. The increase is supposed to be related to the PHPMA–chol content. In NP1 : 5, the PHMPA–chol is responsible for ~17% of the overall mass of the NPs. Consequently, as the PHPMA–chol concentration is increased to 1.0 mg mL^{-1}, a thicker hydrophilic surface is produced which is supposed to influence the R_G/R_H ratio more pronounced. Since this is a highly hydrated layer, the whole particle becomes softer as revealed by the increase in ρ-value.

The SAXS measurements confirmed the presence of the PHPMA layer at the surface of the nanoparticles. $I(q)$ *vs.* q represents the form factor $P(q)$ reflecting their size and shape. Fig. 6 shows the representative SAXS pattern of NP1 : 5 in water at 25 °C.

The high-q range profile of the self-assembled PHPMA–chol-containing NPs (represented here as NP1 : 5) is dominated by the coil nature of the chains at the surface which is ideally dictated by the Debye function and therefore by a nearly q^{-2} dependence. This is indeed a strong hint on the presence of PHPMA–chol chains at the surface of the NPs. On the other hand, the SAXS profile of NP0 could be fitted by using the form factor of homogeneous spheres where the high-q range follows Porod's law ($I(q) \sim q^{-4}$),[25] meaning a well-defined NP-environment interface.

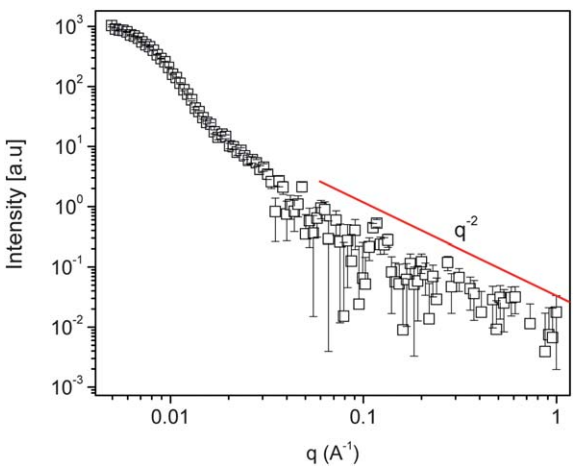

Fig. 6 SAXS data for NP1 : 5 in water at 25 °C.

The thickness of the adsorbed polymer layer was determined through ζ-potential measurements as a function of the electrolyte concentration (Fig. 7 and Table 1).

The increase in the ionic strength of the media leads to a reduction in the ζ-potential of the NPs. This is related to the outward shift of the slip plane as a result of the presence of the adsorbed PHPMA layer. It is worth mentioning that the thickness of the layer is almost constant (~2 nm) for all NPs evaluated. Indeed, as the PHPMA–chol is a multivalent copolymer[22] the formation of a thin layer at the particle surface is expected. Therefore, the PHPMA–chol is presumably bent, forming loops and tails onto the surface of the NPs[42,43] to allow the accommodation of the hydrophobic cholesterol anchor. The increase in the PHPMA–chol concentration results in the formation of a less dense and highly hydrated layer (Fig. 5) which is consistent with classical theories of polymer adsorption predicting the increase in the number of loops and tails with the increase of coverage.[44] In accordance with previous reports, such ζ potential variation *vs.* salinity of the medium is attributed to a rather smooth surface particle structure.[42,45]

The morphology of three NP samples was further evaluated by cryo-TEM. Typical images of NP0, NP1 : 20 and NP1 : 6.7 are shown in Fig. 8a–c, respectively, as well as the corresponding size distribution histograms determined by measuring the NP diameter from the images. For the three samples, distributions of individual and dense NPs were observed.

The corresponding number- and weight-average mean diameters $\overline{D_N}$ and $\overline{D_W}$ as well as polydispersity index P_{TEM} are summarized in Table 2. The diameters determined from cryo-TEM images are significantly lower than the values obtained by DLS. Comparing $\overline{D_N}$ with D_{DLS}, both techniques agree on the fact that the particles NP0 are the largest and the NP1 : 6.7 are the smallest. However, the order changes if we consider $\overline{D_W}$, most likely because NP1 : 20 size distribution appears to be Gaussian while NP0 and NP1 : 6.7 fit better with a log normal function. As DLS evaluates an intensity-average size whereas TEM allows us to measure number-average diameters, DLS sizes are usually larger than the TEM diameters. The effect gets more significant with asymmetrical distributions and increasing

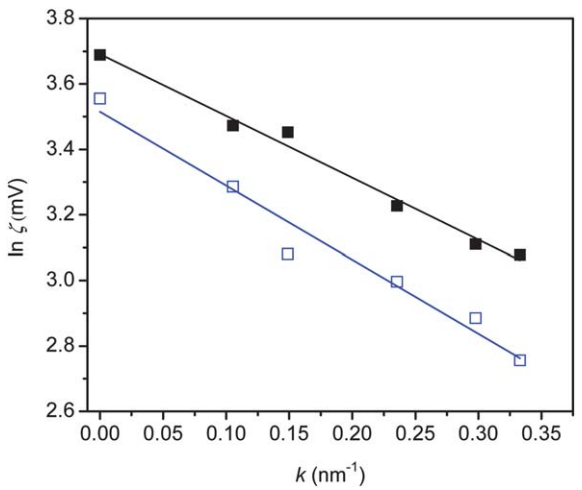

Fig. 7 ln ζ-potential as a function of the Debye-Huckel parameter (k) for NP1 : 20 (■) and NP1 : 5 (□).

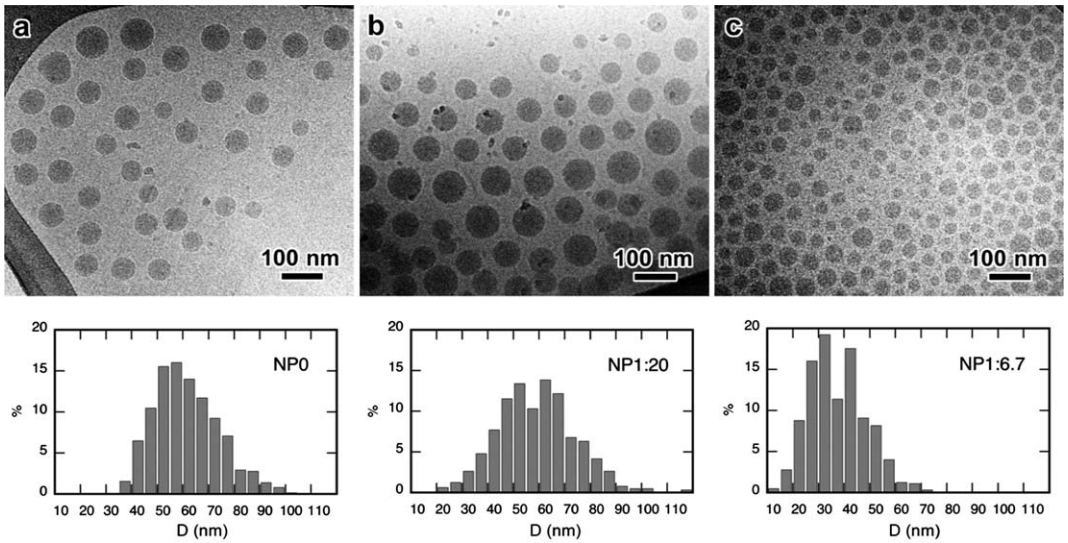

Fig. 8 Cryo-TEM images and corresponding size distribution histograms of the quench-frozen nanoparticles: (a) NP0, (b) NP1 : 20 and (c) NP1 : 6.7. The smaller dark particles are contamination ice crystals.

polydispersity. For this reason, the comparison of the *Z*-average mean diameter $\overline{D_Z}$ calculated from the TEM data with the DLS diameter seems to be more relevant.

High-resolution details on the structure of the NPs could not be detected in the cryo-TEM images possibly due to the poor contrast which is supposed to be linked to the water-swollen characteristic of the assemblies. Indeed, as mentioned above, the naked NP0 nanoparticles are characterized by a water-swollen inner structure and the addition of PHPMA–chol leads to the formation of more collapsed nanoparticles however possessing a highly hydrated and smooth PHPMA stabilizing shell. This explains the slight reduction in R_H and the pronounced reduction in R_G as the concentration of PHPMA–chol increases. Simultaneously, a significant decrease in the apparent diameter $\overline{D_N}$ was observed when comparing the NPs produced by using a low (NP1 : 20) and a high (NP1 : 6.7) amount of PHPMA–chol.

Taking into account the consideration above, it is presumed that the NPs are constituted of an electron-dense compact core revealed in the cryo-TEM images with a hydrophilic PHPMA shell which is too diffuse to be properly detected in our imaging conditions. The NP1 : 6.7 possesses structures with a smaller (denser) core but a thicker surface than NP1 : 20.

Although there are significant differences in the apparent diameter from cryo-TEM images, the overall particle sizes determined by DLS are more similar. In order to visualize the diffuse PHPMA–chol surface, the contrast in cryo-TEM images would probably be improved using a microscope equipped with a field emission gun and an energy filter.[46]

Stability of the nanoparticles

Efficient tumour tissue accumulation requires long circulating NPs to enable time-dependent extravasation of the vessels through the leaky tumour microvasculature.[1,4,7] Therefore, the serum stability is a pre-requisite for the use of polymer nanoparticles as drug carriers *in vivo*. The NPs were incubated in 10% (v/v) human plasma diluted in PBS. The serum stability of the NPs was probed by monitoring their hydrodynamic radius over time. The profiles in Fig. 9a strongly suggest that NP1 : 10 and NP1 : 5 are stable in diluted plasma in which their size remained constant at $R_H = 46$ nm and $R_H = 42$ nm, respectively.

The slight increase in hydrodynamic radius is supposed to be related to the adsorption of a protein monolayer since the average size of single proteins is ~8 nm.[47] On the other hand, a significant increase in the size of NP0 and NP1 : 20 was observed after 15 min of incubation, possibly suggesting particle aggregation and therefore confirming the absence of the protein repelling characteristics. The stability of the nanoparticles was also verified in concentrated saline solutions (Fig. 9b). NP1 : 6.7 and NP1 : 5 are remarkably stable up to 48 h in different ionic strength environments (0.15 M to 1.5 M NaCl) whereas a pronounced increase in the hydrodynamic dimension of NP1 : 20 and NP1 : 10 has been monitored possibly due to the only partial PHPMA coverage.

The convenient presence of a stealth copolymer on the surface of the NPs substantially reduces protein adsorption, thus extending their blood circulation half-life.[8,9] Indeed, anti-biofouling properties of similar hydrophilic polymers have

Table 2 Average diameters of three NP samples determined from the cryo-TEM images and compared to the values measured by DLS

Sample	$\overline{D_N}$ [std] (nm)	$\overline{D_W}$ (nm)	$\overline{D_Z}$ (nm)	$D_{DLS} = 2R_H$ (nm)	$P_{TEM} = \overline{D_W}/\overline{D_N}$
NP0	61.7 [12.4]	69.2	74.1	94.0	1.12
NP1 : 20	59.1 [14.9]	70.0	78.8	80.0	1.18
NP1 : 6.7	37.6 [11.0]	46.8	51.9	74.0	1.24

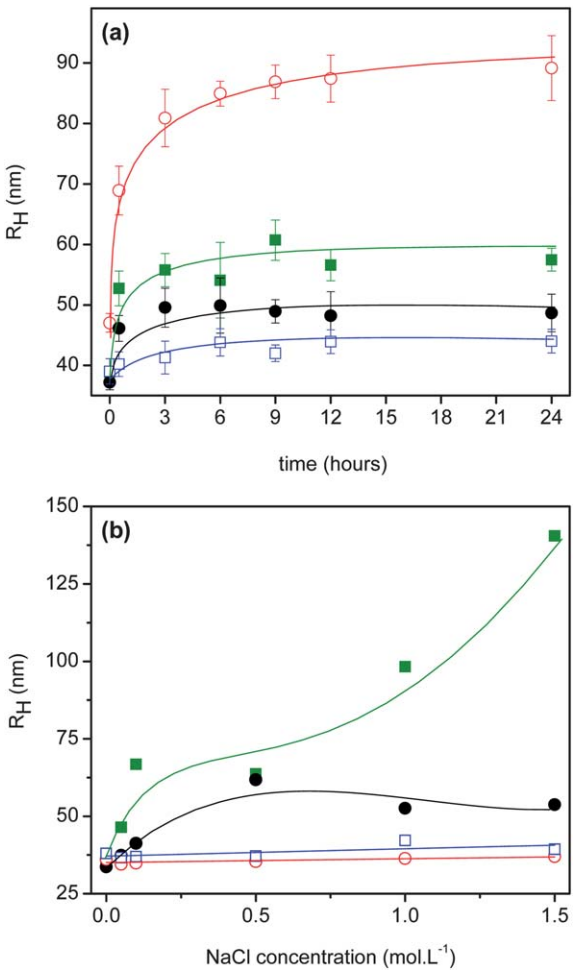

Fig. 9 R_H *vs.* time for NP0 (○), NP1 : 20 (■), NP1 : 10 (●) and NP1 : 5 (□) incubated in 10% v/v human plasma diluted in PBS (pH 7.4 at 37 °C) (a) and (b) R_H *vs.* time for NP1 : 20 (■), NP1 : 10 (●), NP1 : 6.7 (○) and NP1 : 5 (□) as a function of ionic strength after 48 h of incubation.

already been reported with poly(ethylene glycol) (PEG), one of the most effective polymers known to resist protein adsorption and cell adhesion. PEG is a hydrophilic and biocompatible polymer. Since it is highly flexible, it has a relatively large exclusion volume and strongly interacts with water molecules. Its protein resistance is explained on the basis of steric repulsion and hydration forces introducing a high activation energy barrier for proteins to adsorb.[48] Hence, due to the chemical similarities of PEG and the HPMA copolymers (hydrophilicity and absence of charges), the PHPMA surface is also supposed to provide a repulsive effect by the same mechanism, thus making the protein adsorption energetically unfavorable. The long circulation properties of PHPMA-coated adenovirus[23] and liposomes[49] were previously described *in vivo*.

Taking into account that the NP0 (uncoated NPs) are unstable in both saline solutions and in a simulated physiological environment, it is important to note that the aforementioned results suggest that the NPs prepared with 1 : 6.7 and 1 : 5 $w_{HPMA-chol}/w_{PBS/PBDL}$ ratio are optimized regarding their stability in serum and plasma because they are presumably homogeneously covered by PHPMA.

In vitro controlled drug release experiments

Generally, the drug release can be governed by two different mechanisms: (i) a standard diffusion-controlled release or (ii) a triggered pathway initiated by changing the environmental conditions such as pH or temperature.[50] Additionally, considering nanoparticles produced from biodegradable polymers, the drug release can also be controlled by the polymer erosion rate.[51] It is well-known that the drug diffusion-controlled release depends on its effective diffusion coefficient throughout the polymer matrix, which in turn depends on its porosity and tortuosity.[52] At the current investigations, the NPs were loaded with the commonly used anticancer drug DOX. The DOX-loaded NPs (NPDOX) were prepared by having 1 : 6.7 as the $w_{HPMA-chol}/w_{PBS/PBDL}$ ratio. The DOX encapsulation led to a slight increase in the size and dispersity index of the nanocarriers (R_H = 41 nm; 0.12) though a considerable reduction in the ζ-potential was monitored ($\zeta = -12 \pm 3$ mV), which might be ascribed to small amounts of DOX adsorbed onto the outer surface of the nanoparticles, where the amino groups partially neutralize the negative ζ-potential.[53]

The loading content of the NPs was determined by using eqn (7) (~5.0% w/w (50.5 μg DOX per mg NPs) corresponding to a loading efficiency of 50%. This is indeed a relatively low drug loading efficiency. The same nanoparticles provided a paclitaxel (PTX) loading efficiency of ~95%.[25] It highlights that the loading efficiency of the NPs is dictated by the hydrophobic interactions between the anticancer drugs and the core-forming polymer PBS/PBDL. Since the copolyester is particularly hydrophobic and the

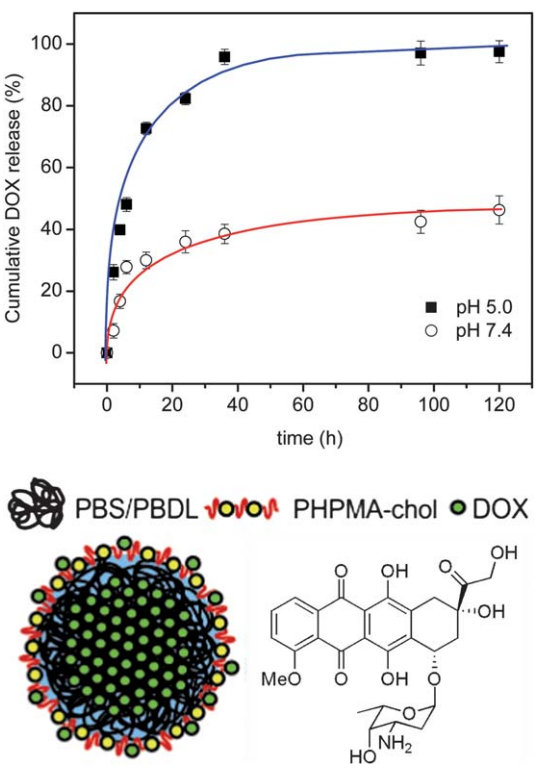

Fig. 10 Doxorubicin release profiles from NPDOX at (■) pH 5.0 and (○) 7.4 (top) and the schematic representation of the DOX-loaded NPs along with the DOX molecular structure (bottom).

DOX is less hydrophobic (water solubility ~ 10 mg mL^{-1}) than PTX (water solubility ~ 0.3 μg mL^{-1}), the hydrophobic interactions are less pronounced in the current system leading to a lower loading efficiency.

The *in vitro* DOX release profiles are shown in Fig. 10 along with the schematic representation of the DOX-loaded NPs. The release experiment was conducted at 37 °C and at pH 7.4 (to simulate conditions during transport in blood and in the healthy tissues) and at pH 5.0 (buffer modeling acidic cytosolic or endosome conditions in tumour cells). The release profile was clearly pH-sensitive. An initial burst effect was observed at pH 7.4 where ~27% of the drug loaded into the NPs was released to the media in the first 6 h. The remaining encapsulated DOX is sustained at the NPs where only ~43% of the DOX is released in 120 h. That means that the drug loss during the systemic circulation of the supramolecular drug carrier (here simulated by the complex body fluid – pH 7.4) can be relatively small. Conversely, the loaded drug was quickly released at pH 5.0 (mimicking the slightly acidic intracellular environment of tumour cells), where ~70% of the loaded DOX was released within the first 12 h and the complete release was achieved in 36 h. Therefore, the NPs exhibit physicochemical properties required for the practical application as nanocarriers in passive tumour-targeting drug delivery *via* pH-triggered release. This is because it suggests that greater bioavailability of DOX can be anticipated after the NPs are internalized in tumour cells *via* endocytosis and entrapped in the acidic endosomal/lysosomal compartments.

It has recently been demonstrated that in PBS/PBDL NPs the PTX drug release is controlled by the bulk erosion rate of the biodegradable copolyester. In the current case, the pH-dependence of DOX release is mainly due to the DOX solubility, which is higher at acidic pH. The initial burst effect noticed at both pH values is due to the faster release of DOX electrostatically adsorbed onto the outer surface of the negatively charged NPs (Fig. 10, bottom), and the release of the remaining DOX physically entrapped into the polymeric hydrophobic core is controlled by a combination of the bulk erosion of the biodegradable NPs and DOX solubility in the incubating media. Indeed, the degradation behavior of the naked PBS/PBDL NPs has been investigated recently[25] and a pronounced reduction in M_w of PBS/PBDL could be observed in ~2 weeks. The particularly fast degradation rate of the PBS/PBDL NPs was attributed to its water-swollen characteristic.

In vitro cell proliferation effect of the NPs

The *in vitro* cell proliferation tested as [^{3}H]-thymidine incorporation into mice C57B/6 and Balb/c unstimulated (spontaneously proliferating) splenocytes incubated with NPs 1 : 6.7 as the $w_{HPMA–chol}/w_{PBS/PBDL}$ ratio was used to evaluate the toxicity of the NPs. The results (Fig. 11) show a significant increase in cell proliferation obtained for NPs incubated with both mice splenocyte cells in all concentrations evaluated.

A similar increase in cell proliferation with increasing concentration of NPs was also observed for the naked NPs[25] and on surfactant-containing systems at low surfactant concentrations.[54] A surfactant concentration higher than 0.1–0.5 mg mL^{-1} disrupts the physiological membranes and becomes highly toxic to cells. In the current case, the enhanced cell proliferation was

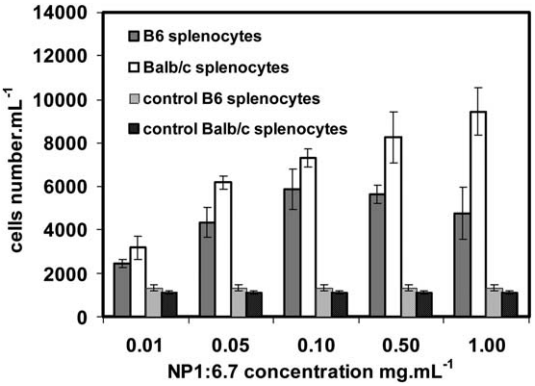

Fig. 11 *In vitro* effect of NPs (NP1 : 6.7) (mg mL^{-1}) on mice Balb/c and B6 splenocytes cell proliferation.

observed also at a higher NP concentration and can be expected once the HPMA copolymers are non-toxic and non-immunogenic and the PBS/PBDL copolyester is biocompatible. This implies that the investigated NPs are supposed to be non-toxic in contact with the living systems fulfilling the basic requirement of good biocompatibility, which is a prerequisite for the biomedical application.

In vitro cytostatic activity

The cytostatic potential of the DOX-loaded NPs and free DOX was also evaluated by [^{3}H]-thymidine incorporation. The inhibition of EL4 tumour cell growth was expressed as IC_{50} which is the concentration of free DOX or DOX equivalent in DOX-loaded NPs which inhibits the cell growth by 50%.[55] All IC_{50} values reported were the average of four independent measurements.

The results shown in Fig. 12 suggest that the unloaded PBS/PBDL (NP0) or NPs (NP1 : 6.7) are non-toxic in all concentrations investigated. Oppositely, the DOX-loaded NPs (NPDOX) are highly cytotoxic (IC_{50} = 0.192 μg mL^{-1}). The cytotoxicity of NPDOX was comparable with the level found in PHPMA–DOX conjugates investigated at the same cancer cell line.[27]

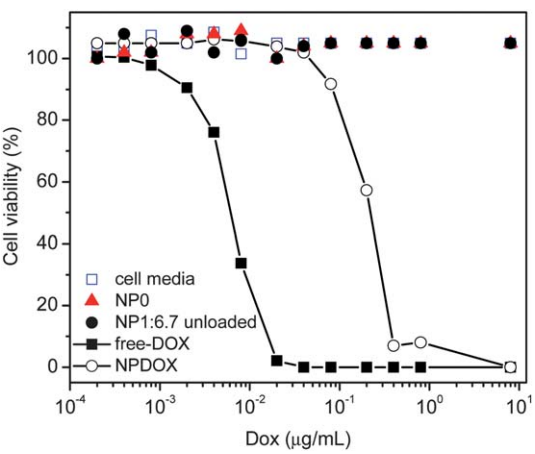

Fig. 12 Cell viability (%) of EL4 lymphoma cells after incubation for 48 h with free DOX (■), NP0 (▲), NP1 : 6.7 unloaded (●), NPDOX (○) and cell media □).

Nevertheless, the reported cytotoxicity of NPDOX was 100 times lower than the cytotoxicity of the free drug (IC_{50} = 0.006 μg mL^{-1}). Since the unloaded NPs are non-toxic, the reduction in the EL4 T cell lymphoma viability is supposed to be related to the presence of the DOX chemotherapeutic; the lower cytotoxicity of the DOX-loaded NPs is the result of a lower rate of cellular uptake of the DOX-containing NPs by endocytosis rather than much faster diffusion of the free drug into the cells and the relatively slow DOX release from NPs after their uptake by the cells.[56] Furthermore, it is worth mentioning that the stealth characteristic and the sub-100 nm size of the NPDOX is supposed to provide them a prolonged blood circulation half-life resulting in potentially enhanced tumour accumulation and improved overall therapeutic efficiency *in vivo* relative to the free DOX.[5]

Conclusions

The preparation, characterization and preliminary evaluation of biological applications of novel polymeric nanoparticles (NPs) comprising a biodegradable poly(butylene succinate-*co*-butylene dilinoleate) – PBS/PBDL – copolyester and a non-immunogenic and non-toxic hydrophilic poly[*N*-(2-hydroxypropyl)methacrylamide] (PHPMA) as a stealth alternative have been reported. The dimension of the NPs was found to be in the range avoiding fast renal clearance (D_H > 10 nm) and are still below the cut-off size of the leaky pathological microvasculature (D_H < 100 nm), thus making the NPs appropriate candidates for targeted drug carrier vehicles exploitable in cancer therapy. The presence of the hydrophilic PHPMA forming the outer surface layer of NPs was evidenced by SAXS, ELS and SLS/DLS measurements, enabling nanoparticles to stealth properties. The stealth property of the biocompatible and biodegradable nanoparticles was achieved by optimizing their surface coating with hydrophilic polymer with a $w_{HPMA–chol}/w_{PBS/PBDL}$ ratio of 1 : 6.7 or 1 : 5. The hydrophilic nanoparticle surface is responsible for the remarkable *in vitro* stability in a simulated physiological environment and ensures particle stability in the presence of salts. Furthermore, a reproducible, efficient and satisfactory physical entrapment of the anticancer drug doxorubicin was achieved (~5.0% w_{drug}/w_{NPs}) and the controlled DOX release is pH-dependent being faster under slightly acidic conditions mimicking an intracellular environment. The cell viability experiments demonstrated that the drug-free NPs are non-toxic whereas the DOX-loaded NPs exert *in vitro* cytostatic efficacy on EL4 T cell lymphoma. Considering the similarities of PHPMA and PEG in terms of low immunogenicity, flexibility, hydrophilicity, and their ability to prolong circulation and reduce toxicity, the PHPMA is reported to be a promising alternative to a PEG-mediated shielding.

Acknowledgements

This research was supported by the Academy of Sciences of the Czech Republic (IAAX00500803 and P208/10/1600). F.C.G. acknowledges financial support from FAPESP (Grant 2010/06348-0).

References

1 L. Y. T. Chou, K. Ming and W. C. W. Chan, *Chem. Soc. Rev.*, 2011, **40**, 233–245.
2 L. Zhang, J. M. Chan, F. X. Gu, J.-W. Rhee, A. Z. Wang, A. F. Radovic-Moreno, F. Alexis, R. Langer and O. C. Farokhzad, *ACS Nano*, 2008, **2**, 1696–1702.
3 A. Bernardi, E. Braganhol, E. Jäger, F. Figueiró, M. I. Edelweiss, A. R. Pohlmann, S. S. Guterres and A. M. O. Battastini, *Cancer Lett.*, 2009, **281**, 53–63.
4 N. Kamaly, Z. Xiao, P. M. Valencia, A. F. Radovi-Moreno and O. C. Farokhzad, *Chem. Soc. Rev.*, 2012, **41**, 2971–3010.
5 J. Fang, H. Nakamura and H. Maeda, *Adv. Drug Delivery Rev.*, 2011, **63**, 136–151.
6 C. H. J. Choi, C. A. Alabi, P. Webster and M. E. Davis, *Proc. Natl. Acad. Sci. U. S. A.*, 2010, **107**, 1235–1240.
7 M. E. Fox, F. C. Szoka and J. M. Fréchet, *Acc. Chem. Res.*, 2009, **42**, 1141–1151.
8 R. Gref, M. T. Minamitake, V. Trubetskoy, V. Torchilin and R. Langer, *Science*, 1994, **263**, 1600–1603.
9 V. P. Torchilin, *Adv. Drug Delivery Rev.*, 2006, **58**, 1532–1555.
10 C. Lemarchand, R. Gref, C. Passirani, E. Garcion, B. Petri, R. Müller, D. Costantini and P. Couvreur, *Biomaterials*, 2006, **27**, 101–118.
11 S. K. Sahho, J. Panyam, S. Prabha and V. Labhasetwar, *J. Controlled Release*, 2002, **82**, 105–114.
12 S. Rudt and R. H. Müller, *J. Controlled Release*, 1993, **25**, 51–59.
13 D. W. Branch, B. C. Wheeler, G. J. Brewer and D. E. Leckband, *Biomaterials*, 2001, **22**, 1035–1047.
14 A. Roosjen, J. de Vries, H. C. van der Mei, W. Norde and H. Busscher, *J. Biomed. Mater. Res., Part B*, 2005, **73B**, 347–354.
15 C. Rodriguez-Emmeneger, A. Jäger, E. Jäger, P. Stepanek, A. Bollogna-Alles, S. S. Guterres, A. R. Pohlmann and E. Brynda, *Colloids Surf., B*, 2011, **83**, 376–381.
16 K. Ulbrich, T. Etrych, P. Chytil, M. Jelínková and B. Říhová, *J. Controlled Release*, 2003, **87**, 33–47.
17 T. Lammers, V. Šubr, P. Peschke, R. Kühnlein, W. E. Hennink, K. Ulbrich, F. Kiessling, M. Heimann, J. Debus, P. E. Huber and G. Storm, *Br. J. Cancer*, 2008, **99**, 900–910.
18 T. Lammers, V. Šubr, K. Ulbrich, V. E. Hennink, G. Storm and F. Kiessling, *Nano Today*, 2010, **5**, 197–212.
19 Ch. M. Ward, M. Pechar, D. Oupický, K. Ulbrich and L. W. Seymour, *J. Gene Med.*, 2002, **4**, 536–547.
20 B. Říhová, *Adv. Drug Delivery Rev.*, 2009, **61**, 1149–1158.
21 C. Koňák, V. Šubr, L. Kostka, P. Štěpánek, K. Ulbrich and H. Schlaad, *Langmuir*, 2008, **24**, 7092–7098.
22 V. Šubr, C. Koňák, R. Laga and K. Ulbrich, *Biomacromolecules*, 2006, **7**, 122–130.
23 N. K. Green, C. W. Herbert, S. J. Hale, A. B. Hale, V. Mautner, R. Harkins, T. Hermiston, K. Ulbrich, K. D. Fisher and L. W. Seymour, *Gene Ther.*, 2004, **11**, 1256–1263.
24 Z. Amoozgar and Y. Yeo, *Wiley Interdiscip. Rev.: Nanomed. Nanobiotechnol.*, 2012, **4**, 219–233.
25 A. Jäger, D. Gromadzki, E. Jäger, F. C. Giacomelli, A. Kozlowska, M. El Fray, L. Kobera, J. Brus, B. Říhová, K. Ulbrich and P. Štěpánek, *Soft Matter*, 2012, **8**, 4343–4354.
26 K. Ulbrich, V. Šubr, J. Strohalm, D. Plocová, M. Jelínková and B. Říhová, *J. Controlled Release*, 2000, **64**, 63–79.
27 P. Chytil, T. Etrych, Č. Koňák, M. Šírová, T. Mrkvan, J. Bouček, B. Říhová and K. Ulbrich, *J. Controlled Release*, 2008, **127**, 121–130.
28 P. Štěpánek, in *Dynamic Light Scattering: The Method and Some Applications*, ed. W. Brown, Oxford Science Publications, Oxford, 1993.
29 H. Dautzenberg, A. Zintchenko, Č. Koňák, T. Reschel, V. Šubr and K. Ulbrich, *Langmuir*, 2001, **17**, 3096–3102.
30 J. N. Israelachivili, in *Inntermolecular and Surface Force*, Academic Press, London, 1985.
31 http://rsbweb.nih.gov/ij/.
32 F. C. Giacomelli, P. Štěpánek, C. Giacomelli, V. Schmidt, E. Jäger, A. Jäger and K. Ulbrich, *Soft Matter*, 2011, **7**, 9316–9325.
33 J. Aubry, F. Ganachaud, J. P. C. Addad and B. Cabane, *Langmuir*, 2009, **25**, 1970–1979.
34 F. Quaglia, L. Ostacolo, G. De Rosa, M. I. La Rotonda, M. Ammendola, G. Nese, G. Maglio, R. Palumbo and C. Vauthier, *Int. J. Pharm.*, 2006, **324**, 56–66.

35 E. Jäger, C. G. Venturini, F. Poletto, L. M. Colome, J. P. U. Pohlmann, A. Bernardi, A. M. O. Battastini, S. S. Guterres and A. R. Pohlmann, *J. Biomed. Nanotechnol.*, 2009, **5**, 130–140.
36 V. C. F. Mosqueira, P. Legrand, H. Pinto-Alphandary, F. Puisieux and G. Barratt, *J. Pharm. Sci.*, 2000, **89**, 614–626.
37 D. T. Birnbaum, J. D. Kosmala and L. Brannon-Peppas, *J. Nanopart. Res.*, 2000, **2**, 173–181.
38 M. Sedlák and Č. Koňák, *Macromolecules*, 2009, **42**, 7430–7438.
39 M. Li, M. Jiang, L. Zhu and C. Wu, *Macromolecules*, 1997, **30**, 2201–2203.
40 F. C. Giacomelli, I. C. Riegel, C. L. Petzhold, N. P. Silveira and P. Stepánek, *Langmuir*, 2009, **25**, 731–738.
41 T. Hu and C. Wu, *Phys. Rev. Lett.*, 1996, **83**, 4105–4107.
42 C. Rouzes, R. Gref, M. Leionard, A. De Sousa Delgado and E. Dellachiere, *J. Biomed. Mater. Res.*, 2000, **50**, 557–565.
43 A. Besheer, J. Vogel, D. Glanz, J. Kressler, T. Groth and K. Mäder, *Mol. Pharmaceutics*, 2009, **6**, 407–415.
44 M. A. Cohen-Stuart, T. Coasgrove and B. Vincent, *Adv. Colloid Interface Sci.*, 1986, **24**, 143–249.
45 D. Duracher, F. Sauzedde, A. Elaissarie, C. Pichot and L. Nabzar, *Colloid Polym. Sci.*, 1998, **276**, 920–928.
46 J. J. Crasous, M. Ballauf, M. Drechsler, J. Schmidt and Y. Talmon, *Langmuir*, 2006, **22**, 2403–2406.
47 F. C. Giacomelli, P. Štěpánek, V. Schmidt, E. Jäger, A. Jäger and C. Giacomelli, *Nanoscale*, 2012, **4**, 4504–4514.
48 H. Otsuka, Y. Nagasaki and K. Kataoka, *Adv. Drug Delivery Rev.*, 2003, **55**, 403–419.
49 K. R. Whiteman, V. Subr, K. Ulbrich and V. P. Torchilin, *J. Liposome Res.*, 2001, **11**, 153–164.
50 F. von Burkersroda, L. Schedl and A. Goopferich, *Biomaterials*, 2002, **23**, 4221–4231.
51 J. M. Chan, L. Zhang, K. P. Yuet, G. Liao, J.-W. Rhee, R. Langer and O. C. Farokhzad, *Biomaterials*, 2009, **30**, 1627–1634.
52 L. A. Fiel, L. M. Rebêlo, T. M. Santiago, M. D. Adorne, S. S. Guterres, J. S. Sousa and A. R. Pohlmann, *Soft Matter*, 2011, **7**, 7240–7247.
53 H. S. Yoo, K. H. Lee, J. E. Oh and T. G. Park, *J. Controlled Release*, 2000, **68**, 419–431.
54 G. Wei, Y. Li, G. Du and J. Chen, *Process Biochem.*, 2003, **38**, 1133–1138.
55 B. Říhová, J. Strohalm, O. Hovorka, V. Šubr, T. Etrych, P. Chytil, R. Pola, D. Plocová, J. Bouček and K. Ulbrich, *J. Controlled Release*, 2008, **127**, 110–120.
56 O. Hovorka, T. Etrych, V. Šubr, J. Strohalm, K. Ulbrich and B. Říhová, *J. Drug Targeting*, 2006, **14**, 391–403.